Technische Universität München
Fakultät für Physik

Spin-wave transport and skyrmion formation in CoFe-based thin film heterostructures

Luis Antonio Flacke

Vollständiger Abdruck der von der Fakultät für Physik der Technischen Universität München zur Erlangung des akademischen Grades eines

Doktors der Naturwissenschaften

genehmigten Dissertation.

Vorsitzender:	Prof. Dr. Frank Pollmann
Prüfer der Dissertation:	1. Prof. Dr. Rudolf Gross
	2. Prof. Dr. Christian Back

Die Dissertation wurde am 14.12.2021 bei der Technischen Universität München eingereicht und durch die promotionsführende Einrichtung am 12.07.2022 angenommen.

Luis Antonio Flacke

Spin-wave transport and skyrmion formation in CoFe-based thin film heterostructures

Dissertation, August 1, 2022
Reviewers: Prof. Dr. Rudolf Gross and Prof. Dr. Christian Back

Technische Universität München

Walther-Meißner-Institut für Tieftemperaturforschung
der Bayerischen Akademie der Wissenschaften
Walther-Meißner-Straße 8
85748 and Garching

Unless the LORD builds the house, They labor in vain who build it;
Unless the LORD guards the city, The watchman stays awake in vain.
— NKJV Psalm 127:1

Abstract

This thesis explores the potential of $Co_{25}Fe_{75}$ alloy-based thin-films and heterostructures for the study of magnetodynamic and magnetostatic phenomena and their applications. We determine different mechanisms contributing to the damping of magnetization spin dynamics in $Co_{25}Fe_{75}$ films via broadband ferromagnetic resonance spectroscopy. Spin-wave excitations and their characteristic propagation lengths in constrained magnonic waveguides are investigated by phase-resolved, micro-focused Brillouin light scattering. In Pt/$Co_{25}Fe_{75}$/Ir-multilayers, we demonstrate magnetic skyrmion formation by magnetic force microscopy and analyze skyrmion stability in external magnetic fields as well as spin dynamics in the skyrmion phase. Our findings show that $Co_{25}Fe_{75}$ films are promising for applications in magnonics and skyrmionics due to their low-magnetic damping and high saturation magnetization.

Kurzfassung

In dieser Dissertation werden magnetische Dünnfilmmultilagen auf der Basis einer $Co_{25}Fe_{75}$ Legierung für die Untersuchung der statischen und dynamischen Eigenschaften der Spinstruktur verwendet. Verschiedene Mechanismen, die zur Dämpfung der Spindynamik beitragen werden mit Hilfe von breitbandiger ferromangetischer Resonanzspektroskopie bestimmt. In strukturierten, magnonischen Wellenleitern werden Spinwellenanregungen und deren charakteristische Ausbreitungsreichweite mit Hilfe von phasenaufgelöster, mikrofokussierter Brillouin Lichtstreuung untersucht. Die Bildung von magnetischen Skyrmionen wird in $Pt/Co_{25}Fe_{75}/Ir$ Multilagen mit Hilfe von Magnetkraftmikroskopie nachgewiesen und es wird deren Stabilität in von außen angelegten magnetischen Feldern untersucht. Es werden desweiteren dynamische Spinanregungen in der Skyrmionenphase beobachtet. Die Ergebnisse zeigen, dass $Co_{25}Fe_{75}$ Filme aufgrund ihrer niedrigen magnetischen Dämpfung und hohen Sättigungsmagnetisierung ein viel versprechendes Anwendungspotential in den Feldern der Magnonik und Skyrmionik besitzen.

Contents

Abstract v

Contents ix

1 Introduction 1

2 Magnetization Dynamics 5
- 2.1 Macrospin Model and Effective Field . . . 5
  - 2.1.1 Effective Field . . . 6
  - 2.1.2 Magnetization in the Effective Field . . . 9
- 2.2 Homogeneous Excitation . . . 11
- 2.3 Broadband Ferromagnetic Resonance Setup . . . 14
- 2.4 Spin Waves . . . 17
- 2.5 Micro-focused Brillouin Light Scattering . . . 20

3 Low Damping CoFe Thin films for Magnetodynamic Applications 25
- 3.1 Reduced Damping by Avoiding Spin Memory Loss . . . 26
- 3.2 Separation of Extrinsic Damping Contributions . . . 28
- 3.3 Spin-Wave Propagation in Low Damping CoFe . . . 33
- 3.4 Magnonic applications based on low-damping CoFe . . . 37
  - 3.4.1 Nonlinear Losses due to Four-Magnon Scattering . . . 38
  - 3.4.2 Spin-Wave Frequency Comb . . . 38
  - 3.4.3 Short Wavelength Spin-Wave Excitation . . . 39

4 Magnetostatics and Domain Formation 41
- 4.1 Domain Formation . . . 41
  - 4.1.1 Uniaxial Anisotropy in Thin Films . . . 42
  - 4.1.2 Dzyaloshinskii-Moriya interaction . . . 43
  - 4.1.3 Spin Spirals and Skyrmions . . . 45
- 4.2 Magnetic Force Microscopy . . . 48
- 4.3 Magnetometry . . . 51

5 Skyrmion Multilayers 53
- 5.1 Fabrication . . . 54
- 5.2 CoFe Thickness Variation . . . 54

5.3 Skyrmion Formation with Easy-Plane Anisotropy 56
5.3.1 Characterization of the sample 57
5.3.2 Micromagnetic Simulation 64
5.3.3 Radius dependence 65
5.4 Interlayer Exchange 70

6 Summary **75**

A Appendix A - Sample Fabrication **77**
A.1 Magnetodynamic Samples 77
A.2 Thickness Variation Samples for Spin Spiral Configuration 82
A.3 Brillouin Light Scattering Samples for DMI Quantification 82
A.4 Samples for Qualitative Interlayer Exchange Investigation 83

B Appendix B - MFM Field Calibration **85**

List of publications **87**

Bibliography **89**

Acknowledgements **113**

1 Introduction

Novel computing paradigms like, e.g., brain-inspired- or neuromorphic computing are more and more sought after in a time that demands not only improved computing performance but also increased energy efficiency. Over the last decades, classical computing built up the technological back bone and exponentially gained relevance in our everyday life. The success of classical semiconductor-based information technology is mainly based on the continuous miniaturization and integration of circuit components following Moore's law since decades [1]. While for the first steps of miniaturization of the integrated circuits (IC) the energy consumption decreased and clock rates increased tremendously, today's microchips are much harder and especially much more expensive to improve [2]. A general IC architecture where the application and thus software adapts to the hardware is expected to be insufficient soon to cope with the exploding amount of data. Alternative computing approaches that allow for parallelization or even resolve the von Neuman bottleneck by allowing in-memory data processing are highly desirable. Thus, for the sake of achieving larger computing and energy efficiencies, hardware needs to be adapted according to the application.

Only recently, vowel recognition based on neuromorphic computing has been shown successfully by using a network of only four synchronized spin torque nano-oscillators (STNOs) [3]. The implementation of the spin degree of freedom for technological applications might not only be useful for read heads of hard disc drives, magnetic random access memory and angle sensors but may as well play an important role for data processing in the future. For neuromorphic computing the separation of memory and processing is overcome by mimicking the brain's neurons and synapses which merge both components. This is realized by so-called memristors (memory + resistor). Their implementation for machine learning tasks already showed improvement by two orders of magnitude in both, energy consumption and acceleration for back propagation algorithms that are necessary for weighting the synaptic links [4]. Inspired by our brain, it is be desirable to achieve as much synapses per neuron as possible to increase the amount of communication paths. However this would result in challenging wiring and 3D stacking architecture of the hardware on the microchip. STNOs could allow for a dense and highly interconnected network due to their ability to radiate microwaves and synchronize with each other without direct wiring [3, 5, 6]. The ability to implement pattern recognition tasks at the hardware level using thin film magnets exemplifies the potential for novel computing paradigms.

Another approach for realizing pattern recognition is based on reservoir computing. Here, an input signal is processed by a reservoir that is previously

trained to map the desired output. The only requirement to the system is that it can store information and has individual non-linear units. Thus, small sized magnetic textures, e.g., skyrmions, provide an encouraging platform for micro-chip reservoir computing hardware as they can reach the low nm-scale. DC and AC currents through a pinned skyrmion bath allow harnessing complex resistance and dynamic magnetization responses [7]. The reservoir itself can thus act as a neuromorphic unit that enables the integration of memory and processing.

Moreover, the employment of spins also endorses benefits in other novel computing approaches. Analog processing can outperform digital devices for specific tasks like, e.g. matrix multiplication. A clear example is the Fourier transform of a wave front passing through a lens. In a recent study, it has been shown that wi-fi signals can be exploited as a medium for calculations [8]. This wave-based (= exploiting wave-like properties) analog computing benefits from parallelization and the possibility of vector calculations rather that binary processing. However, wavelengths of the electromagnetic field at current operation frequencies of a few GHz are rather large. Spin waves in ferromagnetic thin films on the other side provide GHz frequencies together with wavelengths in the micrometer and even in the nanometer range. Hence, miniaturized wave-based computing could be implemented on microchips [9, 10]. However, in contrast to electromagnetic waves, spin waves experience a much stronger dampening which imposes a restriction of their application to their propagation length scale. In order to provide sufficient propagation lengths, low damping properties and high propagation velocities are required.

Apart from computational purposes, thin films involving ferromagnet/heavy metal interfaces were shown to outperform current commercial THz emitters with help of the spin degree of freedom [11]. Here, the nano-patterned magnets show technological relevance for non-invasive material studies by non-ionizing radiation rather than computing applications.

The above-mentioned possibilities of making use of the spin degree of freedom exemplify their high potential for technological devices. Nonetheless, many challenges and limitations are still to be overcome. The most fundamental difference to electronics is the non-conserved quasi-particle number. I.e., the number of electrons is conserved whereas magnons as the quantized excitation of the spin system dissipate. The underlying mechanisms that result in a relaxation strongly define the (energy) efficiency and signal amplitude for many proposed applications [9, 10, 12, 13]. Accordingly, all the above mentioned scenarios benefit from low magnetic damping, such that materials with low loss rates for the magnetic excitations are sought after. Yttrium Iron Garnet (YIG) is the most prominent low damping ferrimagnet and is most specifically used in the field of magnonics [9, 14]. Unfortunately, this material is rather challenging to structure and hardly compatible with current complementary metal-oxide semiconductor (CMOS) technology due to its isolating property. Furthermore, the requirement for

single-crystal Gadolinium Gallium Garnet substrates to achieve its low-damping properties additionally hinders its potential. For technological applications various limitations like costs, easy fabrication, compatibility and flexibility for substrates (deposition possible on Si) have to be considered.

In a recent study the metallic, ferromagnetic Co_xFe_{1-x} alloys were investigated and astonishingly low damping parameters of the $Co_{25}Fe_{75}$ composition were reported [15]. Thus, this work focuses on the implementation of $Co_{25}Fe_{75}$ (CoFe) in thin film multilayers and shows its broad applicability for dynamic and static magnetic phenomena, namely, spin-wave transport and skyrmion creation. The easy fabrication by sputter deposition, simple patterning of nanometer-sized structures, low magnetic damping properties and high saturation magnetization make CoFe a promising platform for further investigation and development of functional multilayers.

In chapter 2, we lay the theoretical basis for describing the dynamics of spin systems within the macrospin model. This approach will be used to describe the microwave response of the thin film ferromagnets. Additionally, we explain how the dynamic measurement techniques, namely, broadband ferromagnetic resonance (BBFMR) and Brillouin light scattering (BLS) can be employed to obtain insight into the magnetic properties of the samples.

Chapter 3 focuses on the magnetodynamic response of CoFe thin-film multilayers. We use BBFMR and thereby separate various contributions to the magnetic damping in CoFe thin films. We take advantage of the low damping achieved in the samples for spin-wave excitation in a structured CoFe magnonic waveguide. Here, spin waves are analyzed by BLS where large spin-wave propagation lengths and group velocities are achieved.

Chapter 4 provides the underlying physical framework required to describe the magnetostatic response in magnetic thin films below saturation. Domain formation is discussed and we give a short overview of magnetic skyrmions and their creation in magnetic thin films.

In chapter 5, we focus on thin-film multilayers that exhibit skyrmion formation. The magnetic properties in the multilayer system are extensively characterized by BBFMR, superconducting quantum interference device (SQUID) magnetometry, BLS, micromagnetic simulations using mumax3 [16], anomalous Hall-effect measurements and most importantly by magnetic force microscopy (MFM). The latter technique allows for direct visualization of the magnetic solitons. Their magnetic field dependent evolution is analyzed and we demonstrate robust skyrmion size for a broad range of external magnetic fields.

Magnetization Dynamics

2

The implementation of magnetism in computational technologies requires a precise control of material parameters and magnetic properties. The determination of the magnetodynamic susceptibility as the linear response of a magnetic material to a time-dependent perturbation allows to obtain insight into material parameters like the effective magnetizations, magnetic anisotropies, the gyromagnetic ratio, energy dissipation and many more. The microwave response of magnetic thin films plays a major role for the experimental work in this thesis such that a basic understanding of the magnetic behavior in presence of external perturbation shall be introduced within the following sections. The fundamental concepts necessary to analyze and interpret the obtained results are well established in literature [17–23] and textbooks [19, 24–27] such that this theory chapter follows the argumentations and derivations of the available references and additional previous works realized at the Walther-Meißner-Institut [28–33].

2.1 Macrospin Model and Effective Field

Magnetic moments within a ferromagnet in general are aligned parallel to each other by the quantum-mechanical exchange or Heisenberg interaction [34]. They can be collectively described within a homogeneously (i.e. uniformly) magnetized system with volume V by the macroscopic magnetization $\mathbf{M}$ as a magnetic moment density

$$\boldsymbol{M} = \frac{1}{V}\sum_i \boldsymbol{\mu}_i = \boldsymbol{m}\, M_\mathrm{S}, \tag{2.1}$$

where $\boldsymbol{\mu}_i$ represent the effective magnetic moments of respective atoms (or the corresponding collective itinerant electrons attributed to each atom). The magnetization vector is split into its magnitude M_S as the saturation magnetization and its direction given by the unit vector $\boldsymbol{m}$. In isolating materials, the Heisenberg model allows to quantify the resulting moments by the overlap of electron orbitals from adjacent atoms. The Heisenberg interaction is a direct exchange that stems from overlapping electron wave functions. The coulomb repulsion together with Heisenberg's uncertainty principle and the Pauli principle lead to an energy contribution that can be described as [24]

$$F_\mathrm{ex} = -\frac{1}{V}\sum_{j\neq i, i>j} J_A^{ij}\frac{1}{\hbar^2}\boldsymbol{S}_i \cdot \boldsymbol{S}_j. \tag{2.2}$$

Here, J_A^{ij} is the exchange constant [24], $\hbar$ is the reduced Planck constant and $\boldsymbol{S}_{i,j}$ being the spin operators. However, in itinerant ferromagnets the collective behavior of conducting electrons has to be considered instead of localized electrons of neighboring atoms. But with help of the mean-field-theory that describes a fictitious mean-field or exchange field the concept of the exchange constant J_A as in Eq. 2.2 can still be employed for band ferromagnets [24]. It plays a crucial part for the magnetic free energy density but for the following discussions focusing on a saturated (uniform) magnetic state its influence vanishes and can thus be neglected. It becomes clear, that while this contribution is responsible for the collective behavior of magnetic moments it does not contribute to a favored direction of the macroscopic magnetization.

2.1.1 Effective Field

In thermal equilibrium, the magnetization vector aligns with the direction where the effective magnetic field

$$\mu_0 \boldsymbol{H}_\mathrm{eff} = -\boldsymbol{\nabla}_M F_\mathrm{m}\big|_{\boldsymbol{M}=\boldsymbol{M}_0} = -\left(\frac{\partial}{\partial M_\mathrm{x}}, \frac{\partial}{\partial M\mathrm{y}}, \frac{\partial}{\partial M_\mathrm{z}}\right) F_\mathrm{m}\big|_{\boldsymbol{M}=\boldsymbol{M}_0} \tag{2.3}$$

exhibits its minimum magnitude. As can be seen from the equation, $\mu_0 \boldsymbol{H}_\mathrm{eff}$ depends on the magnetization direction as well. In absence of external magnetic fields it can be stated, alternatively, that the thermal equilibrium is achieved when the alignment of the magnetization $\boldsymbol{M}_0$ returns a minimum of the magnetic free energy density (F_m)[1]. F_m is composed of various contributions that in sum define the energy landscape and thus the favored direction of $\boldsymbol{m}$. A short overview of relevant contributions is given in the following.

2.1.1.1 Magnetocrystalline Anisotropy

The non-spherical $3d$- or $4f$-electron orbitals are responsible for the magnetocrystalline anisotropy. Because of the more complex shape of the orbitals a change of direction of the orbital moments alters the overlap of the wavefunction between two atoms [2]. Together with the overlap, the electrostatic exchange energy is varied which consequently induces a direction dependence, i.e. an anisotropy, of the orbital moments. Even though the ferromagnetism of the metals used in this thesis (Co and Fe) stems mostly from the electron spin, the spin-orbit coupling connects the orbital- with the spin-moment and subsequently provokes the magnetocrystalline anisotropy [24, 35–38].

In crystalline magnetic systems this contribution is one of the most relevant, however, this work focuses on polycrystalline samples only. By the arrangement

[1] In a more general sense, including external magnetic fields a minimum of the free enthalpy density $G = F_\mathrm{m} - \boldsymbol{M} \cdot \boldsymbol{B}_\mathrm{ext}$, with external magnetic field $\boldsymbol{B}_\mathrm{ext}$ is required [24].

[2] More generally, Coulomb repulsion is altered by changing mean distances of electrons due to the shape and alignment of orbitals. A direct overlap is not strictly required.

of all possible crystallographic orientations a directional dependence induced by the lattice symmetry is averaged out. We will thus proceed with our discussion shedding light on a strong determinant of the magnetization direction in the investigated samples.

2.1.1.2 Shape Anisotropy

The finite size of a magnetized sample results in magnetic surface charges, which generate a magnetic field inside the sample pointing in opposite direction to the externally applied magnetic field. It is therefore called demagnetization field. Depending on the shape of the sample and direction of external fields these internal fields can vary strongly in magnitude. The resulting contribution is thus often referred to as shape anisotropy and is non-homogeneous for arbitrary shapes. For reasons of simplicity the discussion can be reduced to ellipsoidal shapes, where the demagnetizing fields are homogeneous and can be written as [27]

$$\boldsymbol{H}_{\text{dem}} = -\overleftrightarrow{\boldsymbol{N}}\boldsymbol{M} = -\begin{pmatrix} N_{xx} & N_{xy} & N_{xz} \\ N_{yx} & N_{yy} & N_{yz} \\ N_{zx} & N_{zy} & N_{zz} \end{pmatrix} \begin{pmatrix} M_x \\ M_y \\ M_z \end{pmatrix}. \tag{2.4}$$

In a coordinate system with axes along the main axes of the ellipsoid the demagnetization tensor $\overleftrightarrow{\boldsymbol{N}}$ can be reduced to its diagonal components N_{xx}, N_{yy}, and N_{zz}. The free energy density contribution of the demagnetizing field thus can be expressed as [24]

$$F_{\text{dem}} = -\frac{1}{2}\mu_0 \boldsymbol{M} \cdot \boldsymbol{H}_{\text{dem}} = \frac{1}{2}\mu_0 \boldsymbol{M} \overleftrightarrow{\boldsymbol{N}} \boldsymbol{M}. \tag{2.5}$$

As the samples discussed in Chap. 3 and Chap. 5 can be described as magnetic thin films we employ a further simplification. The demagnetization factor for a magnetization pointing perpendicular to the surface of a thin film is $N \approx 1$, whereas for magnetizations lying in the plane results in $N \approx 0$. The shape anisotropy contribution to the free energy density for thin films can thus be written as

$$F_{\text{dem}} = \frac{1}{2}\mu_0 \boldsymbol{M}_{\text{S}}^2. \tag{2.6}$$

In order to minimize the resulting energy density the magnetic moments will try to reduce stray fields. In the case of a magnetic thin film this is achieved by a rotation of the magnetization towards the plane. As a consequence, at minimum, a magnetic field of $\mu_0 H = \mu_0 M_{\text{S}}$ is required in order to drag the magnetic moments perpendicular to the surface. In real samples and in absence of any contribution that imposes a favored direction the demagnetization leads to the formation of magnetic domains (see Chapter 4) in order to further reduce magnetic

stray fields [24]. However, within the macrospin model only the homogeneously aligned magnetization is considered. The simplification is justified whenever other contributions like strong anisotropies or external magnetic fields provoke a fully saturated magnetization.

2.1.1.3 Interface-induced Anisotropy

By its nature, thin films exhibit interfaces that intrinsically induce a symmetry breaking. While the film plane in our case can be assumed to be isotropic the axis parallel to the surface normal is distinct which introduces uniaxial anisotropies. A perfect example of an anisotropy contribution with uniaxial character is the previously discussed shape anisotropy. Nonetheless, the interface between a ferromagnet and the adjacent material can result in further anisotropy terms with the same symmetry. A common effect stems from the mismatch of the lattice constants of different materials where elastic strain can impose additional anisotropy contributions at the interface [39–41]. Also, an altered density of states at the Fermi surface and the influence of spin-orbit coupling by heavy metals were shown to be responsible for uniaxial anisotropies [42,43]. Exemplary and common thin film bilayer compositions where an interface induced perpendicular magnetic anisotropy (PMA) is observed are Co/Pt [40], Co/Au [41] and Co/Ni [42]. While in general the axis out of the thin film plane can be both, easy or hard axis depending on the details of the interfaces we will focus on systems where their interface contributions constitute an easy axis along the surface normal.

For the uniaxial anisotropy a phenomenological description with directional cosines can be employed. Without loss of generality we can assume the easy axis direction to align with the z-axis such that the energy contribution can be written dependent on $m_z^2 = \cos^2\theta$, where θ describes the angle between $\boldsymbol{m}$ and $\boldsymbol{z}$. By using the relation $m_x^2 + m_y^2 = 1 - m_z^2 = \sin^2\theta$ the free energy density contribution can be formulated in first order as [24,44]

$$F_u = K_u(\boldsymbol{z}\cdot\boldsymbol{m})^2 = K_u \sin^2\theta. \tag{2.7}$$

The case $K_u > 0$ describes a system with an easy axis along the z direction, whereas $K_u < 0$ defines a hard axis behavior, or easy plane system with no preferred axis in the plane. The resulting effective field in z-direction can be calculated by [19]

$$\mu_0 H_k = \frac{2K_u}{M_S}. \tag{2.8}$$

As we restrict our attention to multilayers with interface effects favoring a magnetization alignment out of the plane, its contributions compete with the above

described shape anisotropy. Both anisotropies share the uniaxial symmetry which allows to summarize their opposing behavior by the effective energy density

$$K_{\text{eff}} = K_{\text{u}} - \frac{\mu_0 M_{\text{S}}^2}{2}. \tag{2.9}$$

Here, the second term represents the demagnetization as formulated in Eq. 2.6. However, other than the above mentioned bilayer systems where PMA (i.e. $K_{\text{eff}} > 0$) was observed, the studies in this thesis focus on easy-plane multilayers with $K_{\text{eff}} < 0$. Nonetheless, the interfacial anisotropy, here described by K_{u}, is crucial for understanding the presented results in Chapter 3 and 5. Its role outside of the macrospin model will further be discussed in Chapter 4 and 5.

2.1.1.4 Zeeman Energy

The magnetization direction can additionally be controlled externally by applying a magnetic field H_0 induced by, e.g., an electromagnet. The corresponding energy density of a magnetic moment in a magnetic field [24]

$$F_{\text{zee}} = -\mu_0 \boldsymbol{M} \cdot H_0 \tag{2.10}$$

and Eq. (2.3) inherently define $H_{\text{eff}}^{zee} = H_0$. Thus, for the Zeeman energy contribution only the real magnetic field is relevant and virtual fields by molecular- or exchange field play no role [24].

2.1.2 Magnetization in the Effective Field

All these contributions mentioned above sum up to the total free energy density F and thus define the effective magnetic field which we can express as

$$\boldsymbol{H}_{\text{eff}} = \boldsymbol{H}_0 + \boldsymbol{H}_{\text{dem}} + \boldsymbol{H}_{\text{k}}. \tag{2.11}$$

The magnetization will align parallel to the effective field in a thermodynamic equilibrium. Within the macrospin model describing the saturated magnetization the exchange energy contribution is zero and is thus not included [45]. If the magnetization is deflected from its equilibrium direction, the effective field exerts a torque $\boldsymbol{T}$ given by [24].

$$\boldsymbol{T} = \frac{d\boldsymbol{J}}{dt} = V\mu_0 \boldsymbol{M} \times \boldsymbol{H}_{\text{eff}}. \tag{2.12}$$

Evidently, $\boldsymbol{M}$ is equivalent to an angular momentum $\boldsymbol{J}$

$$\boldsymbol{M} = -\gamma \frac{\boldsymbol{J}}{V} \tag{2.13}$$

with γ being the gyromagnetic ratio $g\mu_B/\hbar$, with Landé-factor g and the Bohr magneton μ_B. The above stated Eq. (2.12) and (2.13) merge to the Landau-Lifshitz equation [20]

$$\frac{d\boldsymbol{M}}{dt} = -\gamma\mu_0 \boldsymbol{M} \times \boldsymbol{H}_{\text{eff}}. \tag{2.14}$$

This formulation describes a constant precession of $\boldsymbol{M}$ around $\boldsymbol{H}_{\text{eff}}$, such that the magnetization would never reach thermodynamic equilibrium again after deflecting it from the equilibrium direction. In reality, many different dissipation mechanism lead to a relaxation of the precession which can be described as a magnetic damping. Lenz' rule is one of the most known reasons for magnetic damping via the induction of eddy currents [46, 47] as it finds application in slowing down trains. However, many further loss channels, e.g. due to the interaction with quasi-particles, exist. Below, some are discussed in Chapter 3.2. A large variety of such loss channels can be summarily treated phenomenologically by a dimensionless damping constant α which was introduced by T. Gilbert [21]. It is often referred to as Gilbert damping parameter. By including a viscous damping term $\propto \alpha\dot{M}$ to Eq. (2.14) the famous Landau-Lifshitz-Gilbert (LLG) equation is obtained

$$\frac{d\boldsymbol{M}}{dt} = -\gamma\mu_0 \boldsymbol{M} \times \boldsymbol{H}_{\text{eff}} + \frac{\alpha}{M_S}\boldsymbol{M} \times \frac{d\boldsymbol{M}}{dt}. \tag{2.15}$$

The resulting motion is depicted in Fig. 2.1, where the magnetization relaxes towards its equilibrium position in a precessional manner. It becomes evident, that a large value for α results in a fast relaxation of the magnetization towards its equilibrium direction.

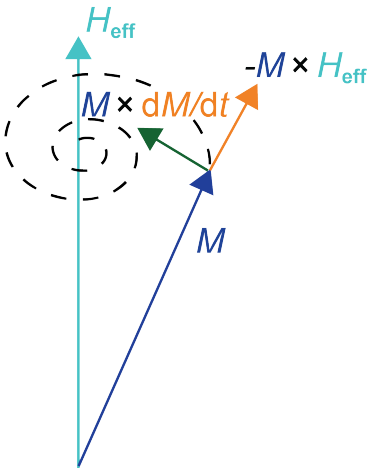

Fig. 2.1. – Sketch of the damped magnetization precession around the effective field defining the equilibrium direction to the magnetization

2.2 Homogeneous Excitation

In the previous section, we discussed the response of the magnetization to a static effective field after deflection from its equilibrium direction. Now, we turn the attention towards the case of an additional time periodic perturbation, where the oscillating magnetic field is applied in such a way that its corresponding torque counteracts the inherent relaxation. The damped motion in Fig. 2.1 can be compensated by a perturbative radiofrequency field $\boldsymbol{h}_{\mathrm{rf}}$ applied perpendicular to $\boldsymbol{H}_{\mathrm{eff}}$. By use of a homogeneous driving field with a frequency that matches the precession frequency of $\boldsymbol{M}$ its motion can be sustained. Such a scenario, the magnetization in an effective field with a perpendicular driving field, is analogous to a driven harmonic oscillator with damping. The derivation of the resonance condition will be sketched in the following as its detailed calculation can be found in many previous works [19, 25, 29–31].

Without loss of generality, we let the effective field without perturbing driving field point in the z-direction such that $\boldsymbol{H}_{\mathrm{eff}} = H_{\mathrm{eff}}\boldsymbol{z}$, with unit vector $\boldsymbol{z}$. The sample is assumed to have an ellipsoidal shape with its symmetry axes pointing along the coordinate axes x, y, and z such that the demagnetization tensor $\overleftrightarrow{\boldsymbol{N}}$ reduces to its diagonal components N_{xx}, N_{yy}, N_{zz}. By adding an oscillating, perpendicular driving field $\boldsymbol{h}_{\mathrm{rf}}(t) = \boldsymbol{h}_{\mathrm{rf}} \cdot \exp(-i\omega t)$ we can write:

$$\boldsymbol{H}_{\mathrm{eff}} = \boldsymbol{H}_0 + \boldsymbol{H}_{\mathrm{dem}} + \boldsymbol{H}_{\mathrm{k}} + \boldsymbol{h}_{\mathrm{rf}}(t) = \begin{bmatrix} -N_{xx}M_x(t) + U_{xx}H_{\mathrm{k}} \\ -N_{yy}M_y(t) + U_{yy}H_{\mathrm{k}} \\ H_0 - N_{zz}M_{\mathrm{S}} + U_{xx}H_{\mathrm{k}} \end{bmatrix} + \begin{bmatrix} h_{\mathrm{rf},x}(t) \\ h_{\mathrm{rf},y}(t) \\ 0 \end{bmatrix}. \tag{2.16}$$

Here, U_{ii} with $i = x, y, z$ represents the diagonal entries of the uniaxial anisotropy tensor analogous to the demagnetization tensor. We consider a static external magnetic field $\boldsymbol{H}_0 = H_0\boldsymbol{z}$, static demagnetization $-N_{zz}M_{\mathrm{S}}$ and uniaxial anisotropy H_{k}, together with the time dependent radiofrequency excitation and its induced dynamic demagnetization $-N_{ii}M_i(t)$, with $i = x, y$. The following derivation restricts to linear response, which holds true for excitation fields $|\boldsymbol{h}_{\mathrm{rf}}| \ll |\boldsymbol{H}_0|$. In this case, the magnetization with $M_{x,y} \ll M_z$ points mainly along $\boldsymbol{z}$-direction with the approximation $M_z = M_{\mathrm{S}}$. A harmonic ansatz for $M_{x,y}(t) = M_{x,y} \cdot \exp(-i\omega t)$ plugged into the LLG equation (Eq. (2.15)) returns a differential equation that describes the linear response relation between perturbative field and magnetization by

$$\begin{bmatrix} h_{\mathrm{rf},x} \\ h_{\mathrm{rf},y} \end{bmatrix} = \overleftrightarrow{\chi}^{-1} \begin{bmatrix} M_x \\ M_y \end{bmatrix}. \tag{2.17}$$

The inversion of $\overleftrightarrow{\chi}^{-1}$ and multiplying M_S^2 to obtain a dimensionless quantity then returns the Polder susceptibility [48]

$$\begin{aligned}\overleftrightarrow{\chi} &= \begin{bmatrix} \chi_{xx} & \chi_{xy} \\ \chi_{yx} & \chi_{yy} \end{bmatrix} \\ &= \frac{M_S}{\det\left(\overleftrightarrow{\chi}^{-1}\right)} \cdot \begin{bmatrix} A_{11} + \frac{i\omega\alpha}{\gamma\mu_0} & \frac{i\omega}{\gamma\mu_0} \\ -\frac{i\omega}{\gamma\mu_0} & A_{22} + \frac{i\omega\alpha}{\gamma\mu_0} \end{bmatrix}\end{aligned} \tag{2.18}$$

with

$$\begin{aligned} A_{11} &= H_0 + (N_{yy} - N_{zz})M_S - (U_{yy} - U_{zz})H_k \\ A_{22} &= H_0 + (N_{xx} - N_{zz})M_S - (U_{xx} - U_{zz})H_k. \end{aligned} \tag{2.19}$$

The Polder susceptibility represents the complex response function of the magnetization regarding a small harmonic perturbation of the effective magnetic field. A schematic depiction of the real χ' and imaginary χ'' part of the first entry - it corresponds to the response of a damped harmonic oscillator - is shown in Fig. 2.2 a) for a system assuming $N_{xx} = N_{yy} = 0$ and $N_{zz} = 1$ and $H_k = 0$.

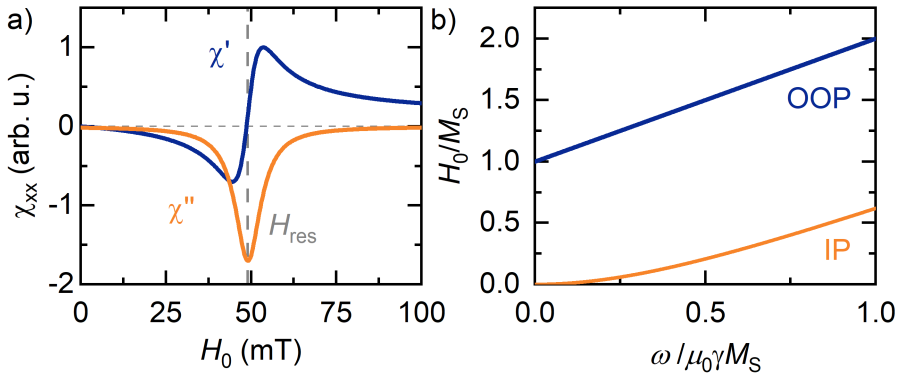

Fig. 2.2. – a) Schematic of the first entry of the Polder susceptibility depending on the external magnetic field strength with the real part χ' and the imaginary part χ'' indicating the absorption. Here, a frequency of 10 GHz, $\mu_0 M_S = 1.5$ T, $\mu_0 H_k = 0$, Landé-factor $g = 2.1$ and $\alpha_G = 0.02$ was used for a thin film with the external magnetic field applied in-plane (IP). b) Schematic of the Kittel equation of the resonance field for the IP (see Eq. (2.21)) and out-of-plane (OOP, see Eq. (2.23)) geometry.

In order to obtain the resonance field H_{res} for a fixed frequency the real part of the resonance condition $\det(\overleftrightarrow{\chi}^{-1}) = 0$ (see Eq. (2.18)) has to be solved. The two simple thin-film cases, i.e. $\boldsymbol{H}_0$ in the thin-film plane (in plane IP) and $\boldsymbol{H}_0$ along

the out of plane (OOP) direction, are depicted in Fig. 2.2 b). In a general form we can derive an expression for the resonance field known as Kittel equation as:

$$H_{\mathrm{res}} = -\frac{1}{2}M_{\mathrm{S}}(N_{xx}+N_{yy}-2N_{zz}) + \frac{1}{2}H_{\mathrm{k}}(U_{xx}+U_{yy}-2U_{zz}) + \sqrt{\left(\frac{2\pi f}{\gamma\mu_0}\right)^2 + \left(\frac{M_{\mathrm{S}}(N_{xx}+N_{yy}) - H_k(U_{xx}+U_{yy})}{2}\right)^2} \tag{2.20}$$

with frequency $f = \omega/2\pi$. As already indicated above, for the thin films two scenarios are separated from each other depending on whether the externally applied field lies within the film plane or points parallel to the surface normal. Assuming an infinitely extended thin film with its plane being defined by the orthogonal unit vectors $\boldsymbol{e}_1$ and $\boldsymbol{e}_2$ and the surface normal pointing along $\boldsymbol{e}_3$ the general form of Eq. (2.20) can be specified for the IP and OOP case. The in-plane case allows two simple coordinate transformation. Without loss of generality we pick $\boldsymbol{e}_1 = \boldsymbol{z}$, $\boldsymbol{e}_2 = \boldsymbol{x}$ and $\boldsymbol{e}_3 = \boldsymbol{y}$ such that $N_{xx} = N_{zz} = U_{xx} = U_{zz} = 0$ and $N_{yy} = U_{yy} = 1$. This allows to formulate the IP-Kittel equation for thin films

$$H_{\mathrm{res}} = \sqrt{\left(\frac{2\pi f}{\gamma\mu_0}\right)^2 + \left(\frac{M_{\mathrm{eff}}}{2}\right)^2} - \frac{M_{\mathrm{eff}}}{2} \tag{2.21}$$

with the effective magnetization

$$M_{\mathrm{eff}} = M_{\mathrm{S}} - H_{\mathrm{k}}. \tag{2.22}$$

On the other hand, when considering the OOP case, the coordinate systems translate with $\boldsymbol{e}_1 = \boldsymbol{x}$, $\boldsymbol{e}_2 = \boldsymbol{y}$ and $\boldsymbol{e}_3 = \boldsymbol{z}$, such that $N_{xx} = N_{yy} = U_{xx} = U_{yy} = 0$ and $N_{zz} = U_{zz} = 1$. This reduces Eq. (2.20) to the OOP-Kittel equation

$$H_{\mathrm{res}} = M_{\mathrm{eff}} + \frac{2\pi}{\gamma\mu_0}f = M_{\mathrm{eff}} + \frac{h}{g\mu_0\mu_{\mathrm{B}}}f. \tag{2.23}$$

The two Kittel equations for IP (Eq. (2.21)) and OOP (Eq. (2.23)) will prove to be a useful tool for the extraction of magnetic material parameters of the investigated thin films. However, apart from the resonance position the resonance linewidth will be of importance as well. While the real part of the resonance condition returns the Kittel equations, the imaginary part gives insight into the linewidth. Solving the mathematical equation the full-width-half-maximum of the resonance can be extracted as

$$\Delta H = 2\frac{\alpha\omega}{\mu_0\gamma}. \tag{2.24}$$

Note that Eq. (2.24) holds for both, IP and OOP configuration. From Eq. (2.24) it becomes apparent that the phenomenological damping parameter α can be obtained by analyzing the linewidth. However, real measurements often exhibit

an additional offset H_{inh} which is referred to as the inhomogeneous linewidth broadening. Exemplary phenomena that can induce such an offset could be inhomogeneities and/or magnon-magnon scattering. As a consequence a broad frequency range has to be investigated to properly extract α from the frequency dependence

$$\mu_0 \Delta H = 2\frac{2\pi f \alpha}{\gamma} + \mu_0 H_{\text{inh}}. \tag{2.25}$$

For an ideal sample, this linear function is usually expected to cross the origin, but as inhomogeneities can induce a constant shift H_{inh} can be taken as a rough indication of the sample's quality and/or roughness.

In chapter 3.2 the analysis of resonance data in OOP case will play a major role such that it will be convenient to only consider the first entry of the Polder susceptibility in the OOP case as

$$\chi(H_0) = \frac{M_S(H_0 - H_{\text{res}} + H_{\text{eff}})}{\left(H_0 - H_{\text{res}} + H_{\text{eff}} + i\frac{\Delta H}{2}\right)^2 - H_{\text{eff}}^2}. \tag{2.26}$$

In this case, the effective field $H_{\text{eff}} = 2\pi f / \mu_0 \gamma$.

2.3 Broadband Ferromagnetic Resonance Setup

In order to quantify the magnetic properties of a thin film its susceptibility is measured by broadband ferromagnetic resonance (BBFMR). A simple setup consisting of a vector network analyzer (VNA), a coplanar waveguide (CPW) and an electromagnet for the creation of a homogeneous external magnetic field is sufficient for this measurement technique. The illustration in Fig. 2.3 shows a sample (with dimensions length l, width b and thickness d_{FM}) placed on top of the center conductor (CC) of the CPW. The conducting line is connected to the two ports of the VNA with which the transmission at various frequencies and external magnetic field magnitudes and directions ($\boldsymbol{H}_0 \parallel \boldsymbol{e}_1$ or $\boldsymbol{H}_0 \parallel \boldsymbol{e}_3$) is recorded. When the external magnetic field matches the resonance condition at the used frequency the sample absorbs power from the electromagnetic field produced by the CC which results in a dip in transmission. This absorption encodes the susceptibility. The underlying theoretical concept will be shortly introduced in the following.

The ac current in the conducting line generates the oscillating driving field h_{rf} with an IP and an OOP component regarding the CPW plane. We define the coordinate system by the vectors $\boldsymbol{e}_1$, $\boldsymbol{e}_2$ and $\boldsymbol{e}_3$ and its components x', y' and z'

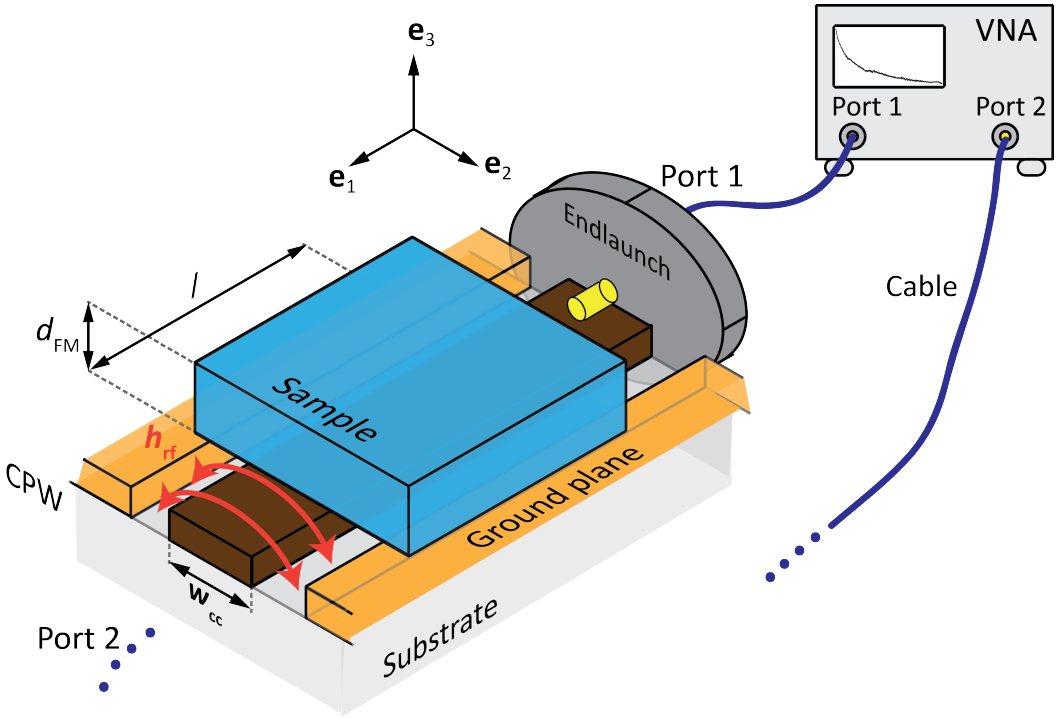

Fig. 2.3. – Sketch of the BBFMR setup used. A thin-film is placed on top of the CC of the CPW. A VNA measures the transmission between the two ports. The microwave current in the CC induces an oscillating magnetic field h_{rf} which serves as driving field to the FMR. At resonance condition the sample absorbs power from the conducting line which influences the recorded transmission. For the measurement the homogeneous external magnetic field is applied either along $\boldsymbol{e}_1$ (IP case) or $\boldsymbol{e}_3$ (OOP case). The measurement is performed for various frequencies and field points to record the field and frequency dependence of the resonance. The illustration is adapted from Ref. [49].

respectively. When the CC is in the shape of a thin strip with uniform current density the driving field is given by the Karlqvist equations [50]:

$$\begin{aligned} h_{y'}(y',z') &= \frac{h_0}{\pi}\left(\arctan\left(\frac{y'+w_{\mathrm{cc}}/2}{z'}\right)-\arctan\left(\frac{y'-w_{\mathrm{cc}}/2}{z'}\right)\right) \\ h_{z'}(y',z') &= \frac{h_0}{2\pi}\ln\left(\frac{(y'+w_{\mathrm{cc}}/2)^2+(z')^2}{(y'-w_{\mathrm{cc}}/2)^2+(z')^2}\right). \end{aligned} \tag{2.27}$$

Here, w_{cc} is the width of the center conductor and the field amplitude $h_0 = J_{\mathrm{CC}}/2 = I/2w_{\mathrm{cc}}$ at $(y',z') = (0,0)$, where I is the current flowing through the strip. The generated field is relevant for the magnetic flux Φ whose change induces the detectable voltage in the CPW by

$$V_{\mathrm{ind}} = -\frac{\partial\Phi}{\partial t}. \tag{2.28}$$

This allows to restrict the discussion to the dynamic part of the flux which can be written as

$$\begin{aligned}\Phi_{\mathrm{dyn}} &= \frac{\mu_0}{I}\iiint_{\mathrm{V}} \boldsymbol{h}(y',z')\cdot\overleftrightarrow{\chi}\cdot\boldsymbol{h}(y',z')\,dx'dy'dz' \\ \Phi_{\mathrm{dyn}} &= \frac{\mu_0}{I}\iiint_{\mathrm{V}} \chi_{y'y'}h_{y'}^2+(\chi_{y'z'}+\chi_{z'y'})h_{y'}h_{z'}+\chi_{z'z'}h_{z'}^2\,dx'dy'dz'.\end{aligned} \tag{2.29}$$

Here, $\boldsymbol{h}(y',z')$ refers to the magnetic field described by the Karlqvist equations (see Eq. (2.27)). We can reduce the equation by omitting the middle term in the integral for reasons of symmetry. Furthermore, when we consider $d_{\mathrm{FM}} \ll w_{\mathrm{cc}}$, i.e., the thickness of the sample is much smaller than the width of CC, we can take the limit $h_{y'z'}(y',0) = \lim_{z'\to 0} h_{y'z'}(y',z')$. As the sample extends far into the ground plane (width of sample $b \gg w_{\mathrm{cc}}$), the volume integral along y' can be considered as infinite. These steps will eventually reduce the dynamic magnetic flux to

$$\Phi_{\mathrm{dyn}} = \mu_0 I\frac{l\cdot d_{\mathrm{FM}}}{4w_{\mathrm{cc}}}(\chi_{y'y'}+\chi_{z'z'}). \tag{2.30}$$

This magnetic flux is associated with an inductance $L = \Phi/I$ which depends on the geometrical parameters of the sample and CPW and the magnetic susceptibility

$$L = \mu_0\frac{l\cdot d_{\mathrm{FM}}}{4w_{\mathrm{cc}}}(\chi_{y'y'}+\chi_{z'z'}). \tag{2.31}$$

After having discussed the induction of the CPW with the sample, we now want to relate it to the VNA measurement. The complex transmission parameter S_{21} relates the voltage going into Port 2 with the voltage sent from Port 1, such that we can write:

$$S_{21} = \frac{V_2}{V_1} = \frac{|V_2|}{|V_1|}e^{i\phi}. \tag{2.32}$$

Here, ϕ represents the phase difference between the incoming and outgoing microwave signal. The transmission through an unloaded CPW (without sample) S_{21}^0 is determined by the microwave cables, endlaunches and the CPW itself. The sample adds a purely inductive contribution $i\omega L$ to the inductance L in series with the impedance Z_0 of the empty CPW. In a voltage-divider model the transmission change due to the resonant excitation of spin dynamics in the sample is thus [51]

$$\Delta S_{21} = \frac{1}{2}\frac{V_{\mathrm{ind}}}{V_1} = -\frac{1}{2}\left(\frac{i\omega L}{Z_0+i\omega L}\right) \approx -\frac{i\omega L}{2Z_0}. \tag{2.33}$$

The approximation holds for $Z_0 \gg \omega L$ which is satisfied for our samples exhibiting resonance frequencies in the GHz regime and inductances of roughly 10^{-15} – 10^{-13} H. The factor $1/2$ accounts for V_{ind} being the voltage between the CC and GND instead of a voltage between port 1 and 2. The additional contribution from

the sample alters the transmission such that the transmission change and the total microwave transmission can be written as:

$$\begin{aligned} \Delta S_{21}(\omega, H_0) &= \frac{S_{21}(\omega, H_0) - S_{21}^0(\omega)}{S_{21}^0(\omega)} \\ S_{21}(\omega, H_0) &= S_{21}^0(\omega)(1 + \Delta S_{21}(\omega, H_0)) \end{aligned} \tag{2.34}$$

In the OOP case $\chi_{z'z'} = \chi_{zz}$ vanishes due to the parallel alignment of the respective driving field's component with regards to H_{eff}. Thus the transmission parameter (see. Eq. (2.33) and (2.34)) can be connected to the susceptibility via the inductance (see Eq. (2.31)) in a trivial form to fit actual transmission raw data:

$$S_{21}(\omega, H_0) = S_{21}^0(\omega, H_0) + iA\frac{\chi(\omega, H_0)}{M_S}. \tag{2.35}$$

Here, the background $S_{21}^0(\omega, H_0)$ is assumed to be a complex linear background dependent on the applied magnetic field and A is a scaling parameter that absorbs the prefactors appearing in Eq. (2.33) and (2.31). For the IP case, when assuming small linewidths ($\Delta H \ll H_0, M_{\text{eff}}$), $\chi_{z'z'}(= \chi_{yy})$ is connected to $\chi_{y'y'}(= \chi_{xx})$ via the elipticity with $\chi_{y'y'} \cdot H_0 \approx \chi_{z'z'} \cdot (H_0 + M_{\text{eff}})$.

2.4 Spin Waves

For the described FMR all magnetic moments precess homogeneously and in phase ($k \to 0$ and $\lambda \to \infty$). However, when the excitation is inhomogeneous the spins precess with different phases resulting in so called spin waves or magnons (see Fig. 2.4 a)). These excitations find strong relevance at nonzero temperatures as thermally excited magnons are responsible for the reduction of the effective saturation magnetization. Due to the precession of magnetic moments they are intrinsically tilted away from its equilibrium position reducing the corresponding magnetization component. In general, the wave character allows to attribute a wavelength λ and a wavevector $k = 2\pi/\lambda$, which in case of the previously discussed FMR leads to $\lambda = \infty$ and $k = 0$. When considering propagating spin waves with $k \neq 0$ we will see that such excitations enable information transport via the magnetization [9, 10]. Such and more aspects are studied in the research field of magnonics. It focuses on spin-wave based phenomena that may be useful for future information processing technologies. Both the spin-wave phase [52–55] and the spin-wave amplitude [10, 56, 57] were shown to be able to encode and transport information. However, many challenges for fabrication and efficiency remain for both insulating and metallic systems.

Other than in the previous sections, when considering spin waves with $k \neq 0$ the exchange interaction between spins and dynamic dipole interactions become

relevant. On the one hand, the exchange interaction results in an additional effective exchange field [19, 58]

$$\mu_0 H_{\mathrm{ex}} = \frac{2A}{M_{\mathrm{S}}} k^2 \tag{2.36}$$

with exchange stiffness constant A. It becomes directly apparent that this contribution is isotropic and gains importance with increasing k-values. On the other hand, the dynamic dipolar fields for IP magnetized thin films with $kd \ll 1$ derived in Ref. [23] can be written as:

$$\begin{aligned} H_{\mathrm{x}}^{dip} &= M_{\mathrm{S}} \left(1 - \frac{1 - e^{-kd}}{kd}\right) \sin^2(\phi) \\ H_{\mathrm{y}}^{dip} &= M_{\mathrm{S}} \frac{1 - e^{-kd}}{kd}. \end{aligned} \tag{2.37}$$

Here, the coordinate system is chosen analogous to the IP case in Chap. 2.2 such that $\boldsymbol{z}$ points along the net magnetization direction, $\boldsymbol{y}$ points along the surface normal and $\boldsymbol{x}$ is IP perpendicular to the net magnetization direction. ϕ thus represents the in-plane angle between the magnetization $\boldsymbol{M}$ and the wavevector $\boldsymbol{k}$. When we consider wavevectors with $\boldsymbol{k} \parallel \boldsymbol{M}$, H_{x}^{dip} vanishes, whereas it becomes the largest when the spin wave propagates perpendicular to $\boldsymbol{M}$. It becomes evident, that especially the dipolar contributions (static and dynamic) lead to a geometry dependent and complex spin-wave manifold that depends on various factors. Relevant aspects are the angles between the magnetization direction, the propagation direction and the surface normal, the applied magnetic field and the material parameters. In this thesis we will make use of IP spin waves. Kalinikos and Slavin formulated the famous equation (now known as Kalinikos-Slavin equation) that describes the resonance frequency for IP spin waves in thin films [23]:

$$\omega = \gamma \mu_0 \sqrt{\left(H_0 + H_{\mathrm{ex}} + H_{\mathrm{x}}^{dip}\right)\left(H_0 + H_{\mathrm{ex}} + H_{\mathrm{y}}^{dip}\right)} \tag{2.38}$$

It may be noted that in order to obtain such an analytical formulation an ellipsoidal shape has to be assumed due to otherwise inhomogeneous demagnetization. In the present, simplified case uniaxial anisotropy is omitted and static demagnetization contributions in the plane vanish for infinitely extended thin films. The two special solutions $\phi = 0$ and $\phi = \pi/2$ describe two different kinds of spin waves which are often referred to as backward volume (BV) mode and Damon-Eshbach (DE) mode [59], respectively. While the BV wave has a negative group velocity - hence the name - and is localized within the thin film volume, the DE wave is a magnetostatic surface wave localized at either the top or bottom side of the thin film, depending on the propagation direction $\pm\boldsymbol{k}$.

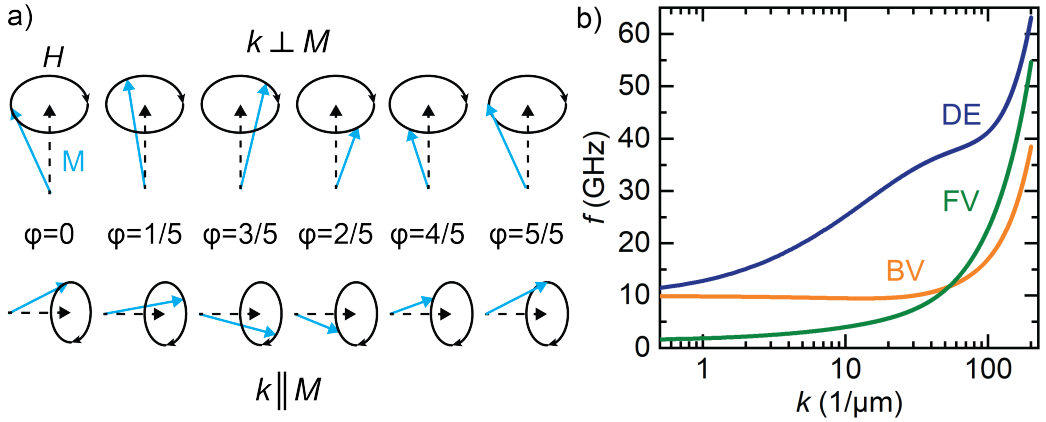

Fig. 2.4. – a) Schematic of spin waves with a wavelength of five lattice constants. The presentation of $\boldsymbol{k} \perp \boldsymbol{M}$ and $\boldsymbol{k} \parallel \boldsymbol{M}$ clarify the geometric relevance for the interaction between adjacent magnetic moments. b) Dispersion relation of the most prominent spin-wave modes. The Damon-Eshbach (DE) mode and the backward volume (BV) are excited when the net magnetization lies in the plane. The area between the two dispersions covers the possible spin-wave manifold for arbitrary ϕ. For complementary reasons the forward volume (FV) mode is plotted, which describes spin waves in thin films when the magnetization points out of the plane. Depending on the geometry, the frequencies below the dispersion correspond to the so-called spin-wave band gap. The DE and the BV mode were calculated using Eq. (2.38) and parameters $\mu_0 H_0 = 50\,\mathrm{mT}$, $\mu_0 M_S = 2.35\,\mathrm{T}$, $A = 26 \times 10^{-12}\,\mathrm{J/m}$, $d = 30\,\mathrm{nm}$ and Landé factor $g = 2.05$ which match the material parameters from CoFe thin films. The FV mode was calculated with Eq. (2.39), where the same material parameters are employed but the external field was set to $\mu_0 H_0 = 2.4\,\mathrm{T}$.

Fig. 2.4 a) shows a schematic sketch of two spin waves with k being either perpendicular or parallel to the magnetization direction. Panel b) shows the dispersion relation of the two described modes. The area between DE and BV waves represents the possible energies of the spin waves propagating in any IP direction which defines the spin-wave manifold. The unavailable frequency range in IP geometry below the BV-minimum is often referred to as the spin-wave gap. For the figure a typical parameter set of a CoFe thin film was used with $\mu_0 M_S = 2.35\,\mathrm{T}$, $A = 26\,\mathrm{pJ/m}$, $g = 2.05$, $H_0 = 50\,\mathrm{mT}$ and $d = 30\,\mathrm{nm}$. Additionally, the so-called forward volume (FV) is shown, which is excited when the magnetization is aligned parallel to the surface normal. As all possible wavevectors are perpendicular to $\boldsymbol{M}$, this configuration is isotropic. The corresponding equation can be found in [19, 23]:

$$\omega = \gamma\mu_0 \sqrt{(H_0 - M_S + H_{ex}) \left(H_0 - M_S + H_{ex} + M_S \left(1 - \frac{1 - e^{-kd}}{kd} \right) \right)}. \quad (2.39)$$

Here, the additional term "$-M_S$" stems from the static demagnetization in OOP direction.

As can be seen from Fig. 2.4 b) and Eq. (2.36), the resonance frequency increases quadratically with increasing k-vector. Thus, the exchange contribution dominates for large k-values. Simultaneously, at large values for k (or reciprocally

small wavelengths) the stray fields between the magnetic moments become smaller. Consequently, the dynamic dipolar contributions become less relevant and the parabolic dispersion is obtained with

$$\omega = \gamma\mu_0(H_0 + H_{ex}) = \gamma(\mu_0 H_0 + \frac{2A}{M_S}k^2). \tag{2.40}$$

This limit ($H_{ex} \gg H_x^{dip}, H_y^{dip}$) describes the so called exchange spin waves. Especially due to the small wavelengths and its high group velocities for possible technological devices the efficient excitation and detection of such exchange spin wave is drawing much attention [10,60–65]. In a collaboration with Hanchen Wang and Haiming Yu we exploit low damping CoFe for exchange spin wave creation (see Chapter 3.4.3).

The group velocity of the spin waves can generally be calculated from the slope of the dispersion relation with

$$v_g = \frac{\partial\omega}{\partial k} \tag{2.41}$$

and determines the speed at which information can be transferred. However, magnetic damping causes a significant relaxation of the spin-wave excitation and thus a finite life time of the desired magnons. This characteristic lifetime is given by $\tau = 1/\Delta\omega$ with [15,23,66]

$$\Delta\omega = \alpha\gamma\mu_0 \left(H_0 + H_{ex} + \frac{1}{2}\left(H_x^{dip} + H_y^{dip}\right)\right). \tag{2.42}$$

It thus becomes apparent that the characteristic decay length of spin waves $\lambda_{prop} = v_g\tau$ is directly linked to the magnetic damping of the sample. Hence, for spin-wave propagation experiments materials with low Gilbert damping parameters are highly favorable, which motivated the work presented in this thesis.

2.5 Micro-focused Brillouin Light Scattering

Brillouin Light Scattering (BLS) is a well established measurement technique [67] that allows the detection of spin-wave excitations. It is a sensitive tool to measure coherent and incoherent spin waves [68]. Additionally, the BLS technique can be modified in various ways [67,69] to extract not only energy- [67] and wavevector- [70,71] but also temporal- [72,73], spatial- [69,74,75] and phase information [69,76] of quasi particle excitations.

The main principle is the inelastic scattering of photons off quasi particles in a solid. In general these include phonons, polaritons and magnons, however this work is restricted to the study of magnons only. The photons scattering inelastically at a magnetic sample can either create or annihilate spin excitations via the Stokes and anti-Stokes process, respectively. Due to energy and momentum conservation

the outcoming photons inherits information of the magnon it interacted with. Fundamentally, we can write:

$$\begin{aligned} \omega_{\text{out}} &= \omega_{\text{in}} \pm \omega_{\text{sw}} \\ k_{\text{out}} &= k_{\text{in}} \pm k_{\text{sw}} \end{aligned} \tag{2.43}$$

Here, ω_{out} and k_{out} represent the frequency and momentum of the scattered photon, wheres the subscript "in" refers to the photon before the scattering process and "sw" refers to the spin wave or magnon. A schematic of these processes of creation ("$-$") and annihilation ("$+$") is shown in Fig. 2.5 a). The magnons excited by microwave fields in ferromagnets live in the GHz regime, such that the change on the probing laser light ($\geq 10^2$ THz) is very small. A very sensitive apparatus is required to reliably detect the changes of an order of magnitude of roughly 10^{-5} and a monochromatic light source with small linewidth is required to obtain a stable photon frequency. The demand for the high sensitivity can be satisfied by a (3+3) pass tandem Fabry-Perot interferometer (TFPI) shown in Fig. 2.5 b). Two Fabry-Perot interferometer (FPI) are used through which the laserbeam is guided six times in total in order to achieve the required contrast. For a certain etalon distance L_1 of the first FPI only laser wavelengths λ that match the condition $L = n\lambda/2$ can pass the filter. All other frequencies are canceled out due to destructive interference of the back and forth reflected light. By moving the stage and hence the etalon distance the frequency spectrum can be probed. The resulting transmitted frequencies match the elastically scattered light and the (anti)-Stokes peaks. After a scan of $\lambda/2$ the signal repeats. This range is often referred to as free spectral range (FSR) $f_{\text{FSR}} = c/2L_1$, with c being the speed of light. The second FPI installed at an angle α and thus having an etalon distance $L_2 = L_1 cos(\alpha)$ allows to suppress higher order signals after passing the FSR. This can be explained as the stage scan is correlated with a frequency scan which is slightly different for the two FPIs. Fig. 2.5 c) shows the transmitting signals for both FPIs and depicts the product of the two when the light passes the TFPI. The TFPI developed by J. R. Sandercock [77] thus allows a high contrast measurement of small photon frequency shifts where higher order transmissions are effectively suppressed. Only the original frequency (Rayleigh peak for elastically scattered photons) and the Stokes and anti-Stokes peak with frequency shifts Δf can thus be transmitted. A single photon detector is used to quantify the signal intensity.

The BLS measurements presented in Chapter 3 were performed in a collaboration with the Helmholtz-Zentrum Dresden-Rossendorf. Tobias Hula recorded the BLS spectra at the setup in Dresden. A schematic is shown in Fig. 2.6. The phase sensitive micro-focused BLS setup is able to merge spatial information and recover wavevector resolution at the same time [69]. A microscope objective allows to obtain a spatial resolution of $\lessapprox 400$ nm. This allows to scan over the sample and measure spin-wave intensities depending on the distance with respect to an

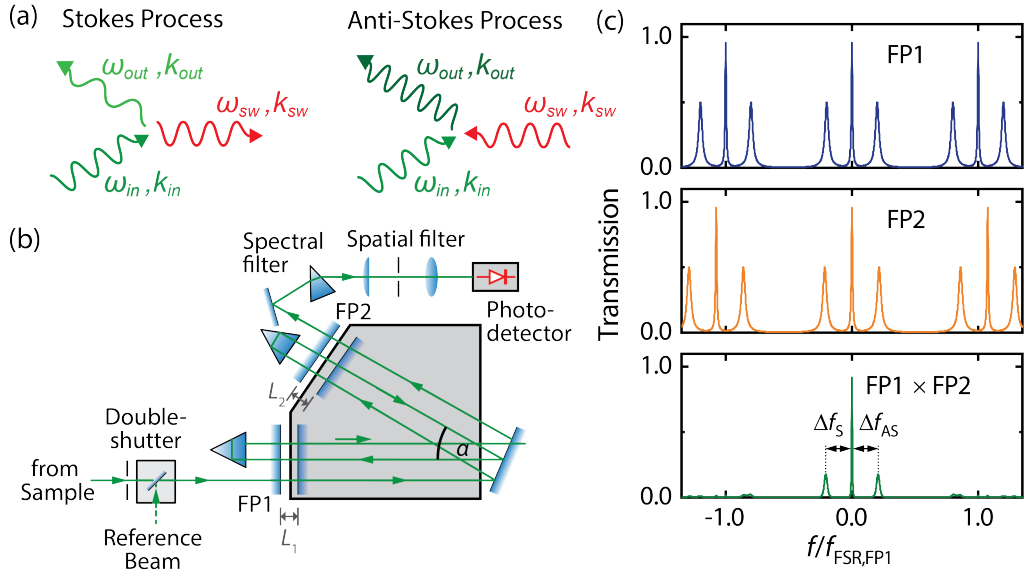

Fig. 2.5. – a) Stokes and anti-Stokes scattering process where an incoming photon with frequency ω_{in} and momentum k_{in} creates or annihilates a magnon, respectively. b) Schematic of the TFPI stage. The laser beam is guided three times through each FPI to achieve a high signal contrast. The use of two FPI with a tilting angle α allows to suppress higher order transmissions. c) Individual transmission showing Rayleigh-, Stokes- and anti-Stokes peaks through FP1 and FP2. The different etalon distances L_1 and L_2 result in a different stage translation to frequency relation. The product of both effectively returns only one signal triplet with a frequency shift depending on the magnon frequency. The figure is adapted from L. Liensberger [29].

exciting microwave antenna. Due to the focused light beam magnons with various wavevectors are collected and wavevector resolution is sacrificed. However, phase information can be retained by using a reference beam with constant phase and its frequency matching the frequency of the inelastically scattered photons. The probing light is sent through an electro-optical modulator (EOM) that is driven by the same source as the antenna that excites the spin waves. BLS is a phase-sensitive mechanism such that the scattered photons maintain the same phase information as the corresponding spin wave. As the phase of the propagating spin-wave mode varies depending on the distance with respect to its origin so does the phase of the scattered photons. By allowing the backscattered light to interfere with the reference beam after passing a polarizer constructive and destructive interference depend on the laser spot position. Using this method, the wavefronts can be visualized such that wavelength and corresponding wavevector are obtained. Hence, the dispersion of the investigated spin wave can be mapped in the operating frequency range of the EOM. More detailed and technical aspects regarding BLS can be found in Refs. [29, 69, 77] and references therein. For this thesis the phase sensitive microfocused BLS technique was used to obtain the spin-wave dispersion and spin-wave propagation lengths. It is thus possible to relate the characteristic decay length found in our structured samples with the low Gilbert damping in CoFe.

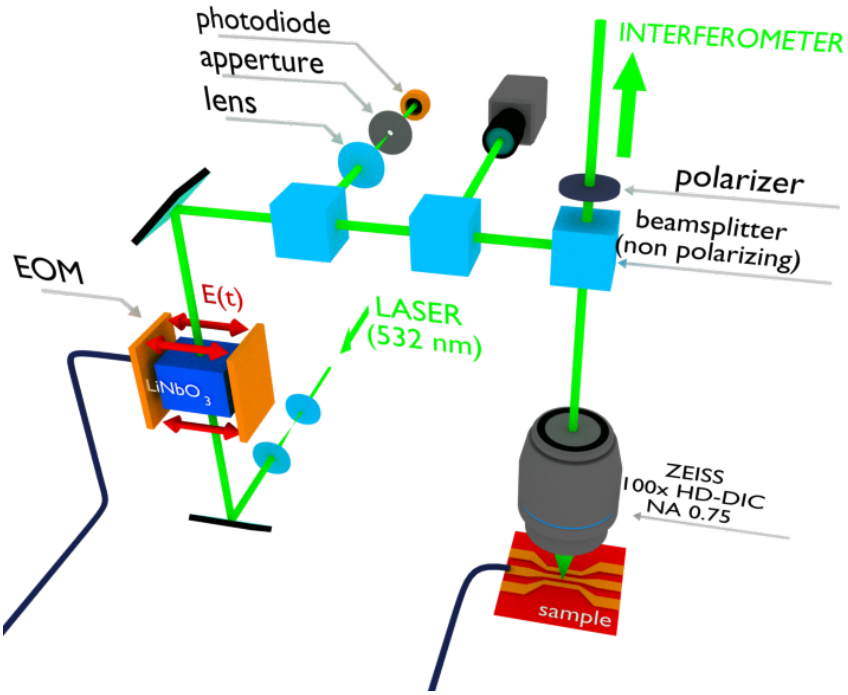

Fig. 2.6. – Schmatic of the phase resolved micro focused BLS setup. The laser is modulated by the EOM driven at the same frequency as the microwave antenna used for spin-wave excitation. The modulated reference beam that is reflected at the sample surface and the inelastically scattered light pass the non polarizing beamsplitter. As both beams have a 90° polarization shift with regards to each other they are brought to interference by an additional polarizer under 45°. An additional photodiode and camera are for operational purposes only. Figure kindly provided by Helmut Schultheiss (private communication).

Low Damping CoFe Thin films for Magnetodynamic Applications

3

The use of magnetization and its GHz frequency dynamics in nano-scaled devices for computational technologies is an intriguing approach to find possible novel applications in the field of information processing and storage [9, 10, 12, 13]. Even in quantum technologies the implementation of magnon-based quantum-coherent operations are considered [78]. At present, tunnel magnetoresistance (TMR) [79] - the magnetic alignment dependent tunneling resistance between two ferromagnetic layers - is used for read-heads of hard disk drives. Such magnetic tunnel junctions are also used for magnetic random access memory (MRAM) as a non-volatile memory. Further phenomena investigated in the field of spintronics like spin orbit torque or spin transfer torque RAMs are being employed for developing new generations of non-volatile memory applications [80]. For such devices fast switching times of the magnetization direction is of importance which demands a precise tuning of the relaxation inherent to the magnetization dynamics. The relaxation parameter is often described phenomenologically by the Gilbert damping constant α_G [21] as many different mechanism like scattering of magnons with other (quasi-)particles [81] or induction can dissipate energy from an excited magnetization motion. While such switching processes exhibit an optimum value for fast magnetization reversal [82] other aspired applications based on e.g. spin waves benefit from vanishing damping constants [9, 10]. The propagation of spin waves is limited by their lifetime emerging from magnetic damping and thus confines its implementation to small length scales. As a consequence, the investigation of spin wave based phenomena is most prominently based on the record low damping ferrimagnetic insulator Yttrium Iron Garnet (YIG) [9, 53, 61, 75, 83–88]. However, a large scale implementation of nano-patterned YIG structures is very costly and challenging. Additionally, due to its insulating property it is incompatible with current CMOS technology. Metallic systems on the other hand can be easily attached to electron based applications and entail easy fabrication possibilities. But alas, additional magnon-electron scattering leads to a faster magnetization relaxation. The Gilbert damping constant in YIG is reported to reach the $\alpha_G \sim 10^{-5}$ regime [89], whereas the most prominent metallic ferromagnets used for thin films like, e.g. Co, NiFe and CoFeB alloys exhibit much higher values $\alpha_G \sim (5-7) \times 10^{-3}$ [90–92]. A significant improvement was achieved by Schoen *et al.* [93] were the intrinsic damping of $Co_{25}Fe_{75}$ (the alloy will be abbreviated with CoFe throughout this work) was reported to reach down to $\alpha_G \approx 5 \times 10^{-4}$ which may endorse the alloy for various future work combining electrical conductivity with low magnetic damping. Within this chapter the low damping properties are extracted by broadband ferromagnetic

resonance (BBFMR) on CoFe thin films and the different damping contributions are elaborated. Its applicability for high spin wave propagation lengths is further confirmed by Brillouin Light Scattering experiments. The most important results presented in this chapter are as well published in Ref. [74].

3.1 Reduced Damping by Avoiding Spin Memory Loss

The seed layer of magnetic CoFe thin films and thus its growth conditions play an important role for the achievement of low damping parameters and reduced inhomogeneous linewidth broadening [94, 95]. Heavy metals with high spin orbit coupling and high spin Hall angles like, e.g. Pt and Ta are often used for magnetic thin films to exploit spin transfer or spin orbit torque effects [12, 96–102]. However, at the interface between the FM layer and the high spin orbit coupling materials spin memory loss acts as an additional loss channel for spin angular momentum [103–105]. It has been shown that the damping can be reduced significantly by the insertion of a additional spacer layers that exhibit vanishing SOC. The effect has been confirmed in various systems comparing bilayer and trilayer structures like, e.g. Co/Pt - Co/Cu/Pt [106] and Py/Ir - Py/Cu/Ir [107]. The effects of spin memory loss have further been investigated in various heterostructures, like e.g. Pd/Cu, Pt/Cu [108] and Ta/Py/Pt trilayers [109]. The insertion of Cu was shown to maintain its applicability for STT effects for current controlled magnetization dynamics [98, 100] and is thus a useful additive for optimized damping properties.

The above mentioned reports in literature regarding its influence on the relaxation is reproduced in Fig. 3.1 for CoFe based multilayers. Here, the Gilbert damping parameter of two sample series consisting of Ru(1.5)/CoFe(5)/Pt(t) and Ru(1.5)/CoFe(5)/Cu(2)/Pt(t) is compared. The Ru layer is used to prevent oxidation of CoFe by the thermally oxidized Si substrate. Even though this protective layer might contribute to the overall damping within the heterostructures, its contribution can be assumed to be constant for both sample series. It thus does not play a role for the comparison of the Gilbert damping parameter of the two series involving inclusion or exclusion of a Cu spacer layer. For very thin Pt thicknesses a finite ratio of the spin angular momentum which is transferred from the CoFe to the Pt via spin pumping [110] is reflected back to the FM layer. Thus, it does not contribute to the relaxation process and the damping decreases for very thin Pt layers as reflection gains importance. For large Pt thicknesses t the damping parameter saturates as the spin angular momentum pumped from the CoFe into the Pt is absorbed entirely. In this saturated regime a reduction of α_G by a roughly 40 % becomes visible when introducing an additional Cu spacer in between. Such a significant decrease aligns well with observations in literature [106, 107, 111]. How-

ever, a phenomenological estimation of the spin diffusion length in Pt with a fit to $\alpha_G = \alpha_{sat} - c\exp(-t/\lambda)$ [107] results in an underestimation of $\lambda_{Pt,Cu/Pt} < 1\,nm$ when assuming an internal Gilbert parameter $\alpha_{int} = \alpha_G(0) = 0.0015$. Even when considering higher values of α_{int} - and thus phenomenologically accounting for spin memory loss - $\lambda_{Pt,Cu/Pt}$ remains below $\approx 1.6\,nm$.

A thorough analysis of the spin diffusion length of Pt in Py/Pt samples with a self-consistent approach by measuring spin-orbit torques and Gilbert damping by FMR yields $\lambda_{Pt} \sim 2.5\,nm - 6.7\,nm$) [109]. Very similar Berger *et al.* [109] where Py/Pt structures with $2\,nm \leq t_{Pt} \leq 20\,nm$ were analyzed, α_G hardly changes for Pt thicknesses down to 2 nm. Nonetheless, they are able to determine λ_{Pt} in their work [109] as the damping-like spin-orbit torque exhibits a larger characteristic length scale of increase and by the use of more detailed models for which they additionally determined the charge conductances of the samples and quantified the spin mixing conductance at the interface by a additional samples comprising a t_{Py} series.

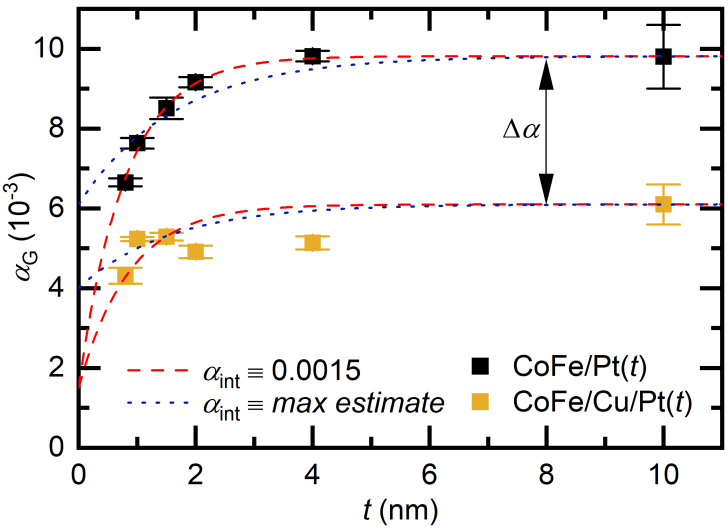

Fig. 3.1. – Gilbert damping parameters determined by BBFMR measurements on Ru(1.5)/CoFe(5)/Pt(t) and Ru(1.5)/CoFe(5)/Cu(2)/Pt(t) multilayers. A significant reduction of the magnetization damping is observed by introducing the additional spacer layer Cu.

Whilst the CoFe/Pt series in Fig. 3.1 compares well with Ref. [109] where a significant spin-memory loss contribution was found and the increased damping constants compared to the CoFe/Cu/Pt samples is consistent with the assumption of the presence of a spin-memory loss contribution $\Delta\alpha$, the data is not sufficient to have a more detailed discussion. At very low Pt thicknesses proximity polarization and inconsistent growth are expected to break the models described in Refs. [109, 112]. Unexpectedly, the CoFe/Cu/Pt series shows an almost constant α_G starting with thicknesses as low as $t_{Pt} \geq 1\,nm$ whose reason of "immediate" saturation is not clear. While such a behavior might align with the idea of an interface effect

as the spin-memory loss for this sample series as well, the lack of SOC in Cu is expected to result in negligible spin-memory loss contributions [103].

Despite the only qualitative and rough discussion, the data together with the available literature on the presence of spin-memory loss in similar sample structures [106, 107, 109, 111] allows to visualize the significant and beneficial effect of a spacer insertion regarding the reduction of magnetic damping. Within the work of a previous master thesis [32] it was found that instead of Cu other spacer layers, namely, Al can be used as well to obtain lower damping parameter values for BBFMR measurements in OOP geometry. In the following, Al spacers are employed for the multilayers that are used to distinguish different damping contributions in detail.

3.2 Separation of Extrinsic Damping Contributions

The excitation of magnetization and the resulting precession of magnetic moments can dissipate its angular momentum via various relaxation paths. Intrinsically, magnons within a ferromagnet can scatter with phonons in the material leading to the loss of angular momentum from the magnon to the phonon bath [113, 114]. Another intrinsic damping contribution stems from magnon-magnon scattering [115, 116], which allows the scattering of the FMR mode ($k = 0$) into spin waves modes ($k \neq 0$). A homogeneous excitation can thus experience an energy transfer into propagating waves. This contribution, however, can be suppressed by geometry when the magnetization is aligned with the external magnetic field parallel to the surface normal of a thin film. Due to the spin wave gap (see Chapter 2), energy conservation impedes the dissipation into other excitation modes at the low driving powers used throughout this work. For metallic systems additional contributions can be identified. Spin excitations can scatter with free electrons [117–121] leading to a further relaxation contribution compared to insulating magnetic materials. Furthermore, within itinerant samples the precession of magnetic moments induces eddy currents according to Lenz's rule which inherently try to counteract the motion of magnetization [46, 47]. This effect however, is shown to be negligible for the thin films used in this study due to their low thicknesses. Apart from the intrinsic mechanisms within the material, which - except from eddy-current contributions - are merged in an intrinsic Gilbert damping value α_0 in this work, other extrinsic phenomena play a crucial role for the relaxation of magnetic precession.

Depending on the sample structure, quality and the measurement technique additional contributions can lead to an increased relaxation rate of the magnetization precession. For FMR measurements the dynamic magnetization couples inductively to the coplanar waveguide and thus dissipates power. This "radiative damping" represents the equivalent of eddy currents but instead of the currents being present within the sample itself they are induced within the setup's waveg-

uide [15]. In heterostructure samples, if the ferromagnetic thin film is adjacent to a metallic or magnetic material, spin-angular momentum can be transferred via the interface [110, 122–132]. This spin pumping phenomenon thus relaxes the magnetic oscillatory motion. During the transport of spin-angular momentum at interfaces with spin orbit coupling an additional spin memory loss is observed where - as the term indicates - the spin information is rather lost than transferred [103–105]. While these mentioned extrinsic contributions are all Gilbert-like, i.e. a linear ΔH vs. f characteristic, further facets might play a role that lead to qualitative deviations of the linewidth dependence. Roughness and/or imperfections in the material lead to long range magnetic inhomogeneity inducing further magnon-magnon scattering processes. These contributions lead to and can be phenomenologically described by the inhomogeneous linewidth broadening [115, 133]. Addtionally, magnon-magnon scattering induces a more complicated, viscous damping that breaks the linear dependence [134–137].

A large variety of different relaxation paths of magnetodynamic motion becomes evident for both, insulating and itinerant ferromagnetic thin films. In the following, five different contributions to the total magnetic damping in CoFe thin films are resolved within a sample series of sputter deposited Ta(3)/Al(3)/CoFe(t)/Al(3)/Ta(3) heterostructures with varying FM thicknesses $1.4\,\mathrm{nm} < t < 26\,\mathrm{nm}$ (see fabrication details in Appendix A). Room-temperature FMR is employed to measure the magnetodynamic response to microwave excitations. Within the metallic ferromagnet Eddy currents are found to be negligible for the entire thickness range while spin pumping becomes the dominating contribution for very thin samples. At this end of the investigated thickness range also losses due to roughness and defects gain relevance as indicated by the inhomogeneous linewidth broadening which is reduced for thicker layers. For these higher values of t, radiative damping - being an intrinsic phenomenon of the measurement technique - becomes significant due to the increasing inductance. With help of the sample series an upper boundary for the intrinsic damping within the CoFe layers is quantified.

Fig. 3.2 a) and b) shows exemplary raw data of the measured field dependent microwave transmission S_{21} at 16 GHz for two samples with $t = 1.8\,\mathrm{nm}$ and $t = 26\,\mathrm{nm}$, respectively. The resonance field, linewidth and amplitude are extracted for a broad frequency range enabling the determination of several magnetic properties. The frequency dependent resonance fields of the two thin films are depicted in Fig. 3.2 c), where a fit to the Kittel equation (2.23) quantifies the effective magnetization M_{eff} and the Landé-factor g. The total measured Gilbert damping and the inhomogeneous linewidth broadening is extracted from the full-width-half-maximum linewidth of the resonance peak shown in Fig. 3.2 d) with Eq. 2.25. For the distinction of relaxation mechanisms, the damping parameter will be splitted into its different contributions $\alpha_{\mathrm{G}} = \alpha_0 + \alpha_{\mathrm{sp}} + \alpha_{\mathrm{eddy}} + \alpha_{\mathrm{rad}}$. Panel e) and

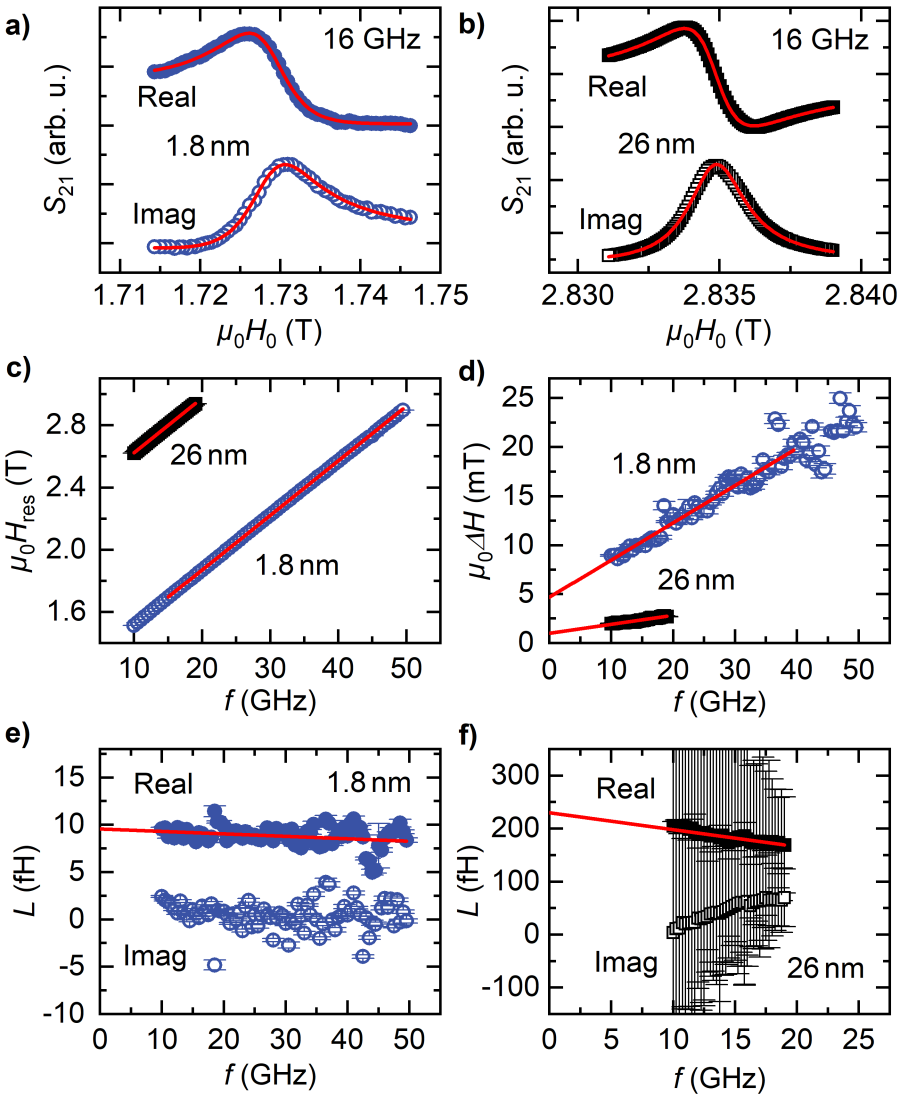

Fig. 3.2. – a),b) Exemplary raw data of the measured microwave transmission S_{21} of blanket Ta(3 nm)/Al(3 nm)/$Co_{25}Fe_{75}$ (t)/ Al(3 nm)/Ta(3 nm) samples with CoFe thickness $t = 1.8$ nm (a) blue symbols) and $t = 26$ nm (b) black symbols), respectively. The traces are recorded at 16 GHz with an applied magnetic field H_0 in OOP geometry. The red lines are obtained by fitting Eq. (2.26) to the data. c) and d) show the thus extracted resonance fields H_{res} and linewidths ΔH as a function of the applied microwave frequency, respectively. The fit errors shown as error bars are smaller than the symbol size. In c) H_{res} is fitted to Eq. (2.23) to extract the Landé-factor g and the effective magnetization M_{eff}. In d) ΔH is plotted vs. frequency. With a fit to Eq. (2.25) (red lines) the Gilbert parameter α_G and the inhomogeneous linewidth broadening H_{inh} are extracted. The linewidth of the $t = 26$ nm thick sample is shown in Fig. 3.4 on an expanded scale. e) and f) depict the complex inductance L of the two samples, where the red lines are linear fits to extract the zero-frequency inductance $\tilde{L}_0$. The zero-frequency offset is used to quantify the radiative damping contribution. The large error bars in f) stem from a larger uncertainty of the complex background offset due to the reduced field range of the resonance.

f) show the complex normalized inductance of the samples loaded on the CPW. By merging Eq. (2.33), (2.34) and (2.35) we obtain:

$$\frac{L}{\chi} = \tilde{L} = -\frac{2Z_0 A}{M_S S_{21}^0 \omega}, \tag{3.1}$$

Due to the effects of inverse spin-orbit torques the inductance is of the form $\tilde{L} = \tilde{L}_0 + \tilde{L}_1(\omega)$, where $\tilde{L}_0 \in \mathbb{R}$ and $\tilde{L}_1 \in \mathbb{C}$ [138]. As can be seen from Eq. (3.1) the determination of the saturation magnetization M_S is a crucial step. Its magnitude can be extracted from the thickness dependence of the effective magnetization M_{eff} shown in Fig. 3.3 a) [93]. The dipolar inductance $\tilde{L}_0$ can be extracted as the zero frequency offset of the real part of the impedance and used to quantify the radiative damping according to [15]

$$\alpha_{rad} = \frac{1}{4}\frac{\gamma\mu_0 M_s}{Z_0}\tilde{L}_0. \tag{3.2}$$

The obtained α_{rad} for the samples with varying thickness is shown in Fig. 3.3 b). The inductance due to AC dipolar fields scales linearly with the ferromagnetic layer thickness [138]

$$L_= \frac{\mu_0 l t_{FM}}{4 w_{cc}} \chi_{yy}(\omega, H_0)\eta^2(z, w_{cc}) \tag{3.3}$$

where, w_{cc} is the center conductor width, and η describes the spacing loss stemming from the finite distance z between the sample and the waveguide. The variations of sample to waveguide distance in the measurements by exchanging samples and slightly different clamping pressures each time scale the inductance for each installing individually, which is why the stringent linear dependence is not obtained in Fig. 3.3 b). However, the tendency of increased radiative contributions with increased thicknesses is clearly visible.

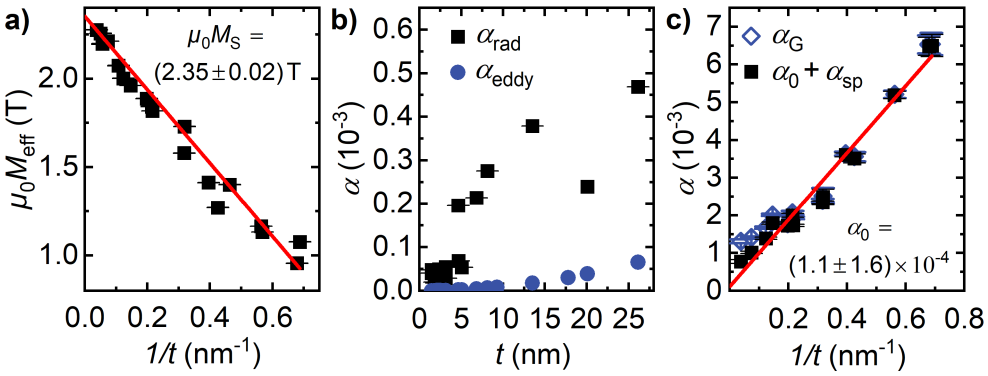

Fig. 3.3. – a) The effective magnetization $\mu_0 M_{eff}$ scales with reciprocal thickness indicating the presence of an uniaxial interface anisotropy. From the extrapolation to bulk thicknesses $t \to \infty$ the saturation magnetization M_S can be determined. b) Radiative and Eddy current contributions to the Gilbert damping parameter according to Eq. (3.2) and Eq. (3.4). c) The total Gilbert damping α_G as measured by FMR and the remaining intrinsic and spin pumping contribution after subtraction of the values shown in b).

Additional to the radiative damping, eddy current contributions are shown in Fig. 3.3 b) and were calculated according to [15]

$$\alpha_{\mathrm{eddy}} = \frac{\gamma \mu_0^2 M_s t^2}{16\rho}. \tag{3.4}$$

Here, $\rho = 340\,\mathrm{n\Omega m}$ is the estimated weighted resistivity value of CoFe films derived from 20 nm thin films of iron and cobalt as a reference [139, 140]. Thinner films are expected to exhibit higher resistivities which further reduces the expected eddy current damping.

Substracting α_{rad} and α_{eddy} from the total measured Gilbert damping α_{G} results in the remaining intrinsic (α_0) and spin pumping (α_{sp}) contributions to α_{G} shown in Fig. 3.3 c). The obtained $\alpha_0 + \alpha_{\mathrm{sp}}$ matches very well the expectation of linear scaling with reciprocal thickness due to the interface character of the spin pumping phenomenon. While the extrapolated bulk value ($t \to \infty$) returns the intrinsic damping α_0, the slope allows insight into the effective spin mixing conductance $g_{\mathrm{eff}}^{\uparrow\downarrow}$. By using a fit to [93]

$$\alpha_0 + \alpha_{\mathrm{sp}} = \alpha_0 + 2\frac{\gamma \hbar g_{\mathrm{eff}}^{\uparrow\downarrow}}{4\pi M_S}\frac{1}{t} \tag{3.5}$$

the obtained $g_{\mathrm{eff}}^{\uparrow\downarrow} = (5.5 \pm 0.3) \times 10^{18}\,\mathrm{m}^{-2}$ compares well to literature values [15]. However, the intrinsic $\alpha_0 = (1.1 \pm 1.6) \times 10^{-4}$ shows that the described approach lacks sensitivity for the present ultra-low damping values. In order to obtain a slightly more reliable upper boundary a second approach analyzing the thickest sample is performed.

In Fig. 3.3 c) the largest deviation from the liner spin pumping dependence is visible for the thickest sample with $t = 26\,\mathrm{nm}$. Thus, in order to quantify an upper limit, a linewidth analysis for this sample is shown in Fig. 3.4. By using Eq. (2.25) the different contributions to α_{G} and the additional $\mu_0 \Delta H$ can be subtracted leading to a reduction of the resulting linewidth. Thus, with this approach, the inhomogeneous linewidth broadening is considered as a separate contribution to the total linewidth. The step-by-step reduction of the linewidth in Fig. 3.4 visualizes the impact of the individual components. The obtained "intrinsic" linewidth can be fitted again with Eq. (2.25) and setting $\mu_0 H_{\mathrm{inh}} = 0$ such that an upper bound for $\alpha_0 \leq 4 \times 10^{-4}$ is obtained.

In conclusion, it is shown that for very thin films the dominating contribution to the magnetic damping stems from adjacent materials that can absorb spin angular momentum from the ferromagnetic layer. For "thicker" samples $t \gtrapprox 5\,\mathrm{nm}$ radiative damping stemming from the FMR measurement technique itself instead of an intrinsic sample property becomes non-negligible within the CoFe thin films investigated. Hence, the comparison of damping values of "thick" thin films determined with different measurement techniques thus requires the consideration

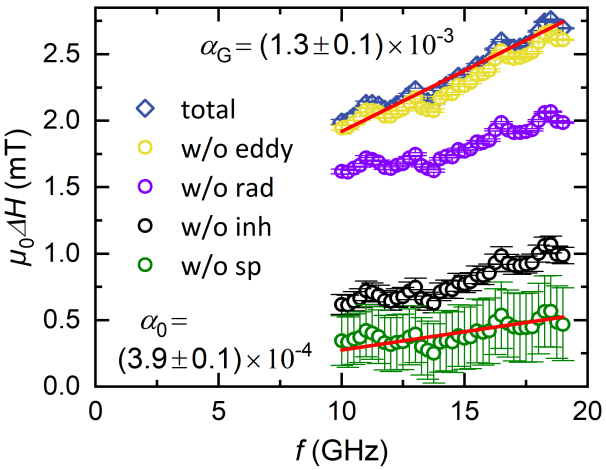

Fig. 3.4. – Linewidth of the sample with thickness $t = 26\,\text{nm}$ measured by FMR in OOP geometry. The blue diamonds depict the total measured linewidth, whereas the yellow, purble, black and green circles indicate the resulting linewidth after progressively subtracting Eddy current, radiative, inhomogeneous linewidth broadening and spin pumping contributions. An upper boundary of the intrinsic damping constant $\alpha_0 \leq 4 \times 10^{-4}$ is found.

of α_{rad}. Especially propagating spin waves relevant for the field of magnonics do not suffer from this contribution. For spin wave experiments the low damping properties achieved in the CoFe heterostructures are expected to increase magnon lifetimes. As a direct consequence, spin wave propagation lengths should be significantly increased compared to other metallic ferromagnets.

3.3 Spin-Wave Propagation in Low Damping CoFe

The low magnetic damping determined in blanket thin film ferromagnetic layers encourages further work that takes advantage of the high relaxation times of magnetic excitations. Spin wave propagation in a magnetic waveguide is a key for many magnonic applications [9, 10] yet limited due to finite decay lengths. Due to its record low damping of the insulating ferrimagnet YIG ($\alpha_G \sim 10^{-5}$) spin wave propagation distances of several mm are reported in "bulk" YIG crystals with thicknesses in the µm regime or above [141, 142]. However, when going to patterned thin films with layers of $\sim 20\,\text{nm}$ thickness, the characteristic propagation length scale drastically reduces to roughly 25 µm [75, 83, 89]. The insulating properties of YIG and the requirement of crystalline growth challenge its application for large scale technological applications. Metallic heterostructures on the other hand, enable compatibility with CMOS technology by their electrical conductivity. Furthermore, the possibility of polycrystalline structure without necessary annealing and easy fabrication steps via sputter deposition and already established lithographic patterning techniques render such type of multilayers even more attractive. With respect to CoFe, the low damping properties not only are expected to increase magnon lifetimes, but the high saturation magnetization

leads to dipolar spin wave velocities in the range of several km/s. Such speeds are much higher compared to values determined for YIG at different thicknesses and applied external magnetic fields [83, 143, 144]. The in this section presented results elaborate, that the same propagation length scales as in 20 nm YIG thin films can be achieved in the metallic thin film systems.

For this purpose two Pt(3)/Cu(3)/CoFe(26)/Cu(3)/Ta(3) thin films were sputter deposited (details about fabrication provided in Appendix A). One sample is unstructured for the characterization of material parameters by FMR, and the second sample is patterned with e-beam lithography. A 5 µm wide waveguide is structured for phase resolved microfocused Brillouin Light Scattering (μBLS) measurements [69]. Due to the higher spin wave velocity in the Damon-Eshbach geometry the external magnetic field is applied perpendicular to the narrow strip (see sketch in Fig. 3.6 a)). The μBLS data were recorded by Tobias Hula at the Helmholtz-Zentrum Dresden Rossendorf.

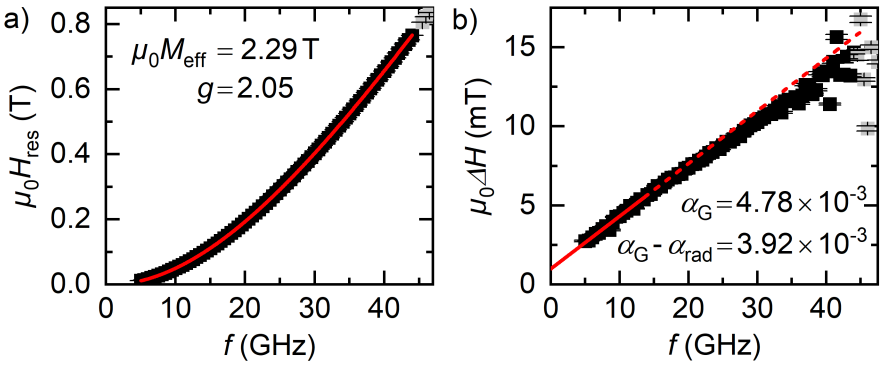

Fig. 3.5. – a) Ferromagnetic resonance fields for a broad frequency range in in-plane geometry of a unstructured Pt(3)/Cu(3)/CoFe(26)/Cu(3)/Ta(3) multilayer. With a fit to the in-plane Kittel equation (2.21) the effective magnetization $\mu_0 M_{eff}$ and the Landé-factor g can be extracted. b) The resonance linewidth is used to determine the Gilbert damping, where only the lower frequency part relevant for the optical measurements is considered. The slight slope change for larger frequencies indicates the presence of non-Gilbert like contributions like magnon-magnon scattering.

The uniform excitation measured on the blanket film is evaluated in Fig. 3.5. The obtained magnetic parameters effective magnetization $\mu_0 M_{eff}$, Landé-factor g and the Gilbert-like damping $\alpha_G - \alpha_{rad}$ are extracted from the resonance fields and linewidths shown in Fig. 3.5 a) and b), respectively. The increased damping compared to the sample series dicussed in Fig. 3.3 can be attributed to the different measurement geometry. In in-plane configuration additional magnon-magnon scattering is enabled, which otherwise is suppressed in thin films measured in OOP geometry [115, 116]. Together with the saturation magnetization $\mu_0 M_S$ determined in Fig. 3.3 a) these parameters are used to model the spin wave dispersion as measured in Fig. 3.6 b) with a simplified version of Kalinikos and Slavin's model for the studied modes with $\mathbf{k}_x \perp \mathbf{M}$:

$$f_{\mathrm{res}} = \frac{\mu_0\gamma}{2\pi}\sqrt{H_0 + H_\mathrm{d} + H_\mathrm{k} + M_\mathrm{s}\frac{1-\exp(-kt)}{kt}} \times \sqrt{H_0 + H_\mathrm{d} + M_\mathrm{s}\left(1 - \frac{1-\exp(-kt)}{kt}\right)}. \quad (3.6)$$

Here, The effective interface anisotropy field $\mu_0 H_\mathrm{k} = \mu_0 M_\mathrm{eff} - \mu_0 M_\mathrm{S} = -60\,\mathrm{mT}$ and the demagnetization field $\mu_0 H_\mathrm{d} = -18\,\mathrm{mT}$ is determined to match Eq. 3.6 to the obtained spin wave dispersion in Fig. 3.6 b). The value shows to be in good agreement with the simplified estimation of an ellipsoid of the CoFe stripe dimensions, where $\mu_0 H_\mathrm{d} \approx -12\,\mathrm{mT}$ [145]. The in-plane wave vector $k = \sqrt{k_\mathrm{x}^2 + k_\mathrm{y}^2}$, where the transversal component $k_\mathrm{y} = 0.31\,\mu\mathrm{m}^{-1}$ due to geometrical confinement is determined as a fitting parameter following the example in Ref. [146].

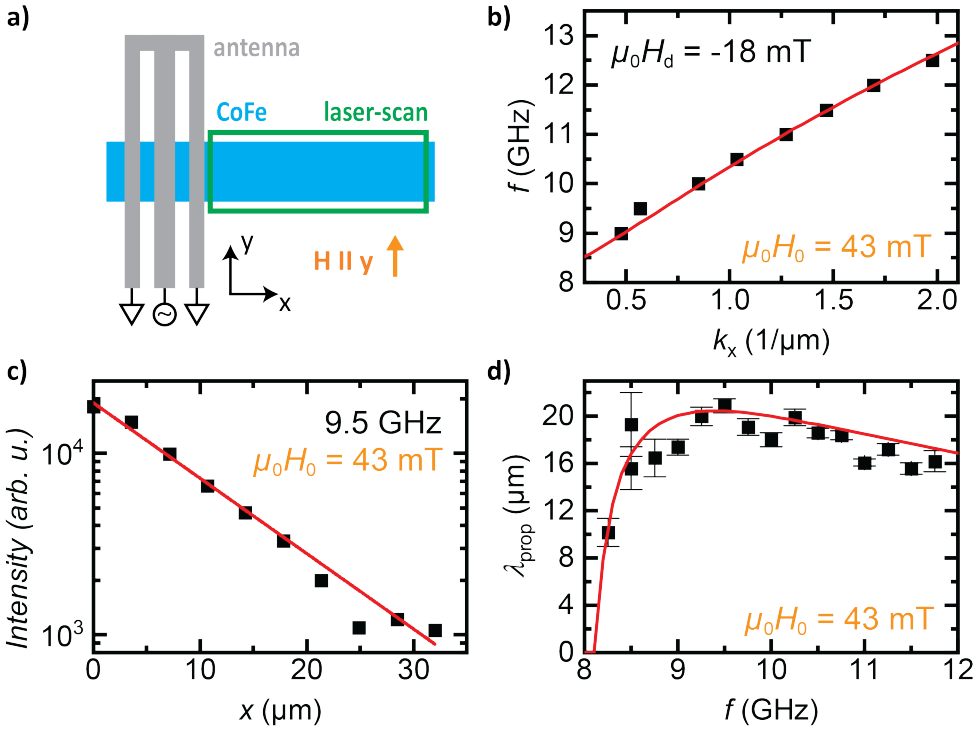

Fig. 3.6. – a) Sketch of the patterned CoFe waveguide with a CPW antenna on top. The field is applied perpendicular to the strip resulting in the Damon-Eshbash geometry for spin waves. b) The dispersion is fitted by the simplified model from Kalinikos and Slavin for the respective geometry (Eq. (3.6), where the determined parameters in Fig. 3.5 and M_S from Fig. 3.3 are used as input parameters. c) depicts the exponential intensity decay with distance from the antenna, where the signal across the y-direction is averaged to avoid mode-beating effects [147–149]. From a fit to Eq. (3.7) to the data with various frequencies the propagation length is extracted and shown in d). The red line indicates the modeled $\lambda_\mathrm{prop} = v_\mathrm{g}\tau$ by using the extracted magnetic material constants.

For the determination of the spin wave propagation length the μBLS intensity is recorded with a 2D scan over the CoFe strip. In order to suppress mode-beating effects, the intensity in y-direction is averaged over the entire width [147–149]. As a result. the x-direction dependence, shows the traveling spin wave with

decaying intensity. This distance dependence of the recorded μBLS intensity is shown in Fig. 3.6 c) with a fixed frequency $f = 9.5\,\mathrm{GHz}$ where $x = 0$ indicates the antenna position. A clear exponential decay is visible by which the characteristic propagation length scale can be obtained from a fit to [150]

$$I = I_0 \exp(-2x/\lambda_{\mathrm{prop}}). \tag{3.7}$$

Analogous quantifications are performed for various frequencies and the extracted λ_{prop} are depicted in Fig. 3.6 d). The observed frequency dependence is modeled by calculating the group velocity $v_{\mathrm{g}} = 2\pi\partial f_{\mathrm{res}}/\partial k$ and the lifetime of the spin wave $\tau = 1/\Delta\omega$. The resonance linewidth is obtained by [19]

$$\Delta\omega = \alpha\mu_0\gamma(M_{\mathrm{eff}}/2 + H_0 + H_{\mathrm{d}}), \tag{3.8}$$

where $\alpha = \alpha_{\mathrm{G}} - \alpha_{\mathrm{rad}}$ is the damping of the structured magnetic sample. The above quantified material parameters enable an almost perfect reproduction of the experimentally determined propagation length $\lambda_{\mathrm{prop}} = v_{\mathrm{g}}\tau$. A twofold conclusion can be drawn from the result. On the one hand, the well agreeing comparison of experiment and theory shows that the patterning of CoFe thin films is possible without altering the magnetic properties or damping constants proving easy fabrication of all-metallic magnonic devices. On the other hand, the consistency allows to predict the influence of further optimization steps.

From the dispersion relation shown in Eq. (3.6) a thickness dependence of f_{res} and thus, v_{g} becomes evident. Larger thicknesses are expected to result in higher group velocities and subsequently higher propagation lengths as depicted in Fig. 3.7 a) and b), respectively. The presented sample ($t = 26\,\mathrm{nm}$) exhibits a maximum $\lambda_{\mathrm{prop}} = (21 \pm 1)\,\mu\mathrm{m}$ and a calculated peak group velocity of almost $17\,\mathrm{km/s}$. A rough estimation for various thicknesses shows that these values are expected to be further optimizable for CoFe thin film layers.

In summary, different damping contributions of CoFe heterostructures could be separated confirming the record low intrinsic damping value for metallic ferromagnetic thin films [93]. While eddy currents are found to be negligible for a broad thickness range, spin pumping shows to be the dominant damping mechanism for the presented multilayers. For "thick" samples, radiative damping which is owned by the FMR measurement technique becomes non-negligible. The increased relaxation times compared to other ferromagnetic systems [90–92] results in high spin wave propagation lengths comparable to those obtained in patterned YIG thin films. However, the group velocities extracted from the dispersion show an enhancement of at least an order of magnitude [75,83]. The beneficial features of the optimized CoFe thin films, i.e. low damping and high saturation magnetization, provide the basis of further collaborations.

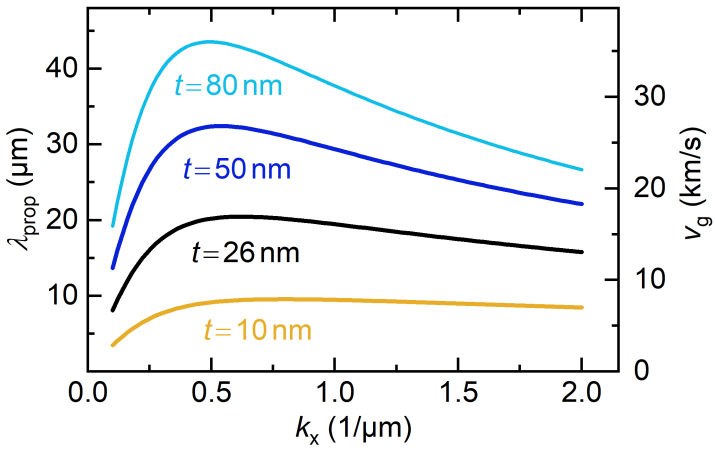

Fig. 3.7. – Thickness dependence of the spin-wave propagation length λ_{prop} and group velocity v_g determined from the given dispersion in Eq. (3.6) using the extracted material parameters for the system. The black line with $t = 26\,\text{nm}$ represents the case of the investigated multilayer structure.

3.4 Magnonic applications based on low-damping CoFe

The optimized sputter deposited heterostructures based on the low damping CoFe alloy motivated collaborations that benefit from its material properties. On the one hand, non-linear effects are investigated in CoFe waveguides which are feasible in the metallic multilayer due to the low damping property and in part published [151] or under review [73]. On the other hand, CoFe nanowires patterned onto a YIG thin film are shown to excite sub 50 nm spin waves in an antiparallel magnetization alignment allowing to downscale possible magnonic logic devices. While further projects exploiting CoFe thin films are intended, the most important results achieved in collaborations are discussed in short in the following.

3.4.1 Nonlinear Losses due to Four-Magnon Scattering

For the analysis of the magnetic damping contributions and the spin wave propagation lengths in CoFe thin films driving powers in the linear regime were employed. The excitation amplitude and thus spin wave intensities can be tuned by the driving powers used. While the characteristic propagation length scale maintains constant in the linear regime higher driving powers lead to four-magnon scattering that provides additional loss channels. The characteristic propagation lengths significantly shrink when entering the non-linear regime which was shown in a collaboration by Tobias Hula *et al.* [151]. In Fig.3.8 the measured μBLS spectra along a CoFe waveguide is shown for three different antenna driving powers. In the linear regime, the magnon population is restricted to the excitation frequency allowing for efficient transport properties. By increasing the driving power, four-magnon scattering parametrically excites and populates final states with higher and lower energies. Magnons from the main channel are thus lost to neighboring states and thus the total intensity of the initially excited state is reduced.

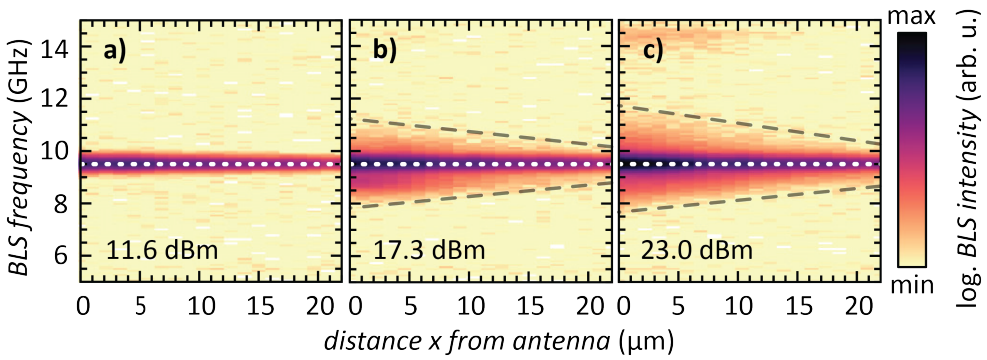

Fig. 3.8. – μBLS intensity spectra along the CoFe waveguide with increasing driving powers at a constant excitation frequency of 9.5 GHz a) to c). The grey dashed lines indicate the continuum of parametrically excited magnon states due to four-magnon scattering. The data was recorded by Tobias Hula and is published in Ref. [151].

3.4.2 Spin-Wave Frequency Comb

As the nonlinear four-magnon scattering represents a loss to the excited spin wave mode it is often considered parasitic or undesirable [152–154]. However, within the collaboration based on the optimized CoFe multilayers [73], we take active control of the scattering process in order to induce tunable spin wave frequency combs [73]. Optical frequency combs are important to metrology and significantly enhance precision of frequency measurements [155–157]. Four-magnon scattering can induce similar phenomena in solid state magnetism. The scattering process of two magnons with identical frequency f^i in an intial state i into two final frequencies f_1^f, f_2^f, where $f_{1,2}^f = f^i \pm \delta f$ can be manipulated with help of a second antenna. The transition probability depends on the population of the initial and final state, such that a second seed frequency f^s can populate a

desired final state and increases scattering rates to the corresponding spin wave channels [73, 158]. The tunability is shown in Fig. 3.9, where one antenna excites at a fixed frequency f^i and a second antenna induces a varying seed frequency f^s. It becomes evident that the frequency difference $\delta f = |f^i - f^s|$ dictates the frequency splitting of the entire frequency comb, where the magnitude also determines the efficiency/amount of further generated frequencies.

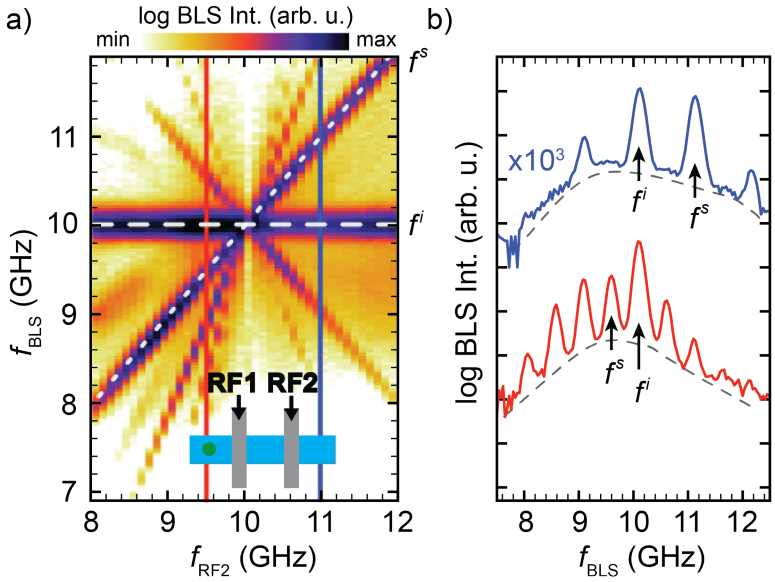

Fig. 3.9. – a) μBLS spectra for fixed frequency f^i at one antenna and a varying seed frequency f^s induced by the second antenna with identical excitation powers of 10 dBm. b) Examples of BLS spectra for two different fixed frequencies f^s. The grey dashed line shows the continuum of excited states due to four-magnon scattering. The data was recorded by Tobias Hula [73].

3.4.3 Short Wavelength Spin-Wave Excitation

Apart from nonlinear spin wave effects in CoFe waveguides based on dipolar spin waves, magnetic hybrid systems can be exploited to excite exchange spin waves. Such exchange magnons are highly favorable for the miniaturization of magnon-based logic [63] and high-speed processing [60]. However, using normal conducting antennas for the devices proof to be very inefficient in exciting and detecting such exchange spin waves [159]. Hence, other methods have to be employed. The implementation of small ferromagnetic stripes structured on another blanket magnetic material (e.g. YIG) has been shown to be able to approach the ultra-strong magnon-magnon coupling regime and by the same means excite low wavelength spin waves [64]. Such stripe architecture was also shown to act as a magnonic transducers to create unidirectional exchange spin waves [65].

In a collaboration with Haiming Yu's group, Hanchen Wang *et al.* makes use of nanopatterned CoFe strips (100 µm × 70 nm × 30 nm) deposited on blanket thin film YIG. Magnetic excitations in the CoFe wires induced by an antenna generate

high frequency stray fields and can impose spin torques in the adjacent YIG film [65, 132]. Using such a device architecture low wavelength spin waves with $\lambda \leq 50\,\text{nm}$ are excited in the YIG film and measured by spin-wave spectroscopy with stripline antennas. First results of the collaboration are currently under review and shown in Fig. 3.10 a). Here, the measured spectrum of the hybrid heterostructure is depicted. The external magnetic field is applied parallel to the CoFe stripes resulting in a Damon-Eshbach geometry from the spin waves in YIG. When sweeping from large negative fields to positive fields a significant qualitative change is observed at the sign change. While the YIG film has negligible in-plane anisotropy its magnetization follows the external magnetic field, whereas the shape anisotropy of CoFe pins its magnetization in its original orientation for fields up to almost 100 mT. In this antiparallel alignment of CoFe and YIG the magnetization precession in the wires efficiently excite exchange spin waves within the YIG film. By calculating the spin wave dispersion in YIG in Fig. 3.10 b) the spin wave mode with the highest excited frequency quantifies the lowest wavelength excited in the hybrid system.

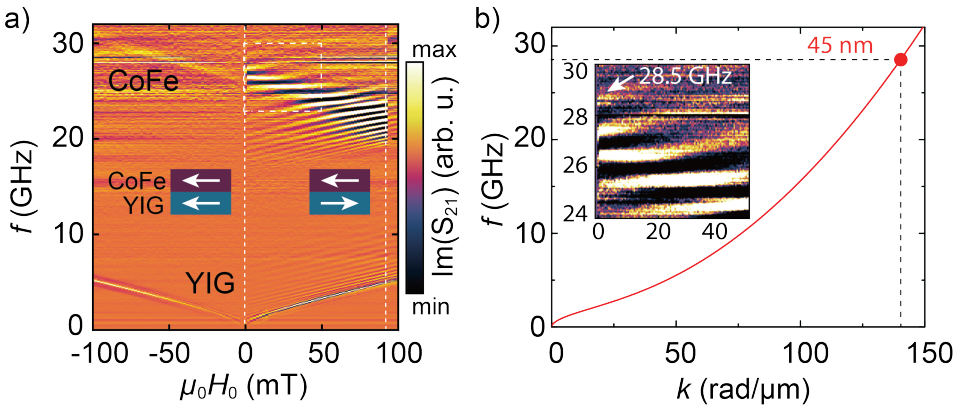

Fig. 3.10. – a) Travelling spin wave spectroscopy image of the CoFe-Yig hybrid system. For a parallel alignment of the magnetizations (negative fields) no exchange spin waves are excited. In the antiparallel case the situation changes significantly and various excitation modes are clearly visible. b) The extraction of the spin wave mode with the highest frequency shown in the inset (zoom-in frame from a)) allows to quantify its wavelength of 45 nm by using calculating the spin wave dispersion of YIG. The experiment and the calculation was performed by Hanchen Wang *et al*.

4 Magnetostatics and Domain Formation

In the previous chapter we focused on the microwave response of fully saturated ferromagnetic thin films. We employed a macrospin model to describe the entire ensemble of magnetic moments and determined the dynamic magnetic material parameters of CoFe thin films by BBFMR. While the presented work so far lies in the realm of magnonics in low damping CoFe, we show that optimized CoFe-based heterostructures exhibit intriguing static magnetic properties below saturation as well. By choosing proper multilayer systems including CoFe we show that skyrmions with previously unexpected field responses can be created. In this chapter we introduce the most important concepts and contributions for domain and skyrmion formation that are present within the investigated samples. Similar to Chapter 2, the fundamental concepts are already well established such that the following sections represent a short overview taken from literature [24, 25, 160].

4.1 Domain Formation

It is well known from everyday life that ferromagnets appear non-magnetic. For example, iron spoons or forks often show no or only negligible magnetic forces. Nevertheless, the exchange interaction is expected to align the moments in ferromagnets for temperatures below the Curie temperature and thus should result in a finite total magnetization of ferromagnetic objects. The reason for the apparently missing magnetism lies within the formation of magnetic domains. These domains are small regions within the ferromagnet where the magnetic moments align parallel to each other, but where the directions vary from domain to domain. From an outside perspective, the magnetizations of the different domains can cancel each other leading to vanishing stray fields. As mentioned in chapter 2, the formation of stray fields is accompanied with an energy increase, which is intrinsically the reason for domain formation. A simple visualization of the process is shown in Fig. 4.1 a) - d) where stray fields can be strongly reduced or even avoided due to a proper domain formation. However, the formation of domain walls, i.e., the transition region between two distinct domains, comes at an additional energy cost which complicates the process. On the one hand, exchange energy has to be paid due to the inherent reorientation of spins in the domain wall. On the other hand, also the misalignment with respect to the easy axis in presence of anisotropy increases the total energy. In the most simple case, these two energies, exchange and anisotropy energy, define the spatial extension of the domain wall. While higher exchange stiffness leads to larger domain wall

widths, higher anisotropy energy densities result in narrower walls. Nonetheless, additional contributions like the Dzyaloshinskii-Moriya interaction (DMI) which is explained further below might also influence the size and geometry of the domains and domain walls. In general, two distinct types of domain walls can be classified. When the reorientation between two domains happens in the plane parallel to the domain wall (i.e. a helical rotation) the wall is termed as a "Bloch-wall" (see Fig. 4.1 e)). In the second case, when the reorientation happens in a plane perpendicular to the domain wall (i.e. a cycloidal rotation) it is referred to as "Néel-wall" (see Fig. 4.1 f)).

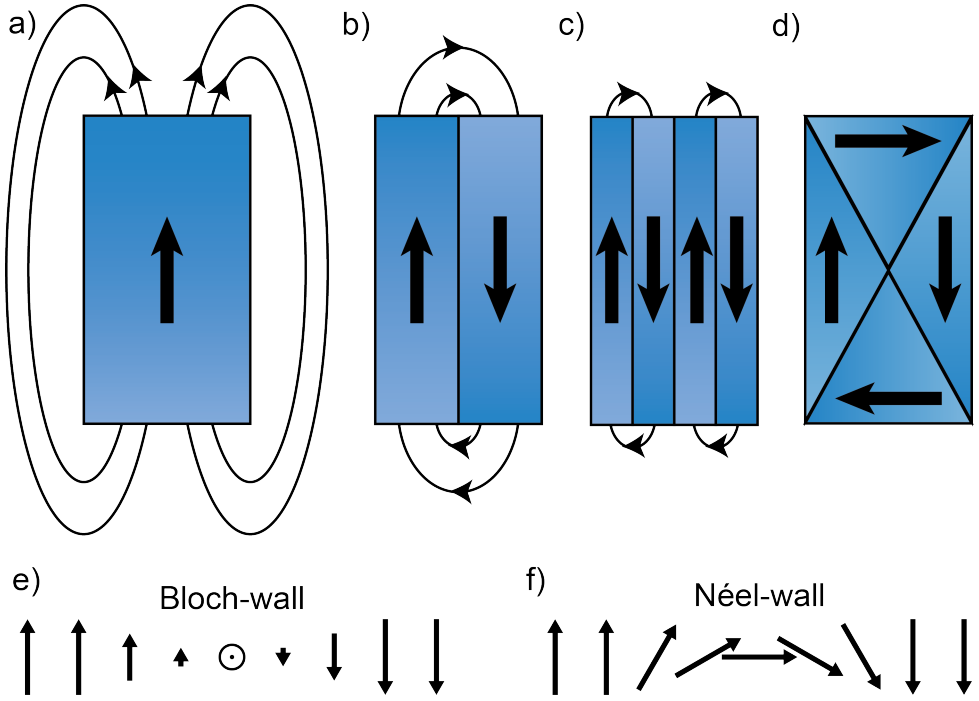

Fig. 4.1. – a) - d) The large stray field induced by a net magnetization and its resulting energy penalty can be reduced by the formation of smaller magnetic domains. However, domain wall energy resulting from the exchange energy has to be paid. In presence of anisotropies the domain size and shape can be redefined. If the anisotropic energy density is very large, domains with unaligned directions can become extinct leading to a remanent configuration as depicted in c) instead of d). The domain walls itself are regions of transition between two distinct domains which depending on its geometry are classified as Bloch-walls (e) and Néel-walls (f).

4.1.1 Uniaxial Anisotropy in Thin Films

The domain formation as depicted in Fig. 4.1 d), is, however, only favorable for very soft magnetic materials, where uniaxial anisotropic contributions are negligible. In the presence of an energetically favored direction, domains that do not align accordingly suffer from an additional energy cost and shrink in size. In case of strong anisotropies domains with magnetization not parallel to the easy axis can even disappear. The multilayer thin films studied in this thesis, comprise two major contributions to magnetic anisotropy, namely demagnetization and

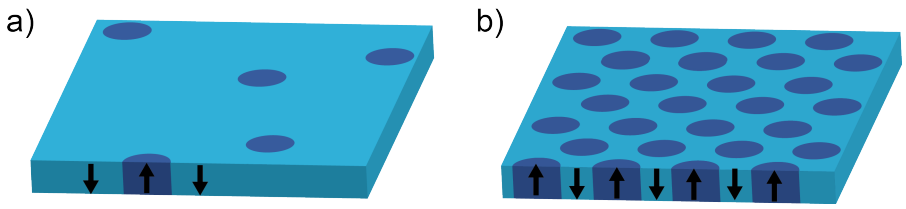

Fig. 4.2. – a) Individual bubbles in a homogeneous magnetization background of a thin film and b) a dense arrangement of bubble-shaped domains.

interface anisotropy. In our case, both of them oppose each other such that they are resumed in the effective anisotropy energy density constant K_{eff} (see Eq. (2.9)) similar to literature [161–165]. Especially in bubble forming systems made of thin films[3] usually a strong out of plane anisotropy is used. This way, the hard axis that is usually present in thin films due to demagnetization is turned into an easy axis by the uniaxial anisotropy when $K_{\text{u}} > \mu_0 M_{\text{S}}^2/2$. In literature, systems with $K_{\text{eff}} > 0$ are often referred to as perpendicular magnetic anisotropy (PMA) systems. Such a configuration induces a large amount of magnetic surface charges. However, the large amount of stray field can be maintained to a reduced level by the formation of "holes" in the homogeneously aligned magnetization. These antiparallel aligned domains in the uniform magnetic background enable flux closure and can thus become a metastable state of the system. Depending on the material properties and the external magnetic field the resulting domains can appear as individual magnetic bubbles (see Fig. 4.2 a)) or arrange in a dense lattice (see Fig. 4.2 b)). We will see that in more involved material systems periodic domain arrangements can even become the magnetic ground state. One of the most important ingredients for this phenomenon is the DMI.

4.1.2 Dzyaloshinskii-Moriya interaction

The DMI is an antisymmetric superexchange interaction between two magnetic spins that results in the canting of neighboring spins. Its contribution lowers the total energy for a perpendicular alignment as can be seen directly when considering the Hamiltonian:

$$H^{DMI} = \boldsymbol{D}_{12} \cdot (\boldsymbol{S}_1 \times \boldsymbol{S}_2)\,. \tag{4.1}$$

Here, $\boldsymbol{D}_{12}$ is the DMI vector and $\boldsymbol{S}_{1,2}$ represent the interacting spins. The interaction is mediated via a third atom with high spin-orbit coupling as shown in Fig. 4.3 a). In a ferromagnetic system, where the exchange interaction plays a crucial role, the

[3] Starting in the early 60s isolated bubble domains were investigated [166] and obtained increasing interest due to their potential application in information storage technologies [160, 167, 168]. Even though isolated bubble devices reached the point of useful commercialization they did not penetrate fully into computational technology. After a rest in research interest as bubble memory did not prevail, recent findings [161, 169–171] initiated new hopes for technological relevance of small circular shaped domains.

competition of direct exchange and DMI results in a spin canting whose canting angle depends on the ratio of the two interactions. Dzyaloshinsky[4] [172] and Moriya [173] were the first ones to explain the weak ferromagnetism that was observed in antiferromagnets due to a slight canting of the magnetic moments. The previous assumption of ferromagnetic impurities inside the antiferromagnets was thus lifted by the "antisymmetric part of the anisotropic superexchange". As the description indicates, it strongly depends on geometry or in other words symmetry. The spin-orbit coupling induced interaction only appears when inversion symmetry is broken like, e.g., in α-Fe_2O_3, or $MnCO_3$ [172]. Apart from its relevance in antiferromagnetic crystals the DMI was found to play a crucial role for the formation of magnetic skyrmions [169, 171, 174]. The overall direction of the DMI vector $\boldsymbol{D}$ depends on the symmetry of the system of interest. While magnetic skyrmions were first found in the non-centrosymmetric crystal MnSi [169] we will focus on thin film multilayer systems that make use of the symmetry breaking at the interface [170]. Figure 4.3 a) serves to depict an exemplary heavy metal - magnetic bilayer system with DMI interaction. The high spin-orbit coupling atoms in the heavy metal mediate the DMI between two neighboring magnetic atoms in the ferromagnet, thus inducing the spin canting. The direction of the DMI vector at such a thin-film system points perpendicular to the plane of the spanning triangle of the three involved atoms. It can be quickly calculated by

$$\boldsymbol{D}_{12} = D_{12} \cdot (\boldsymbol{n} \times \boldsymbol{e}_{1,2}), \tag{4.2}$$

where the magnitude and sign of D_{12} are determined by the involved atoms, $\boldsymbol{n}$ is the interface vector pointing from the ferromagnet towards the adjacent material and $\boldsymbol{e}_{12}$ is the normalized connecting vector of the two involved spins. Fig. 4.3 b) depicts the effect of the sign of the DMI which defines the chirality. The magnitude influences the spiral periodicity. However, an exact prediction of the DMI strength requires involved density functional theory and is not always very accurate [162, 175–177]. Nonetheless, due to its torque canting the spins the DMI is a crucial ingredient for the formation of magnetic skyrmions. The 2D magnetization profile of Néel skyrmions is obtained when rotating the presented 1D spin spiral in the plane leading to a ring of up (down) pointing spins with a center pointing down (up). F

[4] Dzyaloshinsky is now commonly cited and referred to as Dzyaloshinskii even though in his contribution relevant to the field he authored as Dzyaloshinsky.

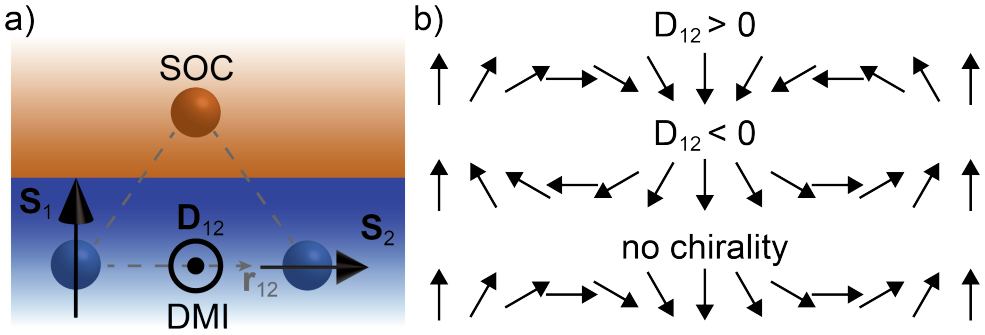

Fig. 4.3. – a) DMI - antisymmetric superexchange b) chirality

4.1.3 Spin Spirals and Skyrmions

Before we go into more details about skyrmions, we will shortly treat the case of large DMI and weak anisotropic energy densities without external magnetic field. Such a scenario is expected to result in a continuous spin rotation where domains and domain walls are hardly separable [178–180]. The magnetic ground state would thus be a spin spiral state with spin spirals as indicated in Fig. 4.3 c). Inhomogeneities in the sample create some sort of randomness such that instead of ordered stripes a labyrinthine arrangement is observed [180–182]. In case of a strong uniaxial anisotropy and lower DMI strength, the continuous rotation is suppressed such that spins not aligning with the easy axis become penalized energetically. The domains would thus form larger up and down regions with constricted areas of rotation constituting the domain walls [182, 183]. Both of these two scenarios allow the formation of bubble-like domains which we will now discuss in more detail.

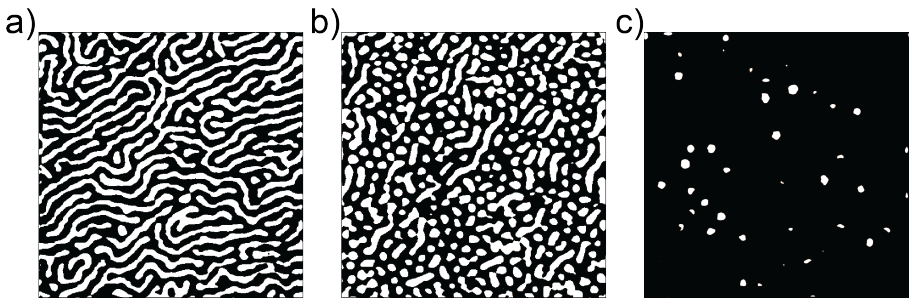

Fig. 4.4. – a) Exemplary depiction of a labyrinthine state, where black and white regions represent positive and negative magnetization component out of the plane. b) By tuning parameters like e.g. external magnetic field or uniaxial anisotropy, that lead to a favored magnetization direction the stripes representing the unfavored domains shrink and turn into smaller bubbles. c) Towards the transition of a uniform magnetization only individual solitons exist before they become extinct completely. The images a) - c) depict 2 µm × 2 µm wide frames. Here, for pedagogical purposes of the images only, the magnetic contrast of CoFe multilayers measured by magnetic force microscopy is abstracted by discretization to up and down states.

Whenever we start from a stripe state with up and downwards directed magnetic moments of neighboring regions (see Fig. 4.4 a)) the transition towards a uniform magnetization can happen via the formation of circular shaped domains. Without loss of generality we can tune a property, e.g. the external magnetic field, such that either one of the two directions is favored. By increasing its strength the favored regions increase while the unfavored shrink in size. Before its annihilation the minority stripes reduce or become chopped to small circles which are often referred to as bubbles and in special cases are called skyrmions (see Fig. 4.4 b) - c)).

While magnetic bubbles represent all sorts of magnetic domains that are somewhat shaped like a bubble, magnetic skyrmions are bubbles that fulfill an additional property. Mathematically, skyrmions are defined as topologically protected field configurations, which in our case means they exhibit a topological charge due to the winding of spins along the spin chain (see Fig. 4.3 b)). Hence, skyrmions represent the category of bubbles that include topological protection. For such textures it is thus not possible to "unwind" the spins by smooth or continuous rotation. Physically, there is an energy barrier that has to be overcome as by, e.g., rotating all spins continuously upwards at least one pair of spins will suffer from an increased exchange energy penalty which leads to the protection. If the chirality within a spin chain is not fixed (rotating in one direction in the first half of the chain and rotating in the other direction for the second half) all spins can be rotated smoothly without having to pass any energy barrier or to break any topological protection[5]. We will from now on concentrate on the topologically protected version of bubbles only.

When comparing literature [13, 164, 169, 178, 179, 185–191], it becomes evident that the term magnetic "skyrmion" alone is not sufficient to describe the investigated magnetic soliton. While the common denominator is the spherical topology and unit topological charge, different properties like size, domain-wall type, magnetization profile, winding numbers and stabilizing energies can vary significantly with and within the specific systems of interest. A short overview is presented to distinguish the most important skyrmion types.

[5] It may be noteworthy to mention that even without DMI in a system topologically protected bubbles can be created. While no fixed chirality is dictated due to the absence of DMI, a single bubble can have a uniform rotation direction (and thus can be termed as a skyrmion due to the topological protection) whereas a neighboring bubble might have the opposite chirality [184]

4.1.3.1 Bloch- and Néel-Skyrmions

The most relevant and best known differentiation refers to the domain-wall type. Bloch- and Néel-type skyrmions exhibit either a Bloch- or Néel-wall between the uniform background and the antiparallel aligned center of skyrmions. Geometry and symmetry are the important ingredients that define which type is preferred. In the absence of DMI, dipolar effects, and thus geometry, determine the wall character. While Bloch-like walls are preferably established in the bulk of the system, a more Néel-like character is established close to the surface [184, 192]. Note, that domain walls do not have to be purely Bloch or Néel type but can as well comprise both components [193].

Similar to the DMI-less systems, bulk and interface character matter for materials exhibiting a non-zero DMI. The first discovered magnetic skyrmions were found in bulk crystals [169, 194, 195] which exhibit an inversion symmetry breaking within their cubic crystal structure. The spin-orbit coupling together with the non-centrosymmetric cubic systems gives rise to the Dresselhaus effect [196] [6] and thus DMI resulting from Dresselhaus spin-orbit coupling [179]. The observed skyrmions exhibit Bloch walls and the DMI is often referred to as bulk-DMI.

On the other hand, when spin orbit coupling and inversion symmetry are present in uniaxial symmetry systems the Bychkov-Rashba effect [197, 198] (often simply refered to as Rashba effect) [7] comes into play. The most prominent example are bi- or multilayer systems where the symmetry is broken at the interface(s). DMI arising from Rashba spin-orbit coupling [179] is thus often referred to as interface-DMI (iDMI) and induces the formation of Néel-skyrmions.

4.1.3.2 Dipolar- and DMI-stabilized Skyrmions

For the distinction of Bloch and Néel skyrmions we already separated DMI-less and DMI-comprising systems. The underlying reason is that two different mechanisms can stabilize the magnetic solitons with unit topological charge. Skyrmions can either be stabilized by dipolar energies (long range demagnetization) or by DMI [185, 191]. Even though the energies at play that give rise to the energy minimum are very distinct, the shape and topological charge are identical.

In literature a distinction is - sometimes - made by referring to skyrmion bubbles as dipolar stabilized solitons, whereas the term skyrmion solely is maintained for DMI stabilized magnetic skyrmions. However, until now, terminology in the field is not very uniform which thus requires caution when comparing "skyrmions" with "skyrmions".

---

[6] The Dresselhaus effect consists in lifting the degeneracy of energy bands with respect to their spin. The band splitting can be described with help of an effective magnetic field whose symmetry favors Bloch-walls.

[7] Similar to the Dresselhaus effect, the Rashba effect lifts the degeneracy of energy bands with respect their spin. The symmetry of the emerging effective magnetic field favors Néel walls. The Bachkov-Rashba effect should not be confused with the Rashba-Edelstein effect which converts a charge current into a spin accumulation.

While DMI-less materials fully rely on dipolar effects, the presence of DMI does not exclude the formation of dipolar-stabilized skyrmions in the system. It is even expected to be able to reach a bi-stable phase, where both types of skyrmion can coexist [191, 199]. Nonetheless, DMI stabilized skyrmions are always much smaller (only few nm) [170, 191] than dipolar stabilized skyrmions. A general misconception that we want to rule out is that it was long thought that dipolar fields cannot stabilize solitons below 100 nm such that the size was used to distinguish between skyrmion bubbles and "real" DMI-skyrmions [161, 199, 200]. It was shown recently, that dipolar fields can indeed induce compact bubbles at least down to roughly 20 nm [191], such that future distinction of the stabilization mechanism has to be performed more carefully. According to Ref. [191] all until now observed room-temperature skyrmions in multilayer thin film systems should be categorized as dipolar-skyrmions rather than DMI-skyrmions due to their findings. Also, it was first thought that the core of skyrmion bubbles is an extended region whereas only DMI-skyrmions are compact, i.e. the radial profile shows a continuous rotation throughout the skyrmion without any uniform magnetization in the core [199]. These inconsistencies in literature show the novelty of the emerging field of skyrmionics where many open questions remain. As a summary, it can be stated that even in DMI systems also long range demagnetization plays a crucial role in defining the available energy minima for skyrmion (bubble) formation and the corresponding radii [185, 191]. Unfortunately, the non-analytical nature of these dipolar effects makes accurate estimations of skyrmion sizes and profiles a bit more cumbersome especially when external magnetic fields are involved [191, 201].

Despite the complications of differentiation of which energies stabilize the skyrmion it is easy to distinguish between the metastability of magnetic solitons and an actual ground state of the magnetic system. We already discussed how skyrmions or bubbles can be created coming from a stripe domain structure by increasing external magnetic fields. It is thus evident, that in the most general case the field history is relevant, which indicates the metastability of the obtained state. However, metastable bubbles do not form when initiating at a homogeneously magnetized state and going to remanence. A spontaneous creation of magnetic solitons out of a uniform background thus reveals a true energy minimum of, e.g., a dense arrangement of skyrmions as a magnetic ground state.

4.2 Magnetic Force Microscopy

In order to analyze the magnetic state and the domains we employed magnetic force microscopy (MFM) [202–205] in order to image the magnetization at the surface of the thin films. The working principle is that of atomic force microscopy (AFM) were a small tip is scanned closely above the surface. Instead of atomic forces as in AFM, MFM makes use of magnetized tips and is thus sensitive to the stray field gradients in the vicinity of the surface. A simplified sketch is shown in Fig. 4.5. By moving the tip at a constant speed either an attracting or repulsive force acts upon the tip depending on the field gradient. Thus, magnetic contrast can be achieved between different domains by measuring the force on the cantilever via optical means. With help of a laser and a frequency modulation of the tip the required sensitivity can be achieved. The cantilever with the tip is excited mechanically close to resonance frequency and the laser is focused on its top surface, such that the reflected light received at a detector oscillates. The frequency, amplitude and phase of the laser modulation can be recorded and mapped to translate the magnetic contrast. In presence of an attracting force, the resonance curve shifts to lower frequencies together with a decrease in phase shift, whereas repulsive forces act contrarily. While this method allows to reduce noise and obtain a high resolution, the tip-sample distance has to be adjusted properly. Too large distances compromise resolution, whereas too small distances convolute the topography onto the MFM signal. A simple method to reduce topographical artifacts is the so called dual pass mode. A first scan is used to map the actual topography and a second scan is used to maintain a constant tip-sample distance according to the contour of the previous topography scan.

The visualization of magnetic domains and skyrmions in this thesis was performed by magnetic force microscopy (MFM) at the Department of Electrical and Computer Engineering at the Technical University of Munich. MFM images were obtained by Valentin Ahrens, Simon Mendisch and myself with a Bruker Dimension Icon AFM. A special desk/case is used to isolate the AFM mechanically and reduce undesired interference with outside mechanical perturbations (see Fig. 4.6 a)). In Fig. 4.6 b) the AFM inside the shielding box is shown. A movable platform allows to control the translation of the sample in a wide range. In order to control the magnetic state and as such the domains in the samples investigated we applied external magnetic fields via a permanent magnet (see Fig. 4.7 a)). A reference spot marked on the magnet allowed for precise de- and installing and fixing of the magnet into the setup with help of the MFM laser spot. Fig. 4.7 b) shows the setup, where the sample can be placed precisely above the permanent magnet. By tuning the height of the linear stage manually, the magnetic field is controlled. A calibration of the stage height and the corresponding magnetic field at the sample surface is shown in Appendix B.

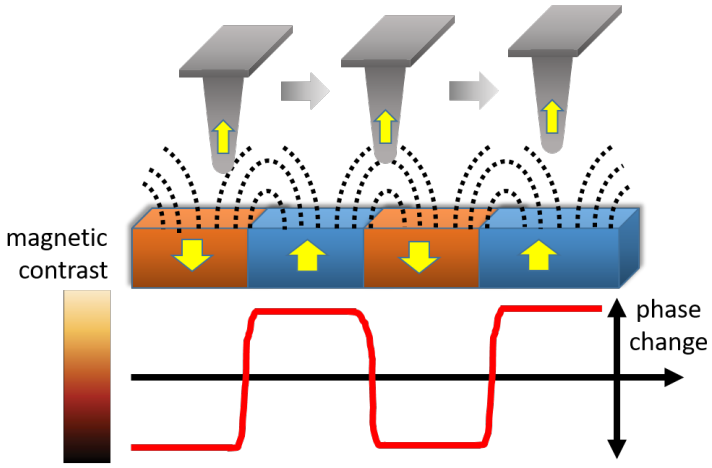

Fig. 4.5. – Sketch of the MFM scanning technique. The cantilever is oscillating up and down (not shown) while being scanned over the sample surface. A magnetic contrast is achieved by detecting the phase change and/or the frequency shift due to the modulation by attracting and repulsive forces [205].

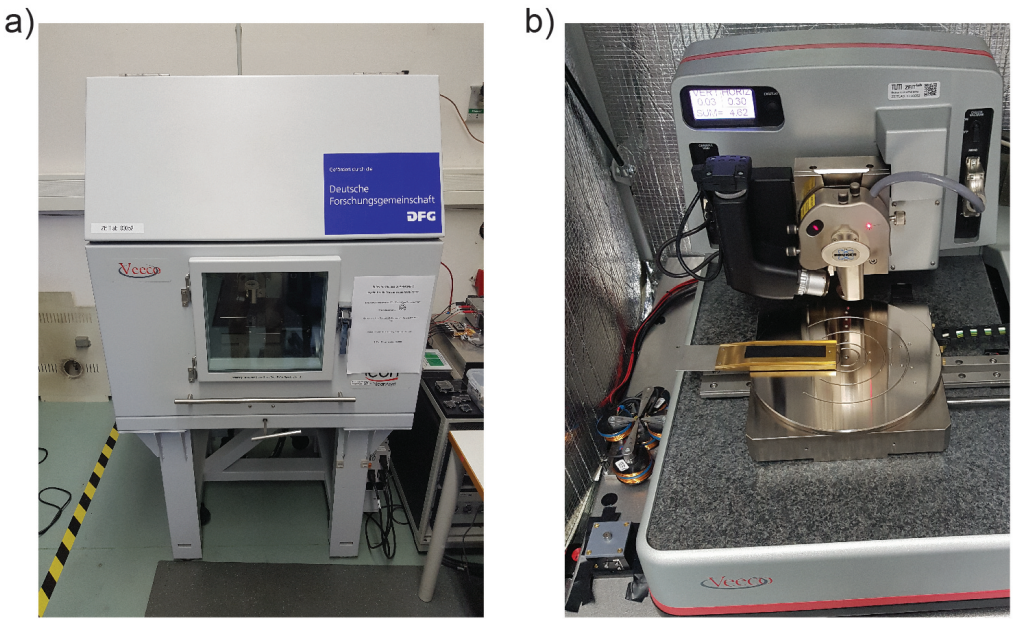

Fig. 4.6. – a) Isolation box to shield mechanical perturbations during the measurements. b) Bruker Dimension Icon AFM with translation plate and sample holder directed to the left.

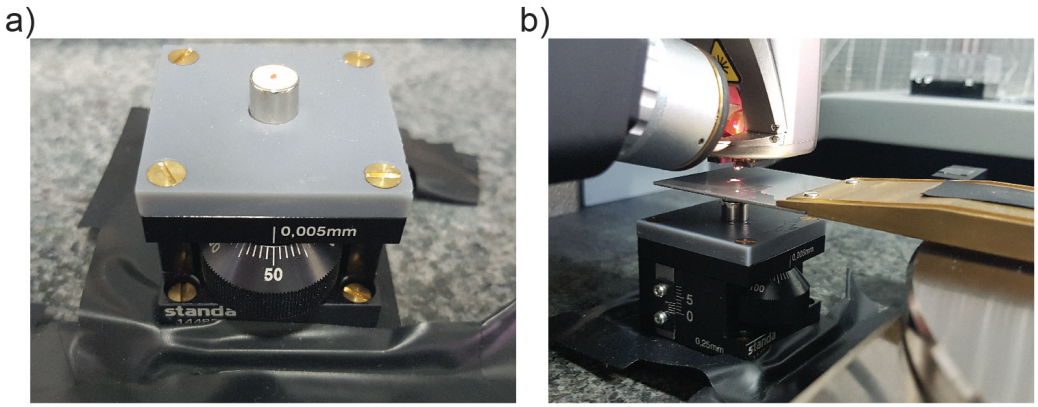

Fig. 4.7. – a) Permanent magnet fixed on a linear stage. The height is controlled manually to change the magnet-sample distance to set the desired magnetic fields. A small mark at the center of the magnet is used for precise (re-) installation with help of the MFM laser spot. b) Side view of the setup. The sample can be placed directly above the magnet stage. The calibration of the magnetic field at the sample surface is presented in Fig. B.1.

4.3 Magnetometry

Apart from spatial dependent measurements to analyze the magnetic texture within our thin films, two integral methods were employed to study the magnetization response vs. external applied field. On the one hand a superconducting quantum interference device (SQUID) [206, 207] magnetometer was used to measure the net magnetization of the sample along the applied field direction. The basic working principle of the SQUID magnetometer is based on two parallel Josephson junctions in a superconducting ring (SQUID loop). A DC current is applied which creates a voltage that depends not only on the applied current but as well on the magnetic flux through the ring. By moving the sample through a second order gradiometer that is coupled to the SQUID loop the magnetic moment is detected. With the SQUID magnetometer, the saturation moment and hysteresis is quantified.

Another method applied for the qualitative comparison of hysteresis loops makes use of the anomalous Hall effect [208–210]. The Hall-voltage in a ferromagnetic thin film strongly depends on the magnetization direction. By scanning the external magnetic field applied in OOP direction, the magnetization follows the magnetic hysteresis behavior and so does the Hall-voltage.

Skyrmion Multilayers

5

Since their discovery in MnSi [169] magnetic skyrmions have been experimentally realized in various different materials and systems. Shortly after the first reports on the skyrmion phase in the metallic B20 crystal MnSi [169, 211], skyrmion formation was proven not to be restricted to metals but was confirmed in the doped semiconductor $Fe_{1-x}Co_xSi$ [194]. The observation of skyrmions in the multiferroic insulator Cu_2OSeO_3 [195] further complemented these findings in bulk systems. Many further bulk crystals with different symmetries like, e.g. FeGe [212], GaV_3S_8 [213] and Co-Zn-Mn alloys [214, 215] enrich the possibilities to stabilize skyrmion within crystals structures. The common ground for all these materials is a non-centrosymmetric crystal structure which breaks inversion symmetry. The symmetry breaking leads to an additional asymmetric exchange interaction due to spin-orbit coupling known as the Dzyaloshinskii-Moriya interaction [172, 173].

After the theoretical prediction of skyrmions forming a spontaneous ground state [171] and its experimental proof in MnSi [169] it did not take long to make use of the intrinsic symmetry breaking at surfaces in thin film systems in order to stabilize the magnetic solitons [170]. Due to the strong spin-orbit coupling at the interface of Fe monolayers on Ir(111) a nano-scale skyrmion lattice at low temperatures was observed [170]. As a further step compared to such a monolayer system it was shown that by choosing two different materials with opposing DMI signs on each side of a ferromagnet the total DMI strength can be increased [161]. As not only the DMI signs but also the signs of the interface vectors counter each other, the DMI interaction on both interfaces of the ferromagnet adds up. Compared to crystals, these multilayers thus profit from a high tunability of material parameters by the choice of materials and thicknesses [162]. Additionally, such multilayers often host skyrmions over much larger temperature ranges, i.e. from room temperature down to a few Kelvin [216, 217].

In this chapter, the previously studied ferromagnet CoFe will be employed for skyrmion formation within multilayer structures. Compared to the often used Co [161, 164, 218] it involves a reduced interface anisotropy and benefits from the low damping properties elaborated in Chapter 3.

5.1 Fabrication

In order to stabilize skyrmions in ferromagnetic multilayer systems, many possible adjacent materials, like e.g Pt, Ir, Ta, MgO, and Ru have been reported [161, 162, 164, 181]. Strong DMI values of $|D| \approx (1.4 - 2.1)\,\mathrm{mJ/m^2}$ in sputter deposited $(\mathrm{Ir/Co/Pt})_{10}$ [161] and $(\mathrm{Ir/Fe/Co/Pt})_{20}$ [162] multilayers were quantified. Due to the similar nature of the ferromagnetic layer of the latter system with CoFe, the magnetic heterostructures in this thesis will make use of Pt and Ir adjacent to the ferromagnet as sketched in Fig. 5.1. Our samples are thus fabricated as $[\mathrm{Pt}(t_{\mathrm{Pt}})/\mathrm{CoFe}(t_{\mathrm{CoFe}})/\mathrm{Ir}(t_{\mathrm{Ir}})]_N$ trilayers which are repeated N times. All the presented samples consistently include a functional seed layer composed of Ta/Pt/Cu. The use of Ta/Pt is widespread [162, 182, 218–221], were Ta acts as an adhesive layer and the Pt induced (111) texturization helps to increase the strength of interface anisotropy in multilayer systems [221–224]. As not only magnetostatic properties but also the dynamic response of the multilayers is investigated the damping has to be optimized. As shown in Fig. 3.1 the Gilbert damping parameter can be significantly reduced by the insertion of an additional Cu spacer. The Pt seed layer is thus separated from the repeated trilayer by Cu in order to minimize damping effects. Due to the interfacial origin of DMI within these multilayer systems, the trilayers can not be modified by additional spacer materials but only by the thicknesses of the involved metals. A cap layer was used to protect the heterostructure from oxidation and consists of Cu/Ta.

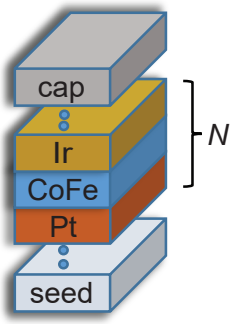

Fig. 5.1. – Simplified sketch of the multilayers investigated where the trilayers are repeated N times.

In the following, samples with varying CoFe, Pt, and Ir thicknesses will be discussed. A table of the exact sputter parameters for each sample including chamber pressure, deposition rates and times, etc. can be found in Appendix A.

5.2 CoFe Thickness Variation

The ferromagnetic layer thickness plays a crucial role for the interplay of DMI strength and exchange energy. In the simplest picture, assuming flat layers and homogeneous magnetization throughout the thickness, the DMI strength at the interface and the exchange stiffness can be regarded as constant. While the energy density stemming from the Heisenberg exchange is independent of thickness, the effective DMI contribution over the entire thickness looses influence with a reduced interface-to-bulk ratio. Even though this model is sufficient to understand why the ferromagnetic layer thickness is relevant for the magnetic ground state, it is strongly oversimplified. Dipolar interactions in multilayer systems can lead to a non-homogeneous magnetization throughout the layers [192, 193, 220]. As

an interface effect the DMI strength depends on the surface quality. In other words, the roughness of the sputter deposited film, intermixing of metals and the surface coverage play an important role for the asymmetric exchange. In the discussions in Chapter 5.3.1 b), the non-trivial thickness dependence of the effective DMI is depicted in Fig. 5.8. Additionally, in the thin film limit, the saturation magnetization and exchange stiffness is no longer independent of thickness [225–227, 227] which further complicates a precise control of fabricated samples.

However, the changes induced by thinner ferromagnetic layers to the magnetic parameters, i.e. effective magnetization, exchange stiffness and DMI all favor a labyrinthine domain formation [180]. While the effective magnetization and exchange stiffness shrink with reduced thickness [225–227, 227], the effective DMI is expected to increase by the increased interface-to-bulk ratio. The transition between a labyrinthine or a spin spiral state (see Fig. 5.2 b)) and the homogeneous ferromagnetic alignment in DMI systems is accompanied by skyrmion formation [162, 180, 189, 228], such that the spin spiral state at remanence is indicative for skyrmion formation in presence of external magnetic fields.

The maximum thickness was long thought to be limited by a condition of effective anisotropy, i.e. $K_{\mathrm{eff}} = K_{\mathrm{u}} - \mu_0 M_{\mathrm{S}}^2/2 > 0$. Here, the easy axis interface anisotropy along the film normal K_{u} is counteracted by the demagnetization, i.e. the shape anisotropy. An uniaxial anisotropy was suggested to be a requirement for DMI systems and the abovementioned condition was obtained omitting higher order spin orbit coupling terms and dipolar contributions [201, 229]. The PMA multilayer systems ($K_{\mathrm{eff}} > 0$) are thus intensively studied and show high tunability of material parameters (e.g. exchange stiffness, saturation magnetization, DMI, anisotropies, interlayer coupling, ...) [161, 162, 164, 192, 193, 218, 230–232]. However, recent theoretical calculations predict an increased phase space and field stability in the $K_{\mathrm{eff}} < 0$ realm [178, 179, 190, 233]. While easy-plane anisotropy has been successfully employed to show skyrmion formation in different systems like polar magnets [234], dipolar stabilized Fe/Gd superlattices [184] and bulk- and interface DMI thin films [217,235], a qualitatively different response of skyrmions in externally applied fields was first discussed during this thesis [236]. Let it be noted that the terms easy-plane and PMA stem from a macro-spin model which does not include domain formation due to, e.g., DMI or magnetostatic energy contributions. Throughout this work the quantification of the anisotropy is performed in saturated states only and the terminology (easy-plane $\equiv K_{\mathrm{eff}} < 0$ and PMA $\equiv K_{\mathrm{eff}} > 0$) is employed consistently as done in related literature [178, 179, 190].

By varying the CoFe thickness t of a $[\mathrm{Pt}(0.65)/\mathrm{CoFe}(t)/\mathrm{Ir}(0.7)]_6$ multilayer (numbers in nm) with nominal $t = (0.9/1.1/1.3)\,\mathrm{nm}$, Fig. 5.2 confirms the formation of a labyrinthine remanent magnetic state for both PMA and easy-plane anisotropy. BBFMR is employed to determine the effective magnetization by a fit

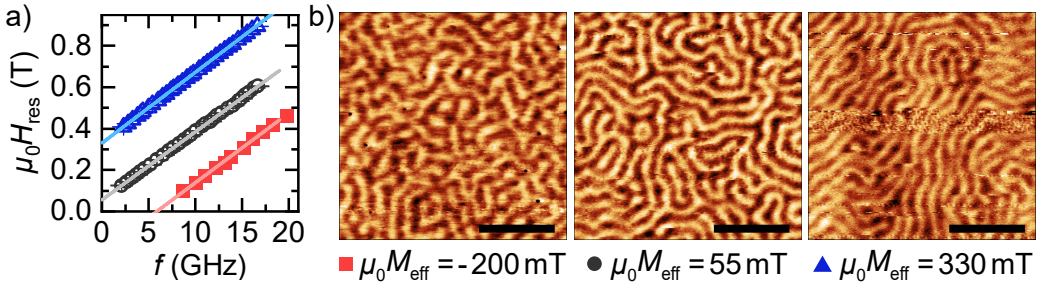

Fig. 5.2. – a) Ferromagnetic resonance of three CoFe multilayers with different FM layer thicknesses of nominally 0.9 nm, 1.1 nm and 1.3 nm. From the fits to Eq. 2.23 we obtain effective magnetizations $\mu_0 M_{eff}$ = -200 mT, 55 mT and 330 mT, respectively. b) MFM images of the three samples in remanence showing labyrinthine magnetic texture. The domain periodicities determined from Fourier transform correspond to wavelengths of 104 nm, 94 nm and 89 nm, respectively. The black scale bars indicate 500 nm.

to Eq. (2.23) (see Fig. 5.2 a)). By combining Eq. (2.22), Eq. (2.8) and Eq. (2.9) we obtain

$$K_{eff} = -\frac{\mu_0 M_S M_{eff}}{2} \tag{5.1}$$

which allows to determine the sign of the effective anisotropy by the sign of the effective magnetization. An exact quantification however requires the determination of M_S which is not done at this point but in chapter 5.3.1 together with a thorough analysis on material parameters of samples analyzed more in depth. The MFM images in Fig. 5.2 b) exhibit a labyrinthine magnetic state indicating the possibility to stabilize skyrmions with externally applied fields for negative and positive M_{eff}.

5.3 Skyrmion Formation with Easy-Plane Anisotropy

The prediction of skyrmion formation in multilayers with $K_{eff} < 0$ include promising material properties like e.g. an increased field range and field stability for the magnetic solitons [178, 179, 190, 233]. Hence, the magnetic texture of an easy-plane anisotropy sample for varying externally applied magnetic fields is investigated in Fig. 5.3. The multilayer consists of nominally $[Pt(0.6)/CoFe(1.145)/Ir(0.7)]_6$ and will be further characterized in chapter 5.3.1. The presented MFM images originate from a collaboration with the Department of Electrical and Computer Engineering from the Technical University of Munich. The images in Fig. 5.3 were recorded by Valentin Ahrens, whereas the field-calibration was performed by Simon Mendisch. A manuscript based on the results reported in this Chapter was submitted to PRL [236].

In Fig. 5.3, at high external magnetic fields (panel a)) no contrast is observed as the magnetic moments are fully aligned with the external field. When the field is reduced below the saturation point (panel b) several individual dots start to

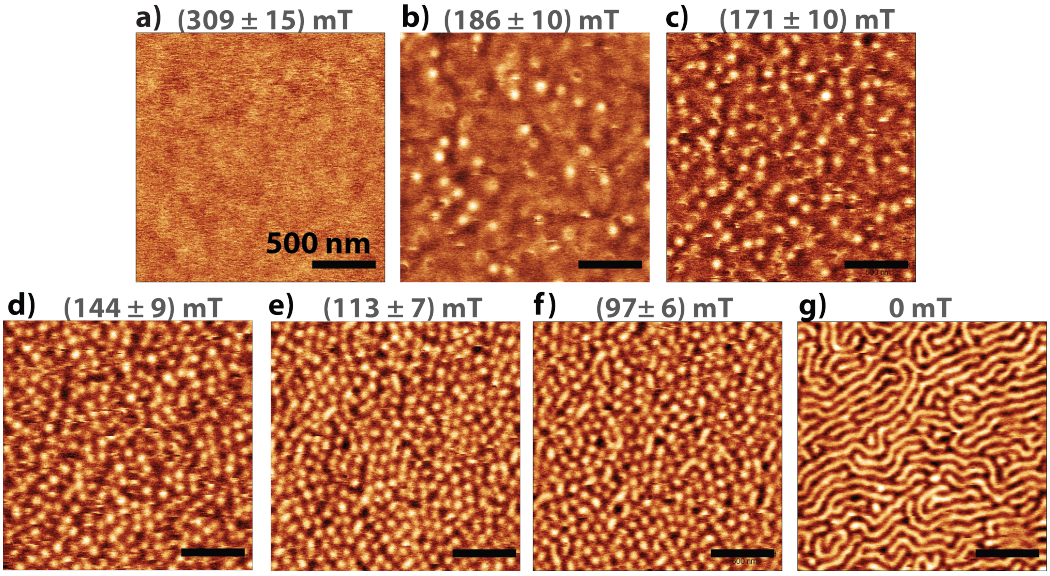

Fig. 5.3. – MFM images recorded with different applied magnetic fields in OOP direction. At high fields a), the sample is magnetically saturated returning no contrast. When reducing the applied field isolated skyrmions start to nucleate as seen in b) and c). By a further field reduction (see d)-f)) a dense unordered arrangement of skyrmions is observed. The remanence state shown in g) is governed by a labyrinthine state, where individual skyrmions maintain stabilized. The images were recorded by Valentin Ahrens.

emerge which are identified as skyrmions. The number of skyrmions increases with shrinking fields (panel c) and d)) until a dense unordered arrangement is stabilized (panel e) and f)). By removing the applied field a labyrinthine remanent state is obtained similar to Fig. 5.2 b), and a small number of individual skyrmions is maintained (panel g)). The observed transition between a fully aligned state towards a spin spiral or labyrinthine magnetic ground state compares well with other reports on skyrmion hosting material systems [161, 162, 164, 217, 237, 238]. The field range within which the skyrmions are detected is twice to ten times as high as in previously investigated systems with $K_{\mathrm{eff}} > 0$ [161, 162, 164, 165]. As the skyrmion formation with easy-plane anisotropy within these samples is confirmed in Fig. 5.3 a more in-depth characterization of the multilayer is performed.

5.3.1 Characterization of the sample

In order to qualitatively and quantitatively compare the investigated multilayer with other reported skyrmion hosting thin films the material parameters relevant for the magnetic texture have to be determined. By ferromagnetic resonance the effective magnetization M_{eff} and the Gilbert damping constant α_{G} can be quantified. With help of SQUID magnetometry the saturation magnetization M_{S} is measured which allows to calculate the effective anisotropy energy density K_{eff}. The iDMI strength D_{int} is measured by Brillouin light scattering on reference samples.

5.3.1.1 Magnetic Resonance

Analogously to the samples in Fig. 5.2 a), the broadband FMR is determined. From OOP and IP FMR measurements and the corresponding Kittel-fit (Eq. (2.23) and Eq. (2.21)) to the data the effective magnetization is quantified as shown in Fig. 5.4 a), revealing the easy-plane anisotropy. While the OOP resonance is well above the noise floor and thus reliably extracted, the IP measurement suffers from additional two-magnon scattering. The reduced amplitude has a low signal to noise ratio which only allows the extraction of the resonance field and frequency manually. The large error-bar reflects the uncertainty yet the easy-plane character is still evident within error. Also within the uncertainty $\mu_0 M_{\mathrm{eff}}$ in both geometries are close together and the small discrepancy could be indicative of a small fourth order anisotropy term [224, 239]. The total perpendicular anisotropy would then be defined by the sum of second and fourth order terms which is obtained in the OOP geometry only [224]. Thus, we will rely on $\mu_0 M_{\mathrm{eff}} \approx 200\,\mathrm{mT}$ for this sample.

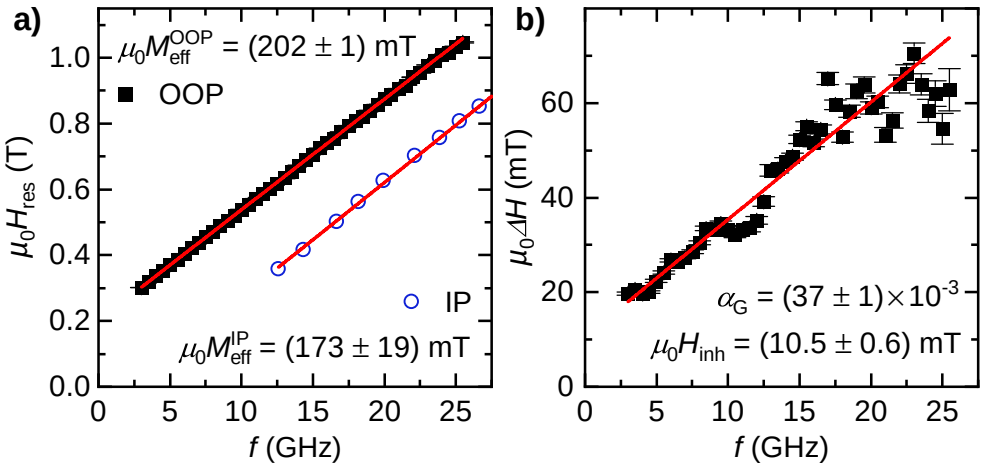

Fig. 5.4. – a) Ferromagnetic resonance for a broad range of frequencies with external magnetic fields aligned in OOP and IP direction. The respective fits to the OOP Kittel Eq. (2.23) and IP Kittel Eq. (2.21) return positive effective magnetization M_S, further affirming the easy-plane anisotropy property. In b), the OOP linewidth shows Gilbert-like damping character and is used to quantify the damping parameter α_G.

The frequency dependent linewidth of the resonance in OOP geometry allows to quantify the Gilbert damping parameter and the inhomogeneous linewidth as discussed in Chapter 2. The inhomogeneous linewidth broadening shows that the sample/interface quality is rather poor compared to the single ferromagnet layers investigated in Chapter 3. However, its has to be considered that a much higher number of much thinner layers is deposited for the skyrmion multilayers. The increased Gilbert-damping compared to the optimized single ferromagnets aligns with the expectation of increased spin pumping contributions due to the adjacent Pt and Ir acting as spin sinks [106, 107, 109, 110, 123, 126, 240]. The interface induced damping contribution scales with $1/t$ and thus penalizes magnetodynamic motion in thin ferromagnetic layers.

In order to reduce the damping it is thus favorable to increase the thickness. The possibility of pushing into the $K_{\mathrm{eff}} < 0$ regime allows thicker ferromagnets compared to PMA samples and facilitates magnetodynamic investigations in skyrmion multilayer systems. Compared to previous skyrmion hosting multilayer materials with PMA like the commonly employed Co which has an $\alpha_{\mathrm{G}} \approx 0.3$ [241] for $t < 1\,\mathrm{nm}$ sandwiched between Pt, Pt/CoFeB/MgO ($\alpha_{\mathrm{G}} = 0.5$ [102]) or Ir/Fe/-Co/Pt ($\alpha_{\mathrm{G}} = 0.1$ [242]) the here extracted $\alpha_{\mathrm{G}} \approx 0.037$ is an improvement of almost an order of magnitude. For the system with Ir/Fe/Co/Pt a recent study where the effective anisotropy was reduced from PMA [242] to $K_{\mathrm{eff}} \approx 0$ [243] estimated a Gilbert damping parameter of $\alpha_{\mathrm{G}} = 0.05$ further supporting the benefit for reduced K_{eff}.

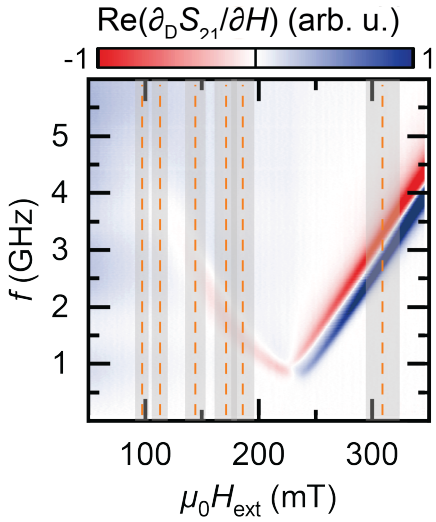

Fig. 5.5. – The low-frequency 2D scan of the OOP magnetic resonance shows a clear FMR signal for $\mu_0 H_{\mathrm{ext}} \gtrapprox 240\,\mathrm{mT}$. By lowering the magnetic field an additional faint resonance with increasing frequency is visible. This field coincides with the nucleation field in Fig. 5.6 below which skyrmions start to evolve. The resonance is attributed to the magnetization dynamics of the non-skyrmion magnetic moments.

The low damping allows the detection of a magnetic resonance in the multilayer below the saturation field as shown in Fig. 5.5. For $\mu_0 H_{\mathrm{ext}} > \mu_0 H_{\mathrm{s}} = 240\,\mathrm{mT}$, i.e. above the saturation field, a clear signal stemming from the FMR is visible. On the other side, for $\mu_0 H_{\mathrm{ext}} < \mu_0 H_{\mathrm{s}}$, a fainting resonance is still observed, which rises in frequency with decreasing $\mu_0 H_{\mathrm{ext}}$. In this region, the MFM images show the formation of non-uniform magnetic texture. Additionally, the effective easy-plane anisotropy is expected to cause a rotation of the magnetization towards the film plane which further reduces the OOP magnetization. A similar resonance behavior is reported in Ref. [243], where the dynamic precession is attributed to the magnetic moments in the quasi-uniform background instead of the spin dynamics within the skyrmions itself. The vanishing signal as a dense skyrmion arrangement is reached agrees well with the given explanation. Similar resonances have been observed by Montoya *et al.* [186] in DMI-less Fe/Gd superlattices. Several resonances attributed

to skyrmions were recorded, yet the in Ref. [186] reported phase transitions differ qualitatively. The Fe/Gd multilayers exhibit a direct development of coexisting stripes and skyrmions coming from a field polarized state instead of the transition depicted in Fig. 5.3. The detection of spin dynamics in the sub-saturation field range within iDMI skyrmion multilayers enables further magnetodynamic studies and the optimization for reduced damping shows to be crucial.

5.3.1.2 Magnetometry and Anisotropy Analysis

The saturation magnetization M_S is a crucial magnetic parameter for many further derived quantities like the effective anisotropy and the DMI strength. SQUID magnetometry is performed to extract the important material constant and the recorded IP and OOP hysteresis loops from the cleaved sample are depicted in Fig. 5.6. The loops are normalized by the magnetic moment in saturation of the respective curve. The OOP magnetization exhibits a characteristic shape often reported in multilayers with domain or rather labyrinthine state formation at low magnetic fields [162, 164, 187, 192, 217, 221, 237, 244]. As the domain formation leads to a shearing of the hysteresis loop even for $K_{\text{eff}} > 0$ [162,164,187,192,221,237,244] a comparison to the IP geometry is required. Other than in the PMA multilayer reported in Ref. [162] where the IP hysteresis shows a clear hard axis behavior the remanent magnetization in the presented $K_{\text{eff}} < 0$ case is higher than in the OOP case for all fields. A easy-plane switching loop with a coercivity of roughly 4 mT is observed. The reduction of magnetic moment aligned with the external magnetic field can be attributed to the domain formation due to the influence of iDMI [180]. It has to be noted that similar behaviors were reported in DMI-less "thick" 25 nm - 500 nm Co crystals [245] and 200 nm epitaxial Ni [246] due to dipolar effects [247]. However, the in these systems relevant crystalline anisotropies and strain effects are not applicable to the poly-crystalline sputter deposited multilayers.

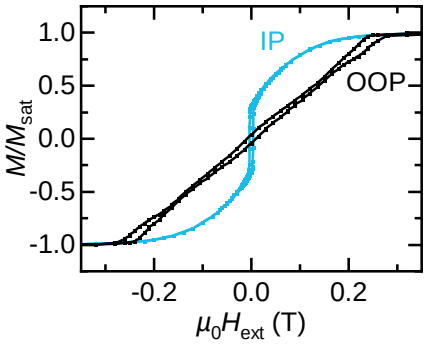

Fig. 5.6. – SQUID magnetometry in IP and OOP direction. The OOP loop shows typical hysteresis pockets close to the saturation field. The IP behavior shows an easy-plane switching behavior with a coercivity of roughly 4 mT. The reduction of magnetic moment before the switching is attributed to domain formation.

M_S is extracted from an IP loop (not shown) measured with the uncleaved sample of known nominal magnetic volume ($10\,\text{mm} \times 6\,\text{mm} \times 1.145\,\text{nm} = 68.7 \times 10^3\,\mu\text{m}^3$). The magnetic moment in saturation at 400 mT is measured to be $0.48\,\mu\text{Am}^2$ and thus, $M_S = 1164\,\text{kA/m}$. The area enclosed by the IP and the OOP loop quantifies the inherent effective anisotropy [223] to a value of

$$K_{\text{eff}} = -37.4\,\text{kJ/m}^3$$

. The effective anisotropy in the saturated state, however, can be calculated considering M_{eff} and Eq. (5.1), where $K_{\mathrm{eff}} = -118\,\mathrm{kJ/m^3}$. Despite the reduction of $|K_{\mathrm{eff}}|$ due to domain formation the easy-plane anisotropy energy density character is evident. Possible systematic experimental errors would lead to an underestimation of the easy-plane character. For the magnetic volume no magnetic dead layer was assumed, which itself would reduce the magnetic volume and thus increase M_{S} and subsequently $|K_{\mathrm{eff}}|$ as well. In the same fashion, M_{eff} can only be underestimated by finite misalignment of the OOP direction and thus, the presented values of $|K_{\mathrm{eff}}|$ can be regarded as a lower limit. A comparison with a selection

Tab. 5.1. – Selection of skyrmion hosting iDMI multilayer systems where K_{eff} was either measured directly or extractable from given magnetic material parameters.

Heterostructure	$K_{\mathrm{eff}}(\mathrm{kJ/m^3})$	Reference
Ir/Co/Pt	170	[161]
Pt/Co/Ta	~ 180	[164]
Pt/Co/Ir	$400 - 550$	[165]
Co/Pd	~ 120	[193]
Ir/Fe/Co/Pt	≤ 250	[162]
Ir/Fe/Co/Pt	$50 - 290$	[192]
Pt/Co/MgO	50	[192]
Pt/CoFe/Ir	$< -37\,(-118)$	this work [74]

of iDMI multilayer systems where skyrmions are reported and K_{eff} is extractable is done with help of Tab. 5.1. It becomes evident that the value for K_{eff} in the herein analyzed system is significant although of opposite sign. In addition to the anisotropy, a further important magnetic parameter in the heterostructure is the DMI strength discussed in the following.

5.3.1.3 Brillouin Light Scattering

Brillouin light scattering is employed to quantify the iDMI on reference samples made of single trilayers [70, 165]. The measurements have been performed in a collaboration with the Fachbereich Physik and Landesforschungszentrum OPTIMAS, Technische Universität Kaiserslautern. Tobias Böttcher provided the BLS data, whereas Manuel Müller performed SQUID magnetometry on the reference samples to quantify the respective M_{S} necessary for the calculation of the effective DMI strength D. Two sample series of single trilayer Pt(t_{Pt})/CoFe(1.145)/Ir(0.7) and Pt(0.6)/CoFe(t_{CoFe})/Ir(0.7) were fabricated for this purpose.

In the presence of asymmetric exchange, the spin wave dispersion of a ferromagnet experiences a non-reciprocal frequency shift:

$$f_{\mathrm{DMI}} = \frac{\gamma}{\pi M_{\mathrm{S}}} Dk. \tag{5.2}$$

Here, D represents the effective DMI strength. By measuring counter propagating spin waves, a frequency difference

$$\Delta f = f(k) - f(-k) = 2 \cdot \frac{\gamma}{\pi M_S} D\,|k| \tag{5.3}$$

is observed as depicted in Fig. 5.7. The Stokes and anti-Stokes BLS peaks are

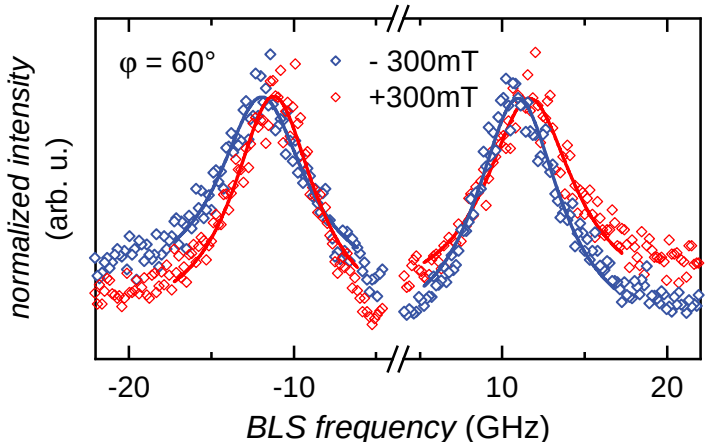

Fig. 5.7. – Normalized Stokes- and anti-Stokes peaks measured by BLS on a single trilayer reference sample with $t_{CoFe} = 1.145$ at an incident angle $\varphi = 60°$. The iDMI induces a frequency shift between the $+k$ and $-k$ magnons, which can be selected by the applied magnetic field direction. The data was recorded by Tobias Böttcher.

recorded for both positive and negative externally applied magnetic fields of $|\mu_0 H_{ext}| = 300\,\mathrm{mT}$. The field inversion changes the magnetization direction and thus results in the same frequency shift $\Delta f = f(M,k) - f(-M,k)$ as for the k inversion. With the angle of incident light relative to the film normal the magnitude of the k vector can be adjusted. In Fig. 5.7 $\varphi = 60°$ is used corresponding to $|k| = 23.8\,\mathrm{rad/\mu m}$. As the frequency shift is directly proportional to the wave vector it can be tuned by the angle φ. For the determination of DMI strength the angle is varied between $45° \leq \varphi \leq 70°$ corresponding to wave vectors $13.7\,\mathrm{rad/\mu m} \leq k \leq 25.8\,\mathrm{rad/\mu m}$. By carrying out a linear fit to Δf vs k the prefactor of Eq. 5.3 is determined. The saturation magnetization extracted from SQUID magnetometry $M_S = 1112\,\mathrm{kA/m}$ and the gyromagnetic ratio determined with BBFMR $\gamma = 176 \times 10^9\,\mathrm{rad/Ts}$ are used to calculate $D = (0.30 \pm 0.03)\,\mathrm{mJ/m^2}$. The effective DMI D is used to quantify the DMI at the interface with [70]:

$$D_{int} = t_{CoFe} \frac{\sqrt{3}}{a} D. \tag{5.4}$$

Here, an average lattice constant $a = 0.32\,\mathrm{nm}$ for CoFe from Ref. [93] is assumed. With the nominal thickness $t_{CoFe} = 1.145\,\mathrm{nm}$ to match the thickness of the multilayer sample investigated in Fig. 5.3, the iDMI value $D_{int} = (1.94 \pm 0.2)\,\mathrm{pJ/m^2}$ compares very well with values reported in Ref. [162], where Ir/Fe/Co/Pt multilayers were analyzed.

The effective DMI determined from BLS and SQUID magnetometry of the different samples with varying thicknesses t_{Pt} and t_{CoFe} are plotted in Fig. 5.8. In the first sample series with varying Pt thickness shown in Fig. 5.8 a), an almost linear increase of D is observed. While for bulk Pt no thickness dependence is expected as the DMI in these multilayers is an interface effect, a full Pt coverage of the surface can not be expected in the sub nm regime [248]. The increasing D thus aligns well with an increased surface coverage due to nominally thicker Pt layers. For the

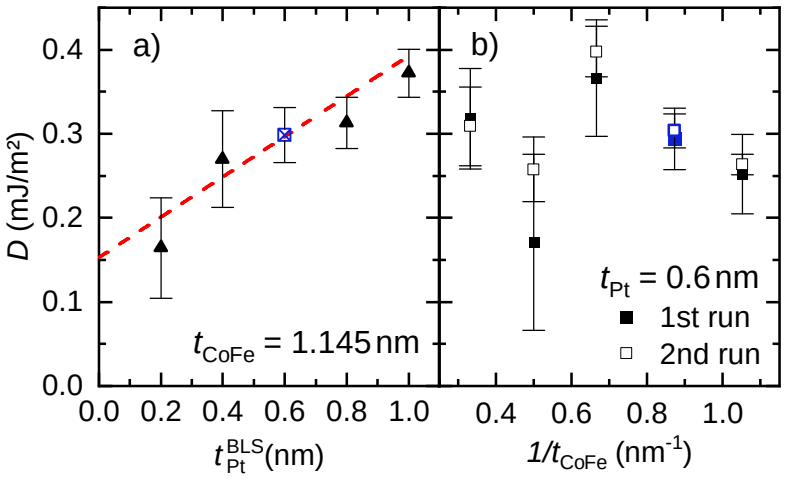

Fig. 5.8. – The effective DMI strength of samples with varying Pt and CoFe thicknesses was determined with BLS measurements and SQUID magnetometry. The Pt thickness variation in a) shows increasing DMI strength for increasing thicknesses, whereas no clear trend for the CoFe thickness variation in b) is visible. The BLS measurements were performed by Tobias Böttcher and the determination of M_S via SQUID magnetometry was performed by Manuel Müller.

second series with varying CoFe layers shown in Fig. 5.8 b) a more complicated behavior is observed. Any purely interfacial effect is expected to scale linearly with $1/t$, however, no clear trend is visible in the range of $0.95\,\text{nm} \leq t_{CoFe} \leq 3\,\text{nm}$. This may be attributed to the involved thickness dependence of material parameters in the ultra-thin regime. Heisenberg exchange can change strongly with the FM thickness [70] as does M_S within these samples ($1041\,\text{kA/m} \leq M_S \leq 1578\,\text{kA/m}$). Surface roughness and coverage are non-trivial to determine within these multilayers further complicating the thickness dependence. Experimental-wise the observed dependence shows to be robust by two separate measurement runs of the samples. The data shows that the largest volume-averaged DMI strength is obtained for $t_{CoFe} = 1.5\,\text{nm}$ implying that ultra-thin samples with $t_{CoFe} < 1\,\text{nm}$ are not required to maximize DMI in this approach. The drawn conclusion has a beneficial impact on the previously discussed tuning of the FM layer towards higher thicknesses. While K_{eff} can be reduced with increased t_{CoFe} DMI strength is not proportionally lost, which would impair skyrmion formation.

With help of BBFMR, SQUID magnetometry and BLS measurements several material parameters are quantified for the presented easy-plane anisotropy skyrmion host. A short overview of the extracted values is presented in Tab. 5.2.

Tab. 5.2. – Overview of the extracted material parameters from various measurement techniques.

$\mu_0 M_{\mathrm{eff}}$ (mT)	$\alpha_{\mathrm{G}}(10^{-3})$	$\gamma(\frac{rad}{Ts})$	μM_{S} (T)	$D_{\mathrm{int}}(\mathrm{mJ/m^2})$	$K_{\mathrm{eff}}(\mathrm{kJ/m^3})$
202 ± 1	37 ± 1	176	1.46	1.94 ± 0.2	$< 37\,(-118)$

5.3.2 Micromagnetic Simulation

With the characterization of both static and dynamic magnetic response the extracted parameters are used to reproduce the observed behavior with micromagnetic simulations [16]. The simulations were performed by Lukas Körber in a cooperation with the Fakultät Physik of the Technical University Dresden and the Helmholtz-Zentrum Dresden-Rossendorf e.V, Institute of Ion Beam Physics and Material Research. The simulated system leans on an effective single film model with a geometry of $512 \times 512 \times 1$ cells with periodic boundary conditions. Here, cell sizes of $3\,\mathrm{nm} \times 3\,\mathrm{nm} \times 12.6\,\mathrm{nm}$ were used. A comparison of the lateral length of the cells to the exchange length

$$l_{\mathrm{ex}} = \sqrt{\frac{2A}{\mu_0 M_{\mathrm{S}}^2}}, \tag{5.5}$$

is important to actively avoid an artificial increase of the effect of the exchange stiffness. From Ref. [249] $A = 26\,\mathrm{pJ/m}$ for CoFe is used and $M_{\mathrm{S}} = 1212\,\mathrm{kA/m}$ approximates the saturation magnetization from SQUID magnetometry measurements. An exchange length of $l_{\mathrm{ex}} \approx 5.4\,\mathrm{nm}$ is obtained which is well above the lateral cell size. The cell thickness approximates the thickness of the multilayer stack. The good agreement of the simulated data with experiments (see Fig. 5.9) shows that the observed behavior can be qualitatively explained well assuming a homogeneous magnetization throughout the layers, where demagnetization effects along the layer-stack play a negligible role [192, 193, 220]. The remaining material parameters for the simulations are the uniaxial anisotropy $K_{\mathrm{u}} = 801.8\,\mathrm{kJ/m^3}$ (together with M_{S} resulting in $\mu_0 M_{\mathrm{eff}} = 200\,\mathrm{mT}$), the DMI constant $D_{\mathrm{int}} = 1.8\,\mathrm{mJ/m^2}$ and the Landé-factor $g = 2.13$.

In Fig. 5.9 a) the experimental magnetometry is compared to the response of the simulated system. The qualitative agreement of the magnetostatics becomes evident while minor deviations can be attributed to the simplification of the simulation. The observed magnetic texture at finite applied external magnetic fields and remanence is shown as MFM and simulated images in the insets of Fig. 5.9 a). Both, individual skyrmions and the formation of a labyrinthine state containing a small number of skyrmions are well reconstructed.

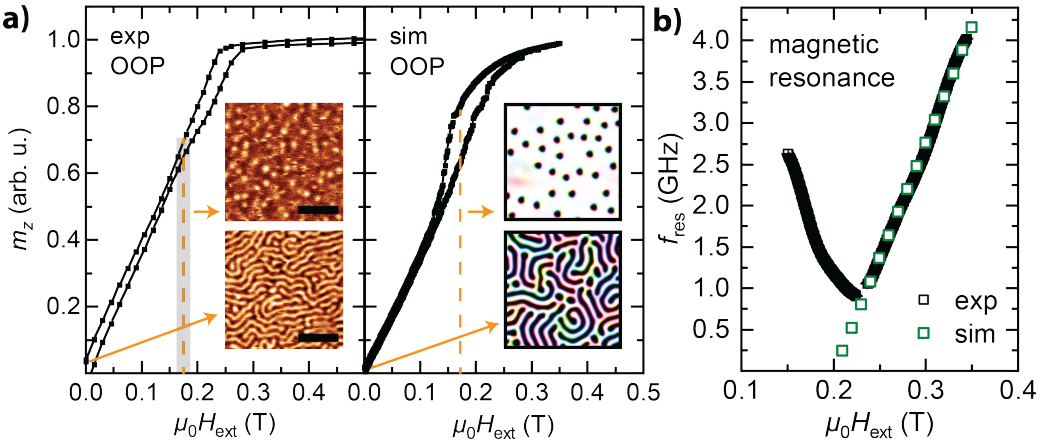

Fig. 5.9. – The material parameteres determined from the above mentioned experiments were used to perform micromagnetic *MuMax* simulations. The static response shown in a) and the ferromagnetic resonance in b) could be qualitatively and quantitatively reproduced, respectively. The simulations exhibit skyrmion formation despite the $K_{\text{eff}} < 0$ parameter space. The simulations were performed by Lukas Körber and the MFM insets were recorded by Valentin Ahrens.

The ferromagnetic resonance shown in Fig. 5.9 b) exhibits a high quantitative agreement of simulation and experiment. For the micromagnetic modeling of the dynamic response, the sample is initialized with a small tilt from the OOP direction and relaxed in a finite static external magnetic field. By a sinc pulse in time of an additional spatially homogeneous field in the plane the magnetization is excited. The Eigenfrequency of the system is extracted and the procedure is repeated for decreasing steps of the static external field. While the resonance in saturation is in very good agreement the dynamic response below saturation could not be extracted from the simulations.

In a summary, micromagnetic simulations of the simple thin film model corroborate the observed static and dynamic response together with skyrmion formation in the effective easy-plane anisotropy realm.

5.3.3 Radius dependence

The sample characterization, i.e. the determination of macroscopic magnetic parameters and the theoretical modeling provide a general understanding of the skyrmion formation in the easy-plane anisotropy system. While the field dependent phase evolution (field polarized alignment → individual skyrmions → dense skyrmion arrangement → labyrinthine spin spiral state) compares well with PMA multilayer systems [161, 162] a more careful analysis reveals qualitative differences. By studying the field dependent skyrmion size a distinctive behavior is obtained, which will be elaborated in the following.

In Fig. 5.10 a) the magnetic texture of the multilayer without any externally applied magnetic field is shown, which depicts the same MFM image as in Fig. 5.3 g). The visibly dense labyrinthine spin spiral state is analyzed regarding its periodicity

in two different ways. On the one hand, a Fourier transform of the image is azimuthally averaged and shown in Fig. 5.10 b). The resulting intensity vs the radial distance in reciprocal space indicates the weight of the spatial periodicities within the MFM image. The peak intensity is found at a "wave vector" which corresponds to an overall stripe periodicity of $\lambda \approx 84\,\mathrm{nm}$. While this method represents an integral approach over the entire MFM image a "local" analysis is shown in Fig. 5.10 c). A line scan through the image which corresponds to the black line in panel a) is selected perpendicular to a high number of stripes. The plotted MFM signal oscillations can be fitted with a sinusoidal function revealing a periodicity of $\lambda \approx 82\,\mathrm{nm}$. The residual of the fit additionally confirms that neither up nor down stripe domains are favored above the other. It can be concluded that both the two dimensional and the one dimensional approach return well matching results. The extracted periodicity of the spin spiral state furthermore allows an estimation of the maximum space for skyrmions in an idealized, dense skyrmion crystal. A single skyrmion with its magnetic moment in the center pointing in down(up) direction is surrounded by magnetic moments pointing in up(down) direction. Thus, an fictitious, idealized skyrmion within a dense stripe environment can have a maximum radius of $\lambda/4 \approx 20\,\mathrm{nm}$.

As the remanent state exhibits individual skyrmions a more detailed analysis is performed as shown in Fig. 5.11. Here, panel a) shows a zoom-in frame of the MFM image also shown in Fig. 5.10 a) in the vicinity of the skyrmion labeled as "A". Two 1D scans cutting through the skyrmion and being almost perpendicular to neighboring stripes and towards each other are highlighted and depicted in Fig. 5.11 b). Sinusoidal fits were used to extract the local periodicity along the scan. While the scan labeled as "1" returns $\lambda_1 = 99\,\mathrm{nm}$ and thus differs from the previously determined periodicity the scan labeled as "2" returns a well matching $\lambda_2 = 83\,\mathrm{nm}$. Additionally, the oscillations within the scans related to the soliton are fitted with a Gaussian function to quantify the radii along the corresponding direction. In the case of scan "1", where the vicinity does not represent the dense domain arrangement the radius $r_1 \approx 30\,\mathrm{nm}$ does not satisfy the relation $\lambda/4 = r$. On the other hand, scan "2" which matches the overall determined periodicity fulfills the estimation with $\lambda_2/4 \approx r_2 \approx 20\,\mathrm{nm}$. The discrepancy of the radii r_1 and r_2 exemplifies the difficulty of quantifying a radius for the skyrmion with a 1D approach, yet it also indicates an importance of neighboring texture. For this reason, the further skyrmion analysis takes into account the 2D data of the solitons. By azimuthally averaging around the center position of the skyrmion, the radial profile is fitted with a Gaussian function. This enables the quantification of a single averaged radius per skyrmion. Nonetheless, a size variation comparing different skyrmions is expected due to the influence of neighboring magnetic texture and inhomogeneity in the sputter deposited multilayers. The 2D analysis approach will thus be elucidated using the example of a dense skyrmion arrangement at finite externally applied field.

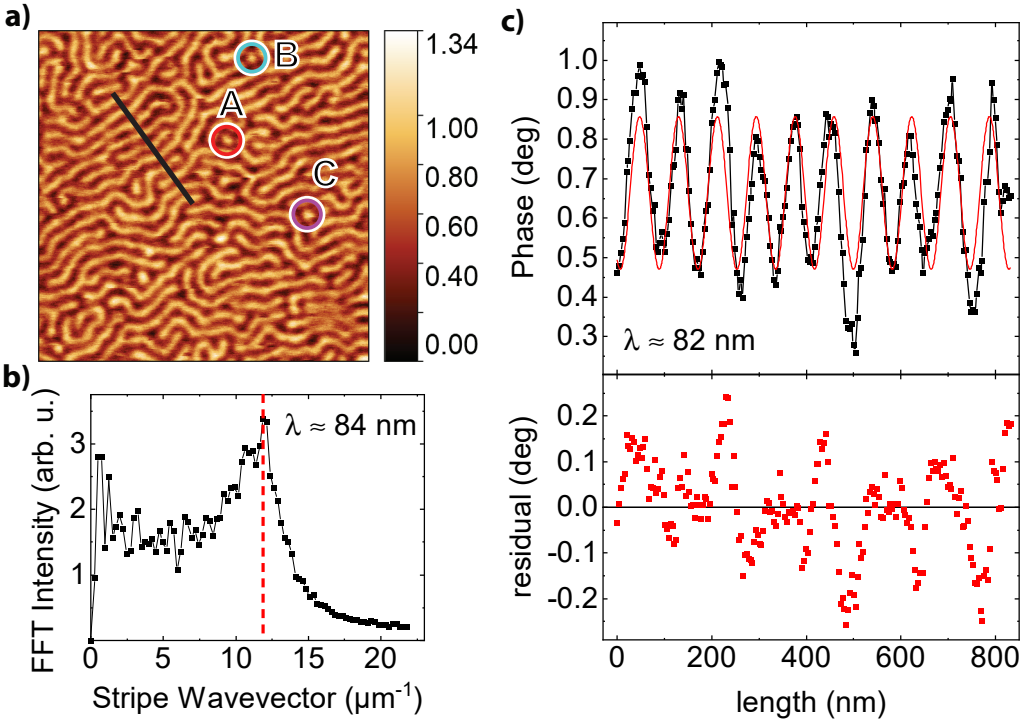

Fig. 5.10. – a) 2 μm × 2 μm MFM image of the remanence state as shown in Fig. 5.3 g). The stripe periodicity is determined via a Fourier transform of the image in b) and a line cut indicated by the black solid line. From the Fourier transform we determine the spacial frequency (or wave vector), with the highest intensity which corresponds to a wavelength of 84 nm. In c) a sinusoidal fit to the line cut returns a well matching periodicity of 82 nm. The residual of the fit shows no clear over/underestimation confirming the equalized up and down domains. The individual skyrmions labeled in a) as A, B, and C are further analyzed in Fig. 5.13 a). The MFM image was recorded by Valentin Ahrens.

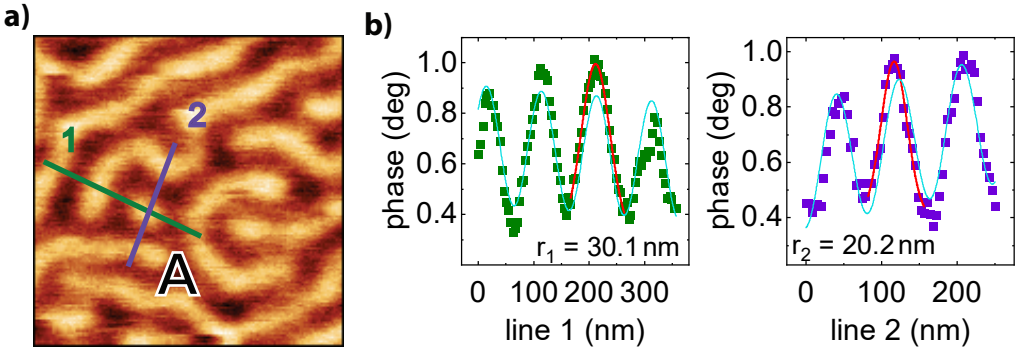

Fig. 5.11. – a) Zoom-in frame of the MFM image shown in Fig. 5.10 a) close to the skyrmion labeled as A. Two line cuts are shown which are further analyzed in b). From the sinusoidal fits to line 1 and line 2 (cyan lines) local periodicities of $\lambda_1 = 99$ nm and $\lambda_2 = 83$ nm were determined. A Gaussian fit to the peak corresponding to the skyrmion signal results in radii along the lines of $r_1 = 30.1$ nm and $r_2 = 20.2$ nm. The MFM image was recorded by Valentin Ahrens.

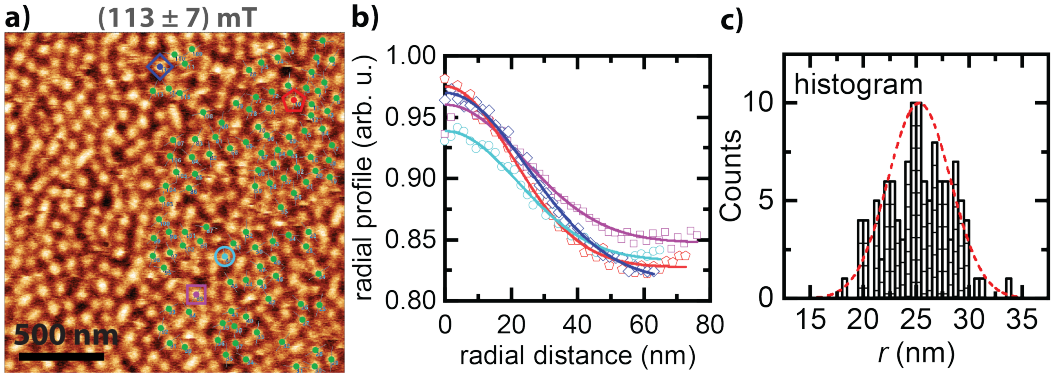

Fig. 5.12. – a) MFM image as in Fig. 5.3 e). A large set of skyrmions was taken indicated by the green dots. The azimuthally averaged radial profile of each skyrmion is analyzed as shown in b). Here, the data points stem from the highlighted skyrmions with the corresponding symbol and color in a). The lines depict Gaussian fits, from which the radius was determined by the half width half maximum. The histogram in c) shows a normal distribution of all extracted radii. The MFM image was recorded by Valentin Ahrens.

In Fig. 5.12 a) the magnetic texture in a magnetic field of $\mu_0 H_{\text{ext}} = (113 \pm 7)$ mT is depicted corresponding to the MFM image in Fig. 5.3 e). The green dots indicate all the selected skyrmions that are further analyzed. Four skyrmions indicated by the blue diamond, red pentagon, cyan circle and purple square are taken to exemplify typical radial profiles in Fig. 5.12 b). As can be seen, the Gaussian fit to the azimuthally averaged skyrmion signal shows a good agreement and allows to extract the radius as the half-width-half-maximum. Fig. 5.12 c) shows the resulting histogram of all the selected skyrmions showing a normal distribution of radii spread between $20\,\text{nm} \leq r \leq 30\,\text{nm}$.

The procedure is performed for all MFM images shown in Fig. 5.3, yet for the remanent state instead of a histogram only the skyrmions labeled as "A", "B" and "C" from Fig. 5.10 a) are evaluated. In Fig. 5.13 a) the radial profiles of the individual solitons in remanence are plotted whereas in Fig. 5.13 b) the arithmetic mean of the radii of the selected skyrmions for each field is shown. The radius error bars in panel b) indicate one standard deviation, while the circles stem from a separate MFM sweep (not shown) with increasing fields. From the graph a constant radius of $r \approx 25\,\text{nm}$ for magnetic fields up to roughly $\mu_0 H_{\text{ext}} \approx 150\,\text{mT}$ becomes immediately apparent, which diverges for higher applied fields. The recorded field dependence strongly controverts the usual skyrmion field evolution, where the solitons significantly shrink in size due to an increased Zeeman energy cost of a skyrmion [161, 162, 165, 218, 250]. Reported skyrmion sizes in iDMI multilayer samples at different applied magnetic fields however are limited to the PMA ($K_{\text{eff}} > 0$) regime which qualitatively separates our system from previous works. The distinct behavior is in accordance with the theoretical work by Banerjee *et al.* [178] who predicted a rather stable skyrmion size for a large field range for easy-plane anisotropy thin films. The additional stabilization mechanism responsible

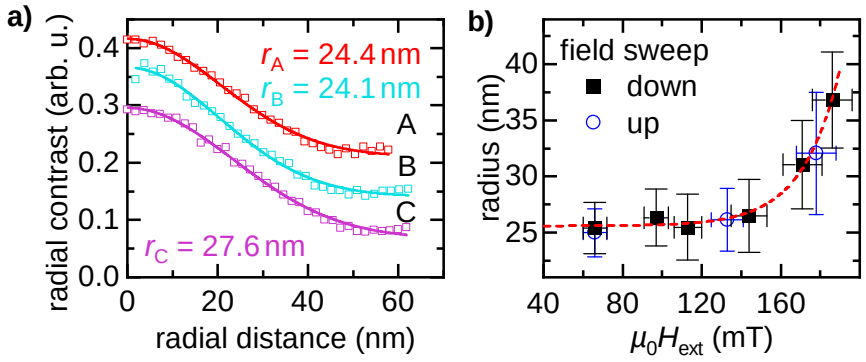

Fig. 5.13. – a) shows the azimuthally averaged radial profiles of the skyrmions labeled as A, B, and C in Fig. 5.10. The Gaussian fits return an average radius of $r = (25.4 \pm 1.6)$ nm. In b) the black squares indicate the average value determined from $28 - 115$ skyrmions from the MFM images shown in Fig. 5.3 b)-f) where the analysis is performed as in Fig. 5.12. The error bars indicate the standard deviation of the radii distribution. The blue circles correspond to the analogous procedure from MFM images taken during a sweep with increasing fields. No hysteretic behavior for the down/up sweep could be resolved.

for the constant skyrmion radius can be explained by the contribution of the easy-plane "compass" anisotropy to the free energy. This addition to the energy landscape stems from higher spin-orbit coupling terms. While the generalization to a continuum model is non-trivial an intuition of its effect can be gained by a discretized model with local moments arranged in a square lattice. In this case the Hamiltonian of the compass anisotropy term can be written as [178, 251, 252]:

$$\mathcal{H}_c = -A_c \sum_i (S_i^y S_{i+\hat{x}}^y + S_i^x S_{i+\hat{y}}^x). \tag{5.6}$$

Here, A_c represents the compass anisotropy which depends on the exchange integral, and $S_i^{x,y}$ represent the local moment's x and y component at lattice site i. $\hat{x}$ and $\hat{y}$ stand for a unit lattice constant in x and y direction. When placing a skyrmion texture in the square lattice smaller radii of the corresponding domain wall would thus decrease the products $S_i^y S_{i+\hat{x}}^y$ and $S_i^x S_{i+\hat{y}}^x$. This leads to an increased total energy. Thus, the compass anisotropy penalizes shrinking skyrmion sizes and counteracts the Zeeman contribution which favors the reduction of non-aligned textures. However, further investigations of the possible effects of compass anisotropy in iDMI multilayers are desirable. The spin-orbit coupling induced anisotropy, amongst other effects like e.g. frustration, can explain the formation of topological spin textures even without DMI in centrosymmetric tetragonal magnets [252, 253]. At the interface of two non-magnetic insulating oxides $LaAlO_3/SrTiO_3$ it was found to play an important part in inducing a magnetization and ferromagnetic exchange [254]. However, the identification of compass anisotropy within a sputter deposited heterostructure in this work may be unprecedented and thus could motivate further systematic experimental and theoretical studies. The micromagnetic simulations used within the collaboration

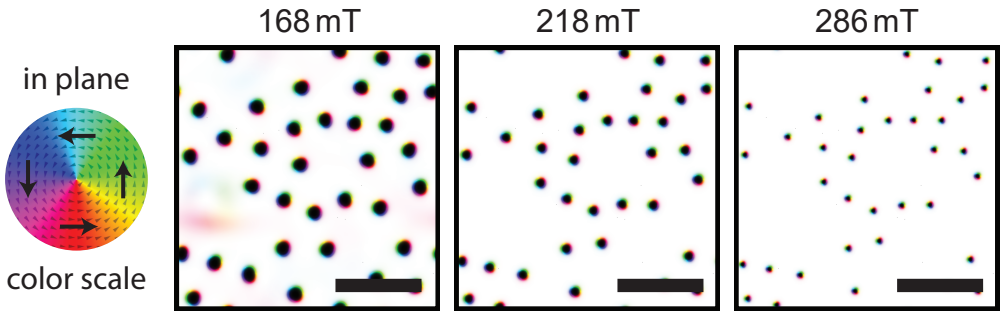

Fig. 5.14. – Magnetic texture at different fields from the micromagnetic simulations presented in Fig. 5.9. With increasing fields the skyrmion radii are compressed due to Zeeman-energy contributions. The simulations do not support compass anisotropy and do not reproduce the experimentally observed radius evolution. The simulations were performed by Lukas Körber.

and performed by Lukas Körber for this study do not include anisotropies caused by higher order spin-orbit coupling terms and accordingly are not able to reproduce the observed skyrmion size dependence (see Fig. 5.13). In Fig. 5.14, which shows the simulated magnetic texture at different fields, the reduction of skyrmion radius with increasing external magnetic field becomes evident. This discrepancy further supports the finding of a previously unconsidered stabilization mechanism existent in easy-plane iDMI multilayers. The detected radius evolution, however, requires the discernment of the investigated superlattice with ferromagnetically coupled CoFe layers from a multilayer system with antiferromagnetic coupling. Antiferromagnetically coupled skyrmions are predicted to exhibit a similar radius increase with increasing external magnetic fields [255] which was experimentally confirmed by recent work showing a soliton expansion [182].

5.4 Interlayer Exchange

The coupling sign of the interlayer exchange in the multilayer system can be determined by a thickness variation of the spacer layers. Especially Ir is often chosen for its mediation of the indirect exchange known as Ruderman-Kittel-Kasuya-Yosida (RKKY) interaction [244, 256–264]. The interaction introduces an oscillatory thickness dependent coupling between two ferromagnetic layers where the mediating spacer thickness determines the sign and strength of the exchange interaction. When the magnitude of the coupling is of minor relevance, the segregation of the two coupling regimes, i.e. antiferromagnetic or ferromagnetic, can easily be performed by measuring the saturation fields H_s of samples with varying spacer thickness [244, 264]. While H_s stays unperturbed for different ferromagnetic RKKY exchange strengths, it shows a dependence proportional to the RKKY interaction in the antiferromagnetic regime. In this case, the additional energy contribution opposes the homogeneous alignment due to Zeeman energy and thus increases the required magnetic field to reach a saturated state.

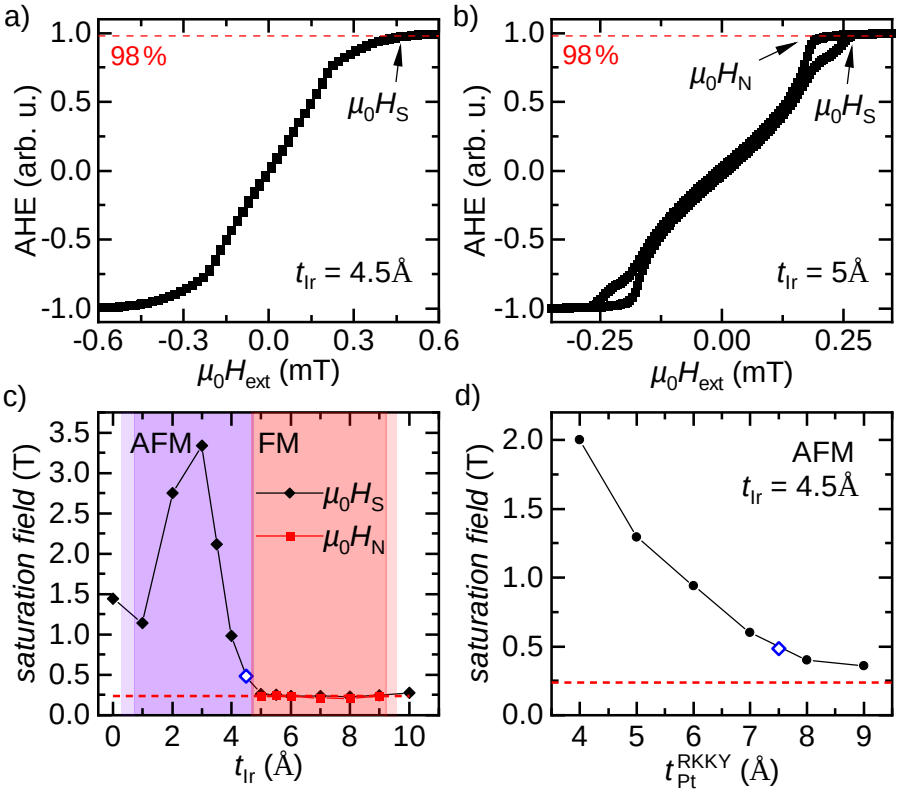

Fig. 5.15. – a) and b) show the normalized anomalous Hall effect signal for two multilayer samples with varying Ir-spacer thickness and CoFe thickness $t_{CoFe} = 1.145$ nm. The curve in a) corresponds to a sample with antiferromagnetic RKKY coupling of the multilayers, whereas the sample shown in b) represents ferromagnetic RKKY coupling. The saturation field $\mu_0 H_s$ is determined as the field above which the signal surpasses the 98 % threshold. For the ferromagnetically coupled samples hysteresis pockets close to $\mu_0 H_s$ are observed, which allow determining a nucleation field $\mu_0 H_N$ below which the homogeneous magnetic alignment decays and skyrmions start to nucleate. In panel c) the extracted saturation and nucleation fields for various samples with different Ir thicknesses are depicted. The antiferromagnetic RKKY coupling regime with increased saturation fields can be clearly distinguished from the ferromagnetic RKKY coupling regime, which coincides with the formation of hysteretic pockets. For panel d) a fixed Ir thickness indicated by the blue diamond symbol was selected an the Pt thickness was varied. For all investigated Pt thicknesses the RKKY coupling remains in the antiferromagnetic realm.

Anomalous Hall effect (AHE) measurements of two sets of samples with varying spacer thickness Pt(0.75)/CoFe(1.145)/Ir(t_{Ir}) and Pt(t_{Pt})/CoFe(1.145)/Ir(0.45) were used to analyze the qualitative coupling dependence. The samples for the AHE analysis were sputter deposited by Elisabeth Meidinger. In Fig. 5.15 a) and b) the hysteresis loops of two samples revealing antiferromagnetic and ferromagnetic coupling, respectively, are depicted. For the first sample, no hysteretic behavior is be observed, while the second shows hysteretic pockets close to $\mu_0 H_s$ similar to the magnetometry loops shown in Fig. 5.6. This allows to extract not only the magnetic field necessary in order to saturate the sample coming from remanence, but also provides a second magnetic field $\mu_0 H_N$ below which the magnetization decays and skyrmions can nucleate. Both fields are defined by a 98 % threshold

of the normalized AHE signal and are extracted for the samples. In Fig. 5.15 c) $\mu_0 H_s$ is plotted vs t_{Ir} which, apart from the qualitatively different hysteresis loops, permits a clear distinction between the two RKKY coupling signs. A peak of almost $\mu_0 H_s \approx 3.5\,\mathrm{mT}$ is detected at a thickness of $t_{Ir} = 3\,\text{Å}$ which drops significantly for higher or lower thicknesses matching the oscillatory expectation for the RKKY interaction mechanism. Above $t_{Ir} \geq 5\,\text{Å}$ $\mu_0 H_s$ maintains a constant value and the distinctive hysteresis pockets allow the determination of the nucleation field $\mu_0 H_N$. It becomes evident at this point, that the multilayer which reveals a qualitatively distinct radius evolution compared to PMA systems shows no antiferromagnetic coupling property. The second sample series with varying Pt thickness shown in Fig. 5.15 d) reveals that Ir is of major importance to dictate the coupling sign. For this set of samples, the Ir thickness is chosen to induce antiferromagnetic interlayer exchange yet also to be very close to the transition towards ferromagnetic coupling. While the strength of the indirect exchange scales inversely to t_{Pt} no qualitative change is observed within the investigated thicknesses. A very similar study on thickness variations of Ru, Ir and Pt spacers with qualitatively identical results has been performed by Karayev *et al.* [264] which corroborates the findings presented in this work. The high tunability of the saturation fields and thus the antiferromagnetic coupling strength of the presented multilayer provides a solid platform for the implementation of synthetic antiferromagnets in the future.

Additional to the distinction of the coupling sign MFM images of three samples of the presented Ir variation series with ferromagnetic, "weak" antiferromagnetic, and antiferromagnetic RKKY coupling were recorded. The influence of RKKY strength and sign on the magnetic texture is shortly discussed in Fig. 5.16 and Fig. 5.17. For the ferromagnetically coupled sample a labyrinthine state in remanence similar to Fig.5.3 g) is expected and observed in Fig. 5.16 b). It may be noted, that a small number of circular dots is visible which appear qualitatively different from the ambient MFM signal. These dots arise due to cross talk from the topography as shown in Fig. 5.16 a) with its relating arrows and do not represent the actual magnetic texture. When going to the antiferromagnetic coupling regime, the compensating magnetic moments are expected to reduce stray fields and thus to annihilate MFM contrast as seen with the sample with $t_{Ir} = 4\,\text{Å}$. Interestingly, this is not the case for the sample close to the transition with "weak" antiferromagnetic RKKY exchange with $t_{Ir} = 4.5\,\text{Å}$. While the saturation field is already slightly increased compared to the ferromagnetic samples and the hysteresis curve qualitatively compares to the antiferromagnetically coupled samples a labyrinthine state is observed. Such a behavior in synthetic antiferromagnets has been reported earlier by Hellwig *et al.*, where dipolar contributions overcome the RKKY coupling [244]. With externally applied magnetic field the two antiferromagnetically RKKY coupled samples also show unidentified features within the magnetic texture as seen in Fig. 5.17. Apart from normal skyrmions, which are expected to evolve from a labyrinthine state and increasing applied magnetic fields, several

circular shaped domains are observed which appear as "popped" or "inverted" bubbles in Fig. 5.17 a). Even the sample which shows vanishing MFM contrast at remanence due to an increased antiferromagnetic RKKY coupling, exhibits circular shaped domains at external magnetic fields. This findings underline the diversity of magnetic phenomena found in iDMI easy-plane multilayers and motivate further thorough investigation in the future.

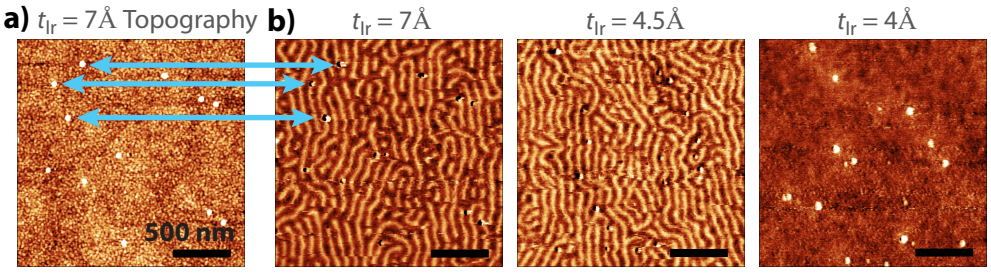

Fig. 5.16. – a) AFM image of the $t_{Ir} = 7$ Å investigated in Fig. 5.15 showing the topography with several grains visible as white dots. These dots cause a cross talk in the MFM images shown in b) and thus, circular textures in the MFM images at the corresponding sites do not stem from magnetic stray fields. In b) MFM images of three samples corresponding to ferromagnetic RKKY coupling ($t_{Ir} = 7$ Å), small antiferromagnetic RKKY coupling ($t_{Ir} = 4.5$ Å) and stronger antiferromagnetic RKKY coupling ($t_{Ir} = 4$ Å). For $t_{Ir} = 4.5$ Å, a labyrinthine magnetic state is still observed despite the antiferromagnetic coupling. For samples $t_{Ir} \leq 4$ Å, where the AFM coupling becomes stronger, no magnetic contrast is observed. The bright dots stem from topographic cross talk.

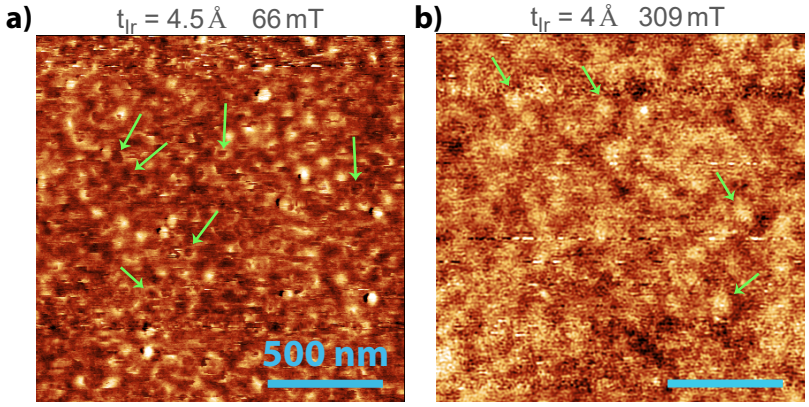

Fig. 5.17. – The antiferromagnetically coupled multilayer with $t_{Ir} = 4.5$ Å shows skyrmion formation at finite fields. The green arrows indicate unknown magnetic textures which appear like "popped" bubbles. Even the sample with stronger AFM coupling, which does not show any magnetic contrast in remanence shows circular magnetic textures at finite applied fields some of which are highlighted by green arrows as well.

Summary

6

This thesis elaborates the versatile possibilities of using ferromagnetic thin films based on the low-damping alloy CoFe for applications in the field of magnonics and skyrmionics. Thin films made of this material can easily be deposited by sputter deposition and patterned into nanostructured devices. The conducting properties imply direct compatibility of potential computational applications with today's already established charge-based technologies. These properties, together with the abundance of Fe and Co, provide a promising platform for novel technological applications that take advantage of the spin degree of freedom.

During this work, the low magnetic damping properties of the metallic alloy are optimized by proper seed, cap and spacer layers. Various relaxation mechanisms, like, e.g., spin pumping and intrinsic damping, are identified with help of broadband ferromagnetic resonance spectroscopy. The magnetic properties of the studied CoFe thin films were extracted from the resonance fields and linewidths. As a subsequent step, the confirmed low damping and the high saturation magnetization are exploited in a structured magnonic waveguide for studying spin-wave propagation. This work shows that CoFe thin films can reach characteristic decay lengths that are now comparable to thin film waveguides made out of the record-low damping, insulating ferrimagnet YIG [74]. CoFe thus provides an alternative to YIG for various magnonic applications that is not only cheaper, easier to fabricate and compatible to CMOS technology but also exhibits much higher spin-wave group velocities. Non-linear spin-wave phenomena that are currently exclusively studied in YIG, e.g. magnon Bose-Einstein condensates [68] could be soon realized in metallic systems with the help of CoFe.

The potential relevance and applicability for future studies and possible devices is further demonstrated in several collaborations based on the fabricated thin films. Spin waves in the non-linear regime are excited together with Hula *et al.*, where four-magnon scattering is studied in a first step [151]. By stimulating relaxation into discrete magnon states we show that four-magnon scattering can be used to create a magnonic frequency comb by two distinct driving frequencies [73]. In another collaboration with Wang *et al.* [265] we take advantage of the magnetic properties of CoFe nanogratings deposited on top of YIG. With help of the nano-patterned alloy, exchange spin waves can be excited efficiently in a YIG thin film. This approach underlines the material's potential not only as a waveguide itself but for applications exploiting magnon-magnon coupling phenomena. Looking into the near future, the investigation will be extended towards studying magnon-phonon coupling and evaluating CoFe's applicability for devices based on surface acoustic waves. When looking a bit further, even technological approaches that

were not investigated specifically throughout this work like, e.g., spin-torque nano-oscillators for neuromorphic computing could benefit from the low magnetic damping and the thus increased efficiencies.

In a second part of this thesis, we show that the alloy is not only useful for magnetodynamic applications but also for the stabilization of complex magnetic textures. We fabricate $[\mathrm{Pt/CoFe/Ir}]_N$ multilayers that exhibit strong interface Dzyaloshinskii-Moriya interaction (iDMI) such that chiral magnetic textures (skyrmions) are obtained. The system supports sub 100 nm skyrmions for a broad magnetic field range. Due to an effective easy-plane anisotropy energy density and higher-order spin-orbit coupling (SOC) mechanisms like compass anisotropies the skyrmion size is robust for a comparably broad range of magnetic fields. This stands in contrast to the usual shrinking of magnetic skyrmions with increased magnetic field due to increasing Zeeman penalties [236]. The observation motivates further research of the many consequences of higher-order SOC in sputter-deposited thin films. Additionally, the investigated multilayers provide a fruitful ground for current dependent measurements. The observed magnetic state shown by magnetic force microscopy could find its application in the first experimental proof of principle for skyrmion reservoir computing. Here, current pulses could excite magnetic resonances and change shape and size of pinned skyrmions. This would lead to an altered resistance response of the reservoir and thus enables for pattern recognition tasks depending on the current pulse shape and injection points [7].

The metallic ferromagnet CoFe that was employed for the thin-film heterostructures throughout this thesis results as a perfect material choice. We experimentally demonstrated record-long spin-wave propagation lengths in CoFe. The low damping could be exploited for non-linear spin-wave phenomena based on four-magnon scattering, which eventually allowed us to generate a magnonic frequency comb. Using a combined static and dynamic characterization of CoFe-based magnetic multilayers, we demonstrated robust formation of magnetic skyrmions accompanied by comparably low magnetic damping. While its high potential for magnonic and skyrmionic applications is directly and succesfully demonstrated various further research projects and questions will and can be addressed as mentioned above. Thus, our work allows to conclude that CoFe thin films represent a promising and versatile platform for future investigations and maybe someday will find its way into technological applications in industry.

Appendix A - Sample Fabrication

A

The fabricational details of sputter deposited multilayer thin films is presented in the following sections and tables.

A.1 Magnetodynamic Samples

The samples for the Gilbert damping analysis were deposited with a chamber pressure of 5×10^{-3} mBar, with an Argon flow of 10 sccm, and constant rotation speed of 20 rpm. Some of the samples were fabricated during the master thesis project.

Tab. A.1. – Sputter deposition parameters for the Ta(3)/Al(3)/CoFe(t)/Al(3)/Ta(3) samples used for the Gilbert damping analysis in Chapter 3.2.

Date	Material	MT4 (mm)	Power (W)	Rate (A/s)	Time (s)	XRD thickness (nm)
20.02.2018	Ta	50	30	2.09	15	3.1
	Al	70	50	1.30	23	2.7
	CoFe	70	25	2.28	22	4.69
	Al	70	50	1.30	23	2.1
	Ta (TaOx)	50	30	2.09	15	2.6
21.02.2018	Ta	50	30	2.09	15	3.2
	Al	70	50	1.30	23	2.5
	CoFe	70	25	2.28	15	2.81
	Al	70	50	1.30	23	3.5
	Ta (TaOx)	50	30	2.09	15	2.9
21.02.2018	Ta	50	30	2.09	15	3.1
	Al	70	50	1.30	23	2.9
	CoFe	70	25	2.28	11	1.41
	Al	70	50	1.30	23	2.4
	Ta (TaOx)	50	30	2.09	15	2.5
21.02.2018	Ta	50	30	2.09	15	3.1
	Al	70	50	1.30	23	3
	CoFe	70	25	2.28	9	1.14
	Al	70	50	1.30	23	2.6
	Ta (TaOx)	50	30	2.09	15	2.4
18.09.2018	Ta	50	30	2	15	3.3
* simulation optimized with intermixing and oxidation layers				Continued on next page		

Tab. A.1 – continued from previous page

Date	Material	MT4 (mm)	Power (W)	Rate (A/s)	Time (s)	XRD thickness (nm)
	Al	70	50	1.2	25	3.3
	CoFe	70	25	2.22	36	7.99
	Al	70	50	1.2	25	2.4
	Ta (TaAl/TaOx)	50	30	2	15	*
18.09.2018	Ta	50	30	2	15	3.2
	Al	70	50	1.2	25	3.3
	CoFe	70	25	2.19	32	6.91
	Al	70	50	1.2	25	2.85
	Ta (TaAl/TaOx)	50	30	2	15	*
18.09.2018	Ta	50	30	2	15	3.3
	Al	70	50	1.2	25	3.4
	CoFe	70	25	2.22	27	4.83
	Al	70	50	1.2	25	2.6
	Ta (TaAl/TaOx)	50	30	2	15	*
18.09.2018	Ta	50	30	2	15	3.4
	Al	70	50	1.2	25	3.2
	CoFe	70	25	2.17	23	4.66
	Al	70	50	1.2	25	2.9
	Ta (TaAl/TaOx)	50	30	2	15	*
19.09.2018	Ta	50	30	2	15	3
	Al	70	50	1.2	25	3
	CoFe	70	25	2.22	18	3.2
	Al	70	50	1.2	25	2
	Ta (TaAl/TaOx)	50	30	2	15	*
19.09.2018	Ta	50	30	2	15	3.4
	Al	70	50	1.2	25	3
	CoFe	70	25	2.22	9	1.47
	Al	70	50	1.2	25	2.7
	Ta (TaAl/TaOx)	50	30	2	15	*
19.11.2018	Ta	50	30	2	15	3.1
	Al	70	50	1.2	25	3.1
	CoFe	70	25	2.27	11	1.78
	Al	70	50	1.2	25	2.8
	Ta (TaAl/TaOx)	50	30	2	15	*
19.11.2018	Ta	50	30	2	15	2.9
	Al	70	50	1.2	25	2.6

* simulation optimized with intermixing and oxidation layers

Continued on next page

Tab. A.1 – continued from previous page

Date	Material	MT4 (mm)	Power (W)	Rate (A/s)	Time (s)	XRD thickness (nm)
	CoFe	70	25	2.14	14	2.53
	Al	70	50	1.2	25	2.6
	Ta (TaAl/TaOx)	50	30	2	15	*
23.11.2018	Ta	50	30	2	15	3.2
	Al	70	50	1.2	25	3.2
	CoFe	70	25	2.19	13	26.1
	Al	70	50	1.2	25	2.6
	Ta (TaAl/TaOx)	50	30	2	15	*
13.12.2018	Ta	70	40	0.68	44.18	3.2
	Al	70	40	1.37	21.9	3.1
	CoFe	70	25	2.38	63.03	13.5
	Al	70	40	1.37	21.9	2
	Ta (TaAl/TaOx)	70	40	0.68	44.18	*

The samples for the damping investigations are presented in Tabs. A.2, A.3 and A.1. Overall a chamber pressure of 5×10^{-3} mBar was used. The samples for the comparison of damping with (Tab. A.3) and without (Tab. A.2) spacer between the heavy metal and the magnetic metal where all fabricated with an argon flow of 10 sccm and a constant sample rotation of 30 rpm. The MT4 height was fixed to 70 mm for all materials.

Tab. A.2. – Ru(1.5)/CoFe(5)/Pt(t) samples with $t = (0.8, 1, 1.5, 2, 4, 10)$ nm for the comparison of damping with and without additional spacer layer investigated in Chap. 3.1.

Date	Material	Power (W)	Rate (A/s)	Time (s)
31.03.2020	Ru	10	1	15
	CoFe	20	1.84	27.17
	Pt	10	1.93	10.36
31.03.2020	Ru	10	1	15
	CoFe	20	1.84	27.17
	Pt	10	1.93	20.73
31.03.2020	Ru	10	1	15
	CoFe	20	1.84	27.17
	Pt	10	1.93	51.81
02.04.2020	Ru	10	1	15
	CoFe	20	1.84	27.17
	Pt	10	1.93	5.18
02.04.2020	Ru	10	1	15
	CoFe	20	1.84	27.17
	Pt	10	1.93	7.77
02.04.2020	Ru	10	1	15
	CoFe	20	1.84	27.17
	Pt	10	1.93	4.15

Tab. A.3. – Ru(1.5)/CoFe(5)/Cu(2)/Pt(t) samples with $t = (0.8, 1, 1.5, 2, 4, 10)$ nm for the comparison of damping with and without additional spacer layer investigated in Chap. 3.1.

Date	Material	Power (W)	Rate (A/s)	Time (s)
02.04.2020	Ru	10	1	15
	CoFe	20	1.91	26.18
	Cu	20	1.22	16.39
	Pt	10	1.36	4.08
02.04.2020	Ru	10	1	15
	CoFe	20	1.91	26.18
	Cu	20	1.22	16.39
	Pt	10	1.36	5.1
02.04.2020	Ru	10	1	15
	CoFe	20	1.91	26.18
	Cu	20	1.22	16.39
	Pt	10	1.36	7.65
02.04.2020	Ru	10	1	15
	CoFe	20	1.91	26.18
	Cu	20	1.22	16.39
	Pt	10	1.36	10.2
08.04.2020	Ru	10	0.97	15.46
	CoFe	20	1.96	25.51
	Cu	20	1.21	16.53
	Pt	10	1.93	20.73
08.04.2020	Ru	10	0.97	15.46
	CoFe	20	1.96	25.51
	Cu	20	1.21	16.53
	Pt	10	1.93	51.81

A.2 Thickness Variation Samples for Spin Spiral Configuration

The samples for the variation of M_{eff} were all fabricated at a chamber pressure of 5×10^{-3} mBar, an Argon flow of 10 sccm, a MT4 height of 70 mm, a constant rotation speed of 30 rpm on 03/23/2021. The total stack sequence on top of the SiOx (100) substrate is as follows: Ta(1.5)/Pt(4)/Cu(2)/[Pt(0.6)/CoFe(t)/Ir(0.7)]$_6$/Cu(2)/Ta(2.5) where the numbers are thickness in nm. By choosing proper deposition times τ the thicknesses $t = 0.9/1.1/1.3$ nm were selected. The individual material deposition parameters can be extracted from Tab. A.4.

Tab. A.4. – Sputter parameters for the materials of the sample series investigating varying M_{eff} for labyrinthine remanent state investigation in Chap. 5.2.

	Ta	Pt	Cu	CoFe	Ir
Power (W)	6	14	19	56	15
Rates (A/s)	0.58	0.69	1.09	1.01	0.41
Time (s)	25.86	57.97/8.7	18.35	τ	17.07

A.3 Brillouin Light Scattering Samples for DMI Quantification

The trilayer thin films for BLS examination and quantification of DMI constants were fabricated by Elisabeth Meidinger. The chamber pressure was 5×10^{-3} mBar, with an Argon flow of 10 sccm, a MT4 height of 70 mm, and constant rotation speed of 30 rpm. The total stack sequence on top of the SiOx (100) substrate is as follows: Ta(1.5)/Pt(4)/Cu(2)/[Pt(t_{Pt})/CoFe(t_{CF})/Ir(0.7)]$_1$/Cu(2)/Ta(2.5). The deposition parameters and respective thicknesses t_{Pt} and t_{CF} can be extracted from the Tabs. A.5 and A.6.

Tab. A.5. – Sputter parameters for the materials of the sample series for quantification of the DMI constant via BLS elaborated in Chap. 5.3.1.3. The deposition times in brackets represent the "default" value for the respective CoFe- or Pt-thickness range. Actual thicknesses and deposition times are listed in Tab. A.6.

	Ta	Pt	Cu	Ir	CoFe
Power (W)	6	14	19	15	56
Rates (A/s)	0.58	0.72	1.14	0.53	1.09
Time (s)	25.86/43.1	55.56/(8.33)	17.54	16.67	(10.5)

Tab. A.6. – Deposition times and thicknesses of the CoFe- and Pt-series for DMI quantification. The deposition times in brackets represent the "default" value for the CoFe- or Pt-thickness range when not varied. The sample fabricated with the values presented in brackets is an only sample, such that 9 samples were fabricated in total. The individual material deposition parameters are found in Tab A.5.

CoFe Series		Pt Series	
Thickness	Time	Thickness	Time
0.95	8.72	0.2	2.78
(1.145)	(10.5)	0.4	5.56
1.5	13.76	(0.6)	(8.33)
2	18.35	0.8	11.11
3	27.52	1	13.89

A.4 Samples for Qualitative Interlayer Exchange Investigation

The multilayer thin films for AHE measurements and qualitative RKKY investigation were fabricated by Elisabeth Meidinger. The chamber pressure was 5×10^{-3} mBar, with an Argon flow of 10 sccm, a MT4 height of 70 mm, and constant rotation speed of 30 rpm. The total stack sequence on top of the SiOx (100) substrate is as follows: Ta(1.5)/Pt(4)/Cu(2)/[Pt(t_{Pt})/CoFe(t_{CoFe})/Ir(0.7)]$_6$/Cu(2)/Ta(2.5). The deposition parameters and respective thicknesses t_{Pt} and t_{CF} can be extracted from the Tabs. A.5 and A.6

Tab. A.7. – Sputter parameters for the materials of the sample series for AHE measurements and determination of qualitative RKKY coupling discussed in Chap 5.4. Actual thicknesses and deposition times are listed in Tab. A.8.

	Ta	Pt	Cu	CoFe	Ir
Power (W)	6	14	19	56	15
Rate (A/s)	0.57	0.75	1.13	1.02	0.445
Time (s)	26.31	53.33/(10)	17.7	11.23	(10.11)

Tab. A.8. – Deposition times and thicknesses of the Pt- and Ir-series for AHE measurements. The individual material deposition parameters are found in Tab. A.7.

Ir Series			Pt Series		
Date	Thickness	Time	Date	Thickness	Time
29.10.2020	0.2	4.49	29.10.2020	0.4	5.33
29.10.2020	0.3	6.74	29.10.2020	0.5	6.67
29.10.2020	0.35	7.87	29.10.2020	0.6	8
29.10.2020	0.4	8.99	29.10.2020	0.7	9.33
29.10.2020	0.45	10.11	29.10.2020	0.8	10.67
29.10.2020	0.5	11.24	29.10.2020	0.9	12
29.10.2020	0.55	12.36			
29.10.2020	0.6	13.48			
29.10.2020	0.7	15.73			
29.10.2020	0.8	17.98			
29.10.2020	0.9	20.22			
29.10.2020	1	22.47			
05.11.2020	0.1	2.25			
05.11.2020	0	0			

Appendix B - MFM Field Calibration

B

The calibration list was recorded by Simon Mendisch. Fig. B.1 shows the calibration table with available magnetic fields between roughly 66 mT and 309 mT.

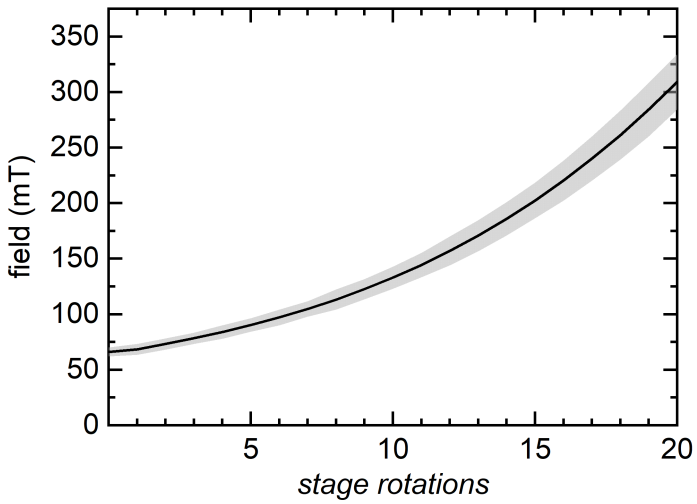

Fig. B.1. – Calibration of the permanent magnet height to magnetic field at the sample surface. The large uncertainty of the field is a maximum estimate due to the uncertainty of the active area position inside the used Hall probe.

List of publications

- L. Flacke, V. Ahrens, S. Mendisch, L. Körber, T. Böttcher, E. Meidinger, M. Yaqoob, M. Müller, L. Liensberger, A. Kákay, M. Becherer, P. Pirro, M. Althammer, S. Geprägs, H. Huebl, R. Gross, M. Weiler, *Robust formation of nanoscale magnetic skyrmions in easy-plane anisotropy thin film multilayers with low damping*, Physical Review B **104**, L100417 (2021).

- H. Wang, L. Flacke, W. Wei, S. Liu, H. Jia, J. Chen, L. Sheng, J. Zhang, M. Zhao, C. Guo, C. Fang, X. Han, D. Yu, M. Althammer, M. Weiler, H. Yu, *Sub-50 nm wavelength spin waves excited by low-damping Co 25 Fe 75 nanowires*, Applied Physics Letters **119**, 152402 (2021).

- T. Hula, K. Schultheiss, F.J.T. Goncalves, L. Körber, M. Bejarano, M. Copus, L. Flacke, L. Liensberger, A. Buzdakov, A. Kákay, M. Weiler, R. Camley, J. Fassbender, H. Schultheiß, *Spin-wave frequency combs*, arXiv: 2104.11491 (2021). (submitted 2021)

- M. Küß, M. Heigl, L. Flacke, A. Hefele, A. Hörner, M. Weiler, M. Albrecht, A. Wixforth, *Symmetry of the Magnetoelastic Interaction of Rayleigh and Shear Horizontal Magnetoacoustic Waves in Nickel Thin Films on $LiTaO_3$*, Physical Review Applied **15**, 034046 (2021).

- M. Küß, M. Heigl, L. Flacke, A. Hörner, M. Weiler, A. Wixforth, M. Albrecht, *Nonreciprocal Magnetoacoustic Waves in Dipolar-Coupled Ferromagnetic Bilayers*, Physical Review Applied **15**, 034060 (2021).

- M. Müller, L. Liensberger, L. Flacke, H. Huebl, A. Kamra, W. Belzig, R. Gross, M. Weiler, M. Althammer, *Temperature-Dependent Spin Transport and Current-Induced Torques in Superconductor-Ferromagnet Heterostructures*, Physical Review Letters **126**, 087201 (2021).

- T. Hula, K. Schultheiss, A. Buzdakov, L. Körber, M. Bejarano, L. Flacke, L. Liensberger, M. Weiler, J.M. Shaw, H.T. Nembach, J. Fassbender, H. Schultheiss, *Nonlinear losses in magnon transport due to four-magnon scattering*, Applied Physics Letters **117**, 042404 (2020).

- M. Küß, M. Heigl, L. Flacke, A. Hörner, M. Weiler, M. Albrecht, A. Wixforth, *Nonreciprocal Dzyaloshinskii–Moriya Magnetoacoustic Waves*, Physical Review Letters **125**, 217203 (2020).
- L. Flacke, L. Liensberger, M. Althammer, H. Huebl, S. Geprägs, K. Schultheiss, A. Buzdakov, T. Hula, H. Schultheiss, E.R.J. Edwards, H.T. Nembach, J.M. Shaw, R. Gross, M. Weiler, *High spin-wave propagation length consistent with low damping in a metallic ferromagnet*, Applied Physics Letters **115**, 122402 (2019).
- L. Liensberger, L. Flacke, D. Rogerson, M. Althammer, R. Gross, M. Weiler, *Spin-Wave Propagation in Metallic $Co_{25}Fe_{75}$ Films Determined by Microfocused Frequency-Resolved Magneto-Optic Kerr Effect*, IEEE Magnetics Letters **10**, 5503905 (2019).

Bibliography

[1] G.E. Moore, *Cramming more components onto integrated circuits*, IEEE Solid-State Circuits Society Newsletter **11**, 33 (2006).

[2] M.M. Waldrop, *The chips are down for Moore's law*, Nature **530**, 144 (2016).

[3] M. Romera, P. Talatchian, S. Tsunegi, F. Abreu Araujo, V. Cros, P. Bortolotti, J. Trastoy, K. Yakushiji, A. Fukushima, H. Kubota, S. Yuasa, M. Ernoult, D. Vodenicarevic, T. Hirtzlin, N. Locatelli, D. Querlioz, J. Grollier, *Vowel recognition with four coupled spin-torque nano-oscillators*, Nature **563**, 230 (2018).

[4] S. Ambrogio, P. Narayanan, H. Tsai, R.M. Shelby, I. Boybat, C. di Nolfo, S. Sidler, M. Giordano, M. Bodini, N.C.P. Farinha, B. Killeen, C. Cheng, Y. Jaoudi, G.W. Burr, *Equivalent-accuracy accelerated neural-network training using analogue memory*, Nature **558**, 60 (2018).

[5] T. Chen, R.K. Dumas, A. Eklund, P.K. Muduli, A. Houshang, A.A. Awad, P. Durrenfeld, B.G. Malm, A. Rusu, J. Akerman, *Spin-Torque and Spin-Hall Nano-Oscillators*, Proceedings of the IEEE **104**, 1919 (2016).

[6] S. Tsunegi, T. Taniguchi, R. Lebrun, K. Yakushiji, V. Cros, J. Grollier, A. Fukushima, S. Yuasa, H. Kubota, *Scaling up electrically synchronized spin torque oscillator networks*, Scientific Reports **8**, 13475 (2018).

[7] D. Pinna, G. Bourianoff, K. Everschor-Sitte, *Reservoir Computing with Random Skyrmion Textures*, Physical Review Applied **14**, 054020 (2020).

[8] P. del Hougne, G. Lerosey, *Leveraging Chaos for Wave-Based Analog Computation: Demonstration with Indoor Wireless Communication Signals*, Physical Review X **8**, 041037 (2018).

[9] V.V. Kruglyak, S.O. Demokritov, D. Grundler, *Magnonics*, Journal of Physics D: Applied Physics **43**, 264001 (2010).

[10] A.V. Chumak, V.I. Vasyuchka, A.A. Serga, B. Hillebrands, *Magnon spintronics*, Nature Physics **11**, 453 (2015).

[11] T. Seifert, S. Jaiswal, U. Martens, J. Hannegan, L. Braun, P. Maldonado, F. Freimuth, A. Kronenberg, J. Henrizi, I. Radu, E. Beaurepaire, Y. Mokrousov,

P.M. Oppeneer, M. Jourdan, G. Jakob, D. Turchinovich, L.M. Hayden, M. Wolf, M. Münzenberg, M. Kläui, T. Kampfrath, *Efficient metallic spintronic emitters of ultrabroadband terahertz radiation*, Nature Photonics **10**, 483 (2016).

[12] S. Bader, S. Parkin, *Spintronics*, Annual Review of Condensed Matter Physics **1**, 71 (2010).

[13] C. Back, V. Cros, H. Ebert, K. Everschor-Sitte, A. Fert, M. Garst, T. Ma, S. Mankovsky, T.L. Monchesky, M. Mostovoy, N. Nagaosa, S.S.P. Parkin, C. Pfleiderer, N. Reyren, A. Rosch, Y. Taguchi, Y. Tokura, K. von Bergmann, J. Zang, *The 2020 skyrmionics roadmap*, Journal of Physics D: Applied Physics **53**, 363001 (2020).

[14] A.A. Serga, A.V. Chumak, B. Hillebrands, *YIG magnonics*, Journal of Physics D: Applied Physics **43**, 264002 (2010).

[15] M.A.W. Schoen, J.M. Shaw, H.T. Nembach, M. Weiler, T.J. Silva, *Radiative damping in waveguide-based ferromagnetic resonance measured via analysis of perpendicular standing spin waves in sputtered permalloy films*, Physical Review B **92**, 184417 (2015).

[16] A. Vansteenkiste, J. Leliaert, M. Dvornik, M. Helsen, F. Garcia-Sanchez, B. Van Waeyenberge, *The design and verification of MuMax3*, AIP Advances **4**, 107133 (2014).

[17] S. Vonsovskii, *Ferromagnetic Resonance*, Elsevier (1966).

[18] A.G. Gurevich, G.A. Melkov, *Magnetization Oscillations and Waves*, CRC Press (1996).

[19] D.D. Stancil, A. Prabhakar, *Spin Waves* 332 (2009).

[20] L. Landau, E. Lifshits, *On the Theory of the Dispersion of Magnetic Permeability in Ferromagnetic Bodies*, Phys. Z. Sowietunion **8** (1935).

[21] T. Gilbert, *A Phenomenological Theory of Damping in Ferromagnetic Materials*, IEEE Transactions on Magnetics **40**, 3443 (2004).

[22] C. Kittel, *On the theory of ferromagnetic resonance absorption*, Physical Review **73**, 155 (1948).

[23] B.A. Kalinikos, A.N. Slavin, *Theory of dipole-exchange spin wave spectrum for ferromagnetic films with mixed exchange boundary conditions*, Journal of Physics C: Solid State Physics **19**, 7013 (1986).

[24] R. Gross, A. Marx, *Festkörperphysik*, De Gruyter Oldenbourg, München, 2. Ed. (2014).

[25] J.M.D. Coey, *Magnetism and Magnetic Materials*, Cambridge University Press (2009).

[26] S. Blundell, *Magnetism in Condensed Matter*, Oxford University Press (2001).

[27] T. Miyazaki, H. Jin, *The Physics of Ferromagnetism*, Vol. 158 von *Springer Series in Materials Science*, Springer Berlin Heidelberg, Berlin, Heidelberg (2012).

[28] H. Maier-Flaig, *Magnetic resonance of ferrimagnetic insulators*, PhD thesis, Technische Universität München (2018).

[29] L. Liensberger, *Magnon Hybrid Dynamics*, PhD thesis, Technische Universität München (2021).

[30] S.H. Klingler, *Magnetization Dynamics in Coupled Thin Film Systems*, PhD thesis, Technische Universität München (2019).

[31] M. Weiler, *Magnetization Dynamics and Spin Torques in Exchange-Coupled Spin Systems*, Habilitation, Technische Universität München (2019).

[32] L. Flacke, *Spin Pumping and Spin Wave Damping in Co25Fe75 Thin Film Heterostructures*, PhD thesis, Technische Universität München (2018).

[33] P.D. Louis, *Broadband-Spectroscopy of Magnetic Materials at Low Temperatures*, Master thesis, Technische Universität München (2016).

[34] W. Heisenberg, *Zur Theorie des Ferromagnetismus*, Zeitschrift für Physik **49**, 619 (1928).

[35] J.G. Gay, R. Richter, *Spin Anisotropy of Ferromagnetic Films*, Physical Review Letters **56**, 2728 (1986).

[36] G.H.O. Daalderop, P.J. Kelly, M.F.H. Schuurmans, *Magnetic anisotropy of a free-standing Co monolayer and of multilayers which contain Co monolayers*, Physical Review B **50**, 9989 (1994).

[37] D. Weller, J. Stöhr, R. Nakajima, A. Carl, M.G. Samant, C. Chappert, R. Mégy, P. Beauvillain, P. Veillet, G.A. Held, *Microscopic Origin of Magnetic Anisotropy in Au/Co/Au Probed with X-Ray Magnetic Circular Dichroism*, Physical Review Letters **75**, 3752 (1995).

[38] J. Stöhr, *Exploring the microscopic origin of magnetic anisotropies with X-ray magnetic circular dichroism (XMCD) spectroscopy*, Journal of Magnetism and Magnetic Materials **200**, 470 (1999).

[39] M. Wolloch, D. Suess, *Strain-induced control of magnetocrystalline anisotropy energy in FeCo thin films*, Journal of Magnetism and Magnetic Materials **522**, 167542 (2021).

[40] P.F. Carcia, *Perpendicular magnetic anisotropy in Pd/Co and Pt/Co thin-film layered structures*, Journal of Applied Physics **63**, 5066 (1988).

[41] C. Chappert, K.L. Dang, P. Beauvillain, H. Hurdequint, D. Renard, *Ferromagnetic resonance studies of very thin cobalt films on a gold substrate*, Physical Review B **34**, 3192 (1986).

[42] G.H.O. Daalderop, P.J. Kelly, F.J.A. den Broeder, *Prediction and confirmation of perpendicular magnetic anisotropy in Co/Ni multilayers*, Physical Review Letters **68**, 682 (1992).

[43] F. Gimbert, L. Calmels, *First-principles investigation of the magnetic anisotropy and magnetic properties of Co/Ni(111) superlattices*, Physical Review B **86**, 184407 (2012).

[44] F. Hellman, A. Hoffmann, Y. Tserkovnyak, G.S.D. Beach, E.E. Fullerton, C. Leighton, A.H. MacDonald, D.C. Ralph, D.A. Arena, H.A. Dürr, P. Fischer, J. Grollier, J.P. Heremans, T. Jungwirth, A.V. Kimel, B. Koopmans, I.N. Krivorotov, S.J. May, A.K. Petford-Long, J.M. Rondinelli, N. Samarth, I.K. Schuller, A.N. Slavin, M.D. Stiles, O. Tchernyshyov, A. Thiaville, B.L. Zink, *Interface-induced phenomena in magnetism*, Reviews of Modern Physics **89**, 025006 (2017).

[45] B. Heinrich, J. Bland, *Ultrathin Magnetic Structures II*, Springer Berlin Heidelberg, Berlin, Heidelberg (1994).

[46] J.M. Lock, *Eddy current damping in thin metallic ferromagnetic films*, British Journal of Applied Physics **17**, 1645 (1966).

[47] P. Pincus, *Excitation of spin waves in ferromagnets: eddy current and boundary condition effects*, Physical Review **118**, 658 (1960).

[48] D. Polder, *On the theory of ferromagnetic resonance*, The London, Edinburgh, and Dublin Philosophical Magazine and Journal of Science **40**, 99 (1949).

[49] L. Liensberger, *Spin-Orbit Torques and Magnetization Dynamics in Non-collinear Magnets*, Master thesis, Technische Universität München (2017).

[50] O. Karlqvist, *Calculation of the magnetic field in the ferromagnetic layer of a magnetic drum* (1954).

[51] Z. Ma, D. Seiler, *Metrology and Diagnostic Techniques for Nanoelectronics*, Pan Stanford Publishing, Singapore, -1 (2016).

[52] S. Klingler, P. Pirro, T. Brächer, B. Leven, B. Hillebrands, A.V. Chumak, *Spin-wave logic devices based on isotropic forward volume magnetostatic waves*, Applied Physics Letters **106**, 212406 (2015).

[53] M.P. Kostylev, A.A. Serga, T. Schneider, B. Leven, B. Hillebrands, *Spin-wave logical gates*, Applied Physics Letters **87**, 153501 (2005).

[54] T. Fischer, M. Kewenig, D.A. Bozhko, A.A. Serga, I.I. Syvorotka, F. Ciubotaru, C. Adelmann, B. Hillebrands, A.V. Chumak, *Experimental prototype of a spin-wave majority gate*, Applied Physics Letters **110**, 152401 (2017).

[55] A. Khitun, Mingqiang Bao, K. Wang, *Spin Wave Magnetic NanoFabric: A New Approach to Spin-Based Logic Circuitry*, IEEE Transactions on Magnetics **44**, 2141 (2008).

[56] A.V. Chumak, A.A. Serga, B. Hillebrands, *Magnon transistor for all-magnon data processing*, Nature Communications **5**, 4700 (2014).

[57] K. Ganzhorn, S. Klingler, T. Wimmer, S. Geprägs, R. Gross, H. Huebl, S.T.B. Goennenwein, *Magnon-based logic in a multi-terminal YIG/Pt nanostructure*, Applied Physics Letters **109**, 022405 (2016).

[58] J.H. Moon, S.M. Seo, K.J. Lee, K.W. Kim, J. Ryu, H.W. Lee, R.D. McMichael, M.D. Stiles, *Spin-wave propagation in the presence of interfacial Dzyaloshinskii-Moriya interaction*, Physical Review B **88**, 184404 (2013).

[59] R.W. Damon, J.R. Eshbach, *Magnetostatic modes of a ferromagnet slab*, Journal of Physics and Chemistry of Solids **19**, 308 (1961).

[60] A. Barman, G. Gubbiotti, S. Ladak, A.O. Adeyeye, M. Krawczyk, J. Gräfe, C. Adelmann, S. Cotofana, A. Naeemi, V.I. Vasyuchka, B. Hillebrands, S.A. Nikitov, H. Yu, D. Grundler, A.V. Sadovnikov, A.A. Grachev, S.E. Sheshukova, J.Y. Duquesne, M. Marangolo, G. Csaba, W. Porod, V.E. Demidov, S. Urazhdin, S.O. Demokritov, E. Albisetti, D. Petti, R. Bertacco, H. Schultheiss, V.V. Kruglyak, V.D. Poimanov, S. Sahoo, J. Sinha, H. Yang, M. Münzenberg, T. Moriyama, S. Mizukami, P. Landeros, R.A. Gallardo, G. Carlotti, J.V. Kim, R.L. Stamps, R.E. Camley, B. Rana, Y. Otani, W. Yu, T. Yu, G.E.W. Bauer, C. Back, G.S. Uhrig, O.V. Dobrovolskiy, B. Budinska, H. Qin, S. van Dijken, A.V. Chumak, A. Khitun, D.E. Nikonov, I.A. Young, B.W. Zingsem, M. Winklhofer, *The 2021 Magnonics Roadmap*, Journal of Physics: Condensed Matter **33**, 413001 (2021).

[61] L. Sheng, J. Chen, H. Wang, H. Yu, *Magnonics Based on Thin-Film Iron Garnets*, Journal of the Physical Society of Japan **90**, 081005 (2021).

[62] H. Yu, O. d' Allivy Kelly, V. Cros, R. Bernard, P. Bortolotti, A. Anane, F. Brandl, F. Heimbach, D. Grundler, *Approaching soft X-ray wavelengths in nanomagnet-based microwave technology*, Nature Communications **7**, 11255 (2016).

[63] P. Che, K. Baumgaertl, A. Kúkol'ová, C. Dubs, D. Grundler, *Efficient wavelength conversion of exchange magnons below 1oo nm by magnetic coplanar waveguides*, Nature Communications **11**, 1445 (2020).

[64] J. Chen, C. Liu, T. Liu, Y. Xiao, K. Xia, G.E.W. Bauer, M. Wu, H. Yu, *Strong Interlayer Magnon-Magnon Coupling in Magnetic Metal-Insulator Hybrid Nanostructures*, Physical Review Letters **120**, 217202 (2018).

[65] J. Chen, T. Yu, C. Liu, T. Liu, M. Madami, K. Shen, J. Zhang, S. Tu, M.S. Alam, K. Xia, M. Wu, G. Gubbiotti, Y.M. Blanter, G.E.W. Bauer, H. Yu, *Excitation of unidirectional exchange spin waves by a nanoscale magnetic grating*, Physical Review B **100**, 104427 (2019).

[66] Y. Li, W.E. Bailey, *Wave-Number-Dependent Gilbert Damping in Metallic Ferromagnets*, Physical Review Letters **116**, 117602 (2016).

[67] F. Kargar, A.A. Balandin, *Advances in Brillouin–Mandelstam light-scattering spectroscopy*, Nature Photonics (2021).

[68] S.O. Demokritov, V.E. Demidov, O. Dzyapko, G.A. Melkov, A.A. Serga, B. Hillebrands, A.N. Slavin, *Bose–Einstein condensation of quasi-equilibrium magnons at room temperature under pumping*, Nature **443**, 430 (2006).

[69] T. Sebastian, K. Schultheiss, B. Obry, B. Hillebrands, H. Schultheiss, *Micro-focused Brillouin light scattering: imaging spin waves at the nanoscale*, Frontiers in Physics **3**, 35 (2015).

[70] H.T. Nembach, J.M. Shaw, M. Weiler, E. Jué, T.J. Silva, *Linear relation between Heisenberg exchange and interfacial Dzyaloshinskii–Moriya interaction in metal films*, Nature Physics **11**, 825 (2015).

[71] C.W. Sandweg, M.B. Jungfleisch, V.I. Vasyuchka, A.A. Serga, P. Clausen, H. Schultheiss, B. Hillebrands, A. Kreisel, P. Kopietz, *Wide-range wavevector selectivity of magnon gases in Brillouin light scattering spectroscopy*, Review of Scientific Instruments **81**, 073902 (2010).

[72] T. Brächer, F. Heussner, P. Pirro, T. Fischer, M. Geilen, B. Heinz, B. Lägel, A.A. Serga, B. Hillebrands, *Time- and power-dependent operation of a parametric spin-wave amplifier*, Applied Physics Letters **105**, 232409 (2014).

[73] T. Hula, K. Schultheiss, F.J.T. Goncalves, L. Körber, M. Bejarano, M. Copus, L. Flacke, L. Liensberger, A. Buzdakov, A. Kákay, M. Weiler, R. Camley, J. Fassbender, H. Schultheiß, *Spin-wave frequency combs*, arXiv: 2104.11491 (2021).

[74] L. Flacke, L. Liensberger, M. Althammer, H. Huebl, S. Geprägs, K. Schultheiss, A. Buzdakov, T. Hula, H. Schultheiss, E.R.J. Edwards, H.T.

Nembach, J.M. Shaw, R. Gross, M. Weiler, *High spin-wave propagation length consistent with low damping in a metallic ferromagnet*, Applied Physics Letters **115**, 122402 (2019).

[75] M.B. Jungfleisch, W. Zhang, W. Jiang, H. Chang, J. Sklenar, S.M. Wu, J.E. Pearson, A. Bhattacharya, J.B. Ketterson, M. Wu, A. Hoffmann, *Spin waves in micro-structured yttrium iron garnet nanometer-thick films*, Journal of Applied Physics **117**, 17D128 (2015).

[76] K. Vogt, H. Schultheiss, S.J. Hermsdoerfer, P. Pirro, A.A. Serga, B. Hillebrands, *All-optical detection of phase fronts of propagating spin waves in a Ni81Fe19 microstripe*, Applied Physics Letters **95**, 182508 (2009).

[77] J. Sandercock, *Tandem Fabry-Perot Spectrometers TFP-1 and TFP-2 HC*, Operator manual, Mettmenstetten, Switzerland (2020).

[78] H. Yusuf, M. Chilcote, D.R. Candido, S. Kurfman, D.S. Cormode, Y. Lu, M.E. Flatté, E. Johnston-Halperin, *Exploring a quantum-information-relevant magnonic material: Ultralow damping at low temperature in the organic ferrimagnet V[TCNE] x*, AVS Quantum Science **3**, 026801 (2021).

[79] M. Julliere, *Tunneling between ferromagnetic films*, Physics Letters A **54**, 225 (1975).

[80] S. Bhatti, R. Sbiaa, A. Hirohata, H. Ohno, S. Fukami, S.N. Piramanayagam, *Spintronics based random access memory: a review*, Materials Today **20**, 530 (2017).

[81] H. Suhl, *Theory of the magnetic damping constant*, IEEE Transactions on Magnetics **34**, 1834 (1998).

[82] O. Chubykalo, U. Nowak, R. Smirnov-Rueda, M.A. Wongsam, R.W. Chantrell, J.M. Gonzalez, *Monte Carlo technique with a quantified time step: Application to the motion of magnetic moments*, Physical Review B **67**, 064422 (2003).

[83] M. Collet, O. Gladii, M. Evelt, V. Bessonov, L. Soumah, P. Bortolotti, S.O. Demokritov, Y. Henry, V. Cros, M. Bailleul, V.E. Demidov, A. Anane, *Spin-wave propagation in ultra-thin YIG based waveguides*, Applied Physics Letters **110**, 092408 (2017).

[84] C. Hauser, T. Richter, N. Homonnay, C. Eisenschmidt, M. Qaid, H. Deniz, D. Hesse, M. Sawicki, S.G. Ebbinghaus, G. Schmidt, *Yttrium Iron Garnet Thin Films with Very Low Damping Obtained by Recrystallization of Amorphous Material*, Scientific Reports **6**, 20827 (2016).

[85] M. Evelt, V.E. Demidov, V. Bessonov, S.O. Demokritov, J.L. Prieto, M. Muñoz, J. Ben Youssef, V.V. Naletov, G. de Loubens, O. Klein, M. Collet, K. Garcia-Hernandez, P. Bortolotti, V. Cros, A. Anane, *High-efficiency control of spin-wave*

propagation in ultra-thin yttrium iron garnet by the spin-orbit torque, Applied Physics Letters **108**, 172406 (2016).

[86] H. Yu, O. d'Allivy Kelly, V. Cros, R. Bernard, P. Bortolotti, A. Anane, F. Brandl, R. Huber, I. Stasinopoulos, D. Grundler, *Magnetic thin-film insulator with ultra-low spin wave damping for coherent nanomagnonics*, Scientific Reports **4**, 6848 (2015).

[87] Y. Kajiwara, K. Harii, S. Takahashi, J. Ohe, K. Uchida, M. Mizuguchi, H. Umezawa, H. Kawai, K. Ando, K. Takanashi, S. Maekawa, E. Saitoh, *Transmission of electrical signals by spin-wave interconversion in a magnetic insulator*, Nature **464**, 262 (2010).

[88] T. Schneider, A.A. Serga, B. Leven, B. Hillebrands, R.L. Stamps, M.P. Kostylev, *Realization of spin-wave logic gates*, Applied Physics Letters **92**, 022505 (2008).

[89] Houchen Chang, Peng Li, Wei Zhang, Tao Liu, A. Hoffmann, Longjiang Deng, Mingzhong Wu, *Nanometer-Thick Yttrium Iron Garnet Films With Extremely Low Damping*, IEEE Magnetics Letters **5**, 6700104 (2014).

[90] M. Tokaç, S.A. Bunyaev, G.N. Kakazei, D.S. Schmool, D. Atkinson, A.T. Hindmarch, *Interfacial Structure Dependent Spin Mixing Conductance in Cobalt Thin Films*, Physical Review Letters **115**, 056601 (2015).

[91] T. Gerrits, M.L. Schneider, T.J. Silva, *Enhanced ferromagnetic damping in Permalloy/Cu bilayers*, Journal of Applied Physics **99** (2006).

[92] E.C.I. Enobio, H. Sato, S. Fukami, F. Matsukura, H. Ohno, *CoFeB Thickness Dependence of Damping Constants for Single and Double CoFeB-MgO Interface Structures*, IEEE Magnetics Letters **6**, 5700303 (2015).

[93] M.A.W. Schoen, D. Thonig, M.L. Schneider, T.J. Silva, H.T. Nembach, O. Eriksson, O. Karis, J.M. Shaw, *Ultra-low magnetic damping of a metallic ferromagnet*, Nature Physics **12**, 839 (2016).

[94] E.R. Edwards, H.T. Nembach, J.M. Shaw, *Co25Fe75 Thin Films with Ultralow Total Damping of Ferromagnetic Resonance*, Physical Review Applied **11**, 054036 (2019).

[95] R. Weber, D.S. Han, I. Boventer, S. Jaiswal, R. Lebrun, G. Jakob, M. Kläui, *Gilbert damping of CoFe-alloys*, Journal of Physics D: Applied Physics **52**, 325001 (2019).

[96] A.A. Awad, P. Dürrenfeld, A. Houshang, M. Dvornik, E. Iacocca, R.K. Dumas, J. Åkerman, *Long-range mutual synchronization of spin Hall nano-oscillators*, Nature Physics **13**, 292 (2016).

[97] S. Kaka, M.R. Pufall, W.H. Rippard, T.J. Silva, S.E. Russek, J.A. Katine, *Mutual phase-locking of microwave spin torque nano-oscillators*, Nature **437**, 389 (2005).

[98] V. Demidov, S. Urazhdin, G. de Loubens, O. Klein, V. Cros, A. Anane, S. Demokritov, *Magnetization oscillations and waves driven by pure spin currents*, Physics Reports **673**, 1 (2017).

[99] L. Liu, T. Moriyama, D.C. Ralph, R.A. Buhrman, *Spin-torque ferromagnetic resonance induced by the spin Hall effect*, Physical Review Letters **106**, 1 (2011).

[100] V.E. Demidov, S. Urazhdin, E.R. Edwards, S.O. Demokritov, *Wide-range control of ferromagnetic resonance by spin Hall effect*, Applied Physics Letters **99**, 10 (2011).

[101] W. Jiang, X. Zhang, G. Yu, W. Zhang, X. Wang, M. Benjamin Jungfleisch, J.E. Pearson, X. Cheng, O. Heinonen, K.L. Wang, Y. Zhou, A. Hoffmann, S.G.E. te Velthuis, *Direct observation of the skyrmion Hall effect*, Nature Physics **13**, 162 (2017).

[102] K. Litzius, I. Lemesh, B. Krüger, P. Bassirian, L. Caretta, K. Richter, F. Büttner, K. Sato, O.A. Tretiakov, J. Förster, R.M. Reeve, M. Weigand, I. Bykova, H. Stoll, G. Schütz, G.S.D. Beach, M. Kläui, *Skyrmion Hall effect revealed by direct time-resolved X-ray microscopy*, Nature Physics **13**, 170 (2017).

[103] K. Chen, S. Zhang, *Spin Pumping in the Presence of Spin-Orbit Coupling*, Physical Review Letters **114**, 126602 (2015).

[104] K. Dolui, B.K. Nikolić, *Spin-memory loss due to spin-orbit coupling at ferromagnet/heavy-metal interfaces: Ab initio spin-density matrix approach*, Physical Review B **96**, 220403 (2017).

[105] K. Gupta, R.J. Wesselink, R. Liu, Z. Yuan, P.J. Kelly, *Disorder Dependence of Interface Spin Memory Loss*, Physical Review Letters **124**, 087702 (2020).

[106] J.C. Rojas-Sánchez, N. Reyren, P. Laczkowski, W. Savero, J.P. Attané, C. Deranlot, M. Jamet, J.M. George, L. Vila, H. Jaffrès, *Spin Pumping and Inverse Spin Hall Effect in Platinum: The Essential Role of Spin-Memory Loss at Metallic Interfaces*, Physical Review Letters **112**, 106602 (2014).

[107] T. White, T. Bailey, M. Pierce, C.W. Miller, *Strong Spin Pumping in Permalloy-Iridium Heterostructures*, IEEE Magnetics Letters **8**, 3508304 (2017).

[108] H. Kurt, R. Loloee, K. Eid, W.P. Pratt, J. Bass, *Spin-memory loss at 4.2 K in sputtered Pd and Pt and at Pd/Cu and Pt/Cu interfaces*, Applied Physics Letters **81**, 4787 (2002).

[109] A.J. Berger, E.R.J. Edwards, H.T. Nembach, O. Karis, M. Weiler, T.J. Silva, *Determination of the spin Hall effect and the spin diffusion length of Pt from self-consistent fitting of damping enhancement and inverse spin-orbit torque measurements*, Physical Review B **98**, 024402 (2018).

[110] Y. Tserkovnyak, A. Brataas, G.E.W. Bauer, *Enhanced Gilbert Damping in Thin Ferromagnetic Films*, Physical Review Letters **88**, 117601 (2002).

[111] A.M. Gonçalves, F. Garcia, H.K. Lee, A. Smith, P.R. Soledade, C.A.C. Passos, M. Costa, N.M. Souza-Neto, I.N. Krivorotov, L.C. Sampaio, I. Barsukov, *Oscillatory interlayer coupling in spin Hall systems*, Scientific Reports **8**, 2318 (2018).

[112] C.T. Boone, H.T. Nembach, J.M. Shaw, T.J. Silva, *Spin transport parameters in metallic multilayers determined by ferromagnetic resonance measurements of spin-pumping*, Journal of Applied Physics **113**, 153906 (2013).

[113] S. Streib, N. Vidal-Silva, K. Shen, G.E. Bauer, *Magnon-phonon interactions in magnetic insulators*, Physical Review B **99**, 1 (2019).

[114] S.R. Boona, J.P. Heremans, *Magnon thermal mean free path in yttrium iron garnet*, Physical Review B **90**, 064421 (2014).

[115] B. Heinrich, J.F. Cochran, R. Hasegawa, *FMR linebroadening in metals due to two-magnon scattering*, Journal of Applied Physics **57**, 3690 (1985).

[116] C.E. Patton, C.H. Wilts, F.B. Humphrey, *Relaxation Processes for Ferromagnetic Resonance in Thin Films*, Journal of Applied Physics **38**, 1358 (1967).

[117] V. Kamberský, *Spin-orbital Gilbert damping in common magnetic metals*, Physical Review B **76**, 134416 (2007).

[118] V. Kamberský, *FMR linewidth and disorder in metals*, Czechoslovak Journal of Physics **34**, 1111 (1984).

[119] V. Kamberský, *On ferromagnetic resonance damping in metals*, Czechoslovak Journal of Physics **26**, 1366 (1976).

[120] D. Thonig, J. Henk, *Gilbert damping tensor within the breathing Fermi surface model: anisotropy and non-locality*, New Journal of Physics **16**, 013032 (2014).

[121] A. Brataas, Y. Tserkovnyak, G.E.W. Bauer, *Scattering Theory of Gilbert Damping*, Physical Review Letters **101**, 037207 (2008).

[122] Y. Tserkovnyak, A. Brataas, G.E.W. Bauer, B.I. Halperin, *Nonlocal magnetization dynamics in ferromagnetic heterostructures*, Reviews of Modern Physics **77**, 1375 (2005).

[123] A. Brataas, Y. Tserkovnyak, G.E. Bauer, *Spin-pumping in ferromagnet–normal metal systems*, Journal of Magnetism and Magnetic Materials **272-276**, 1981 (2004).

[124] O. Mosendz, J.E. Pearson, F.Y. Fradin, G.E.W. Bauer, S.D. Bader, A. Hoffmann, *Quantifying Spin Hall Angles from Spin Pumping: Experiments and Theory*, Physical Review Letters **104**, 046601 (2010).

[125] K. Ando, Y. Kajiwara, K. Sasage, K. Uchida, E. Saitoh, *Inverse spin-hall effect induced by spin pumping in various metals*, IEEE Transactions on Magnetics **46**, 3694 (2010).

[126] A. Kapelrud, A. Brataas, *Spin Pumping and Enhanced Gilbert Damping in Thin Magnetic Insulator Films*, Physical Review Letters **111**, 097602 (2013).

[127] M.V. Costache, M. Sladkov, S.M. Watts, C.H. van der Wal, B.J. van Wees, *Electrical Detection of Spin Pumping due to the Precessing Magnetization of a Single Ferromagnet*, Physical Review Letters **97**, 216603 (2006).

[128] E. Saitoh, M. Ueda, H. Miyajima, G. Tatara, *Conversion of spin current into charge current at room temperature: Inverse spin-Hall effect*, Applied Physics Letters **88**, 182509 (2006).

[129] G. Woltersdorf, O. Mosendz, B. Heinrich, C.H. Back, *Magnetization Dynamics due to Pure Spin Currents in Magnetic Double Layers*, Physical Review Letters **99**, 246603 (2007).

[130] M. Weiler, M. Althammer, M. Schreier, J. Lotze, M. Pernpeintner, S. Meyer, H. Huebl, R. Gross, A. Kamra, J. Xiao, Y.T. Chen, H. Jiao, G.E.W. Bauer, S.T.B. Goennenwein, *Experimental Test of the Spin Mixing Interface Conductivity Concept*, Physical Review Letters **111**, 176601 (2013).

[131] M. Althammer, *Pure spin currents in magnetically ordered insulator/normal metal heterostructures*, Journal of Physics D: Applied Physics **51**, 313001 (2018).

[132] S. Klingler, V. Amin, S. Geprägs, K. Ganzhorn, H. Maier-Flaig, M. Althammer, H. Huebl, R. Gross, R.D. McMichael, M.D. Stiles, S.T. Goennenwein, M. Weiler, *Spin-Torque Excitation of Perpendicular Standing Spin Waves in Coupled YIG/Co Heterostructures*, Physical Review Letters **120**, 127201 (2018).

[133] B. Heinrich, K. Myrtle, J. Rudd, J. Cochran, R. Hasegawa, *Two-magnon scattering in iron-rich metallic glasses*, Journal of Magnetism and Magnetic Materials **31-34**, 1597 (1983).

[134] M.J. Hurben, C.E. Patton, *Theory of two magnon scattering microwave relaxation and ferromagnetic resonance linewidth in magnetic thin films*, Journal of Applied Physics **83**, 4344 (1998).

[135] R. Arias, D.L. Mills, *Extrinsic contributions to the ferromagnetic resonance response of ultrathin films*, Physical Review B **60**, 7395 (1999).

[136] K. Lenz, H. Wende, W. Kuch, K. Baberschke, K. Nagy, A. Jánossy, *Two-magnon scattering and viscous Gilbert damping in ultrathin ferromagnets*, Physical Review B **73**, 144424 (2006).

[137] K. Zakeri, J. Lindner, I. Barsukov, R. Meckenstock, M. Farle, U. von Hörsten, H. Wende, W. Keune, J. Rocker, S.S. Kalarickal, K. Lenz, W. Kuch, K. Baberschke, Z. Frait, *Spin dynamics in ferromagnets: Gilbert damping and two-magnon scattering*, Physical Review B **76**, 104416 (2007).

[138] A.J. Berger, E.R.J. Edwards, H.T. Nembach, A.D. Karenowska, M. Weiler, T.J. Silva, *Inductive detection of fieldlike and dampinglike ac inverse spin-orbit torques in ferromagnet/normal-metal bilayers*, Physical Review B **97**, 094407 (2018).

[139] S.J. Raeburn, R.V. Aldridge, *The Hall effect, resistivity and magnetic moment of amorphous and polycrystalline iron films*, Journal of Physics F: Metal Physics **8**, 1917 (1978).

[140] J.W. De Vries, *Temperature and thickness dependence of the resistivity of thin polycrystalline aluminium, cobalt, nickel, palladium, silver and gold films*, Thin Solid Films **167**, 25 (1988).

[141] B. Obry, V.I. Vasyuchka, A.V. Chumak, A.A. Serga, B. Hillebrands, *Spin-wave propagation and transformation in a thermal gradient*, Applied Physics Letters **101** (2012).

[142] A.V. Sadovnikov, C.S. Davies, V.V. Kruglyak, D.V. Romanenko, S.V. Grishin, E.N. Beginin, Y.P. Sharaevskii, S.A. Nikitov, *Spin wave propagation in a uniformly biased curved magnonic waveguide*, Physical Review B **96**, 1 (2017).

[143] A. Talalaevskij, M. Decker, J. Stigloher, A. Mitra, H.S. Körner, O. Cespedes, C.H. Back, B.J. Hickey, *Magnetic properties of spin waves in thin yttrium iron garnet films*, Physical Review B **95**, 064409 (2017).

[144] H. Qin, S.J. Hämäläinen, K. Arjas, J. Witteveen, S. van Dijken, *Propagating spin waves in nanometer-thick yttrium iron garnet films: Dependence on wave vector, magnetic field strength, and angle*, Physical Review B **98**, 224422 (2018).

[145] J.A. Osborn, *Demagnetizing Factors of the General Ellipsoid*, Physical Review **67**, 351 (1945).

[146] Z. Duan, I.N. Krivorotov, R.E. Arias, N. Reckers, S. Stienen, J. Lindner, *Spin wave eigenmodes in transversely magnetized thin film ferromagnetic wires*, Physical Review B **92**, 104424 (2015).

[147] P. Pirro, T. Brächer, K. Vogt, B. Obry, H. Schultheiss, B. Leven, B. Hillebrands, *Interference of coherent spin waves in micron-sized ferromagnetic waveguides*, Physica Status Solidi (B) Basic Research **248**, 2404 (2011).

[148] V.E. Demidov, M.P. Kostylev, K. Rott, P. Krzysteczko, G. Reiss, S.O. Demokritov, *Excitation of microwaveguide modes by a stripe antenna*, Applied Physics Letters **95**, 112509 (2009).

[149] P. Clausen, K. Vogt, H. Schultheiss, S. Schäfer, B. Obry, G. Wolf, P. Pirro, B. Leven, B. Hillebrands, *Mode conversion by symmetry breaking of propagating spin waves*, Applied Physics Letters **99**, 162505 (2011).

[150] V.E. Demidov, S. Urazhdin, R. Liu, B. Divinskiy, A. Telegin, S.O. Demokritov, *Excitation of coherent propagating spin waves by pure spin currents*, Nature Communications **7**, 10446 (2016).

[151] T. Hula, K. Schultheiss, A. Buzdakov, L. Körber, M. Bejarano, L. Flacke, L. Liensberger, M. Weiler, J.M. Shaw, H.T. Nembach, J. Fassbender, H. Schultheiss, *Nonlinear losses in magnon transport due to four-magnon scattering*, Applied Physics Letters **117**, 042404 (2020).

[152] M.M. Scott, C.E. Patton, M.P. Kostylev, B.A. Kalinikos, *Nonlinear damping of high-power magnetostatic waves in yttrium–iron–garnet films*, Journal of Applied Physics **95**, 6294 (2004).

[153] V.E. Demidov, J. Jersch, K. Rott, P. Krzysteczko, G. Reiss, S.O. Demokritov, *Nonlinear Propagation of Spin Waves in Microscopic Magnetic Stripes*, Physical Review Letters **102**, 177207 (2009).

[154] H.G. Bauer, P. Majchrak, T. Kachel, C.H. Back, G. Woltersdorf, *Nonlinear spin-wave excitations at low magnetic bias fields*, Nature Communications **6**, 8274 (2015).

[155] M. Bellini, T.W. Hänsch, *Phase-locked white-light continuum pulses: toward a universal optical frequency-comb synthesizer*, Optics Letters **25**, 1049 (2000).

[156] D.J. Jones, S.A. Diddams, M.S. Taubman, S.T. Cundiff, L.S. Ma, J.L. Hall, *Frequency comb generation using femtosecond pulses and cross-phase modulation in optical fiber at arbitrary center frequencies*, Optics Letters **25**, 308 (2000).

[157] T. Fortier, E. Baumann, *20 years of developments in optical frequency comb technology and applications*, Communications Physics **2**, 153 (2019).

[158] P. Krivosik, C.E. Patton, *Hamiltonian formulation of nonlinear spin-wave dynamics: Theory and applications*, Physical Review B **82**, 184428 (2010).

[159] F. Ciubotaru, T. Devolder, M. Manfrini, C. Adelmann, I.P. Radu, *All electrical propagating spin wave spectroscopy with broadband wavevector capability*, Applied Physics Letters **109**, 012403 (2016).

[160] A. Malozemoff, J. Slonczewski, *Magnetic Domain Walls in Bubble Materials*, Elsevier (1979).

[161] C. Moreau-Luchaire, C. Moutafis, N. Reyren, J. Sampaio, C.A.F. Vaz, N. Van Horne, K. Bouzehouane, K. Garcia, C. Deranlot, P. Warnicke, P. Wohlhüter, J.M. George, M. Weigand, J. Raabe, V. Cros, A. Fert, *Additive interfacial chiral interaction in multilayers for stabilization of small individual skyrmions at room temperature*, Nature Nanotechnology **11**, 444 (2016).

[162] A. Soumyanarayanan, M. Raju, A.L. Gonzalez Oyarce, A.K.C. Tan, M.Y. Im, A.P. Petrović, P. Ho, K.H. Khoo, M. Tran, C.K. Gan, F. Ernult, C. Panagopoulos, *Tunable room-temperature magnetic skyrmions in Ir/Fe/Co/Pt multilayers*, Nature Materials **16**, 898 (2017).

[163] B. Dieny, M. Chshiev, *Perpendicular magnetic anisotropy at transition metal/oxide interfaces and applications*, Reviews of Modern Physics **89**, 025008 (2017).

[164] S. Woo, K. Litzius, B. Krüger, M.Y. Im, L. Caretta, K. Richter, M. Mann, A. Krone, R.M. Reeve, M. Weigand, P. Agrawal, I. Lemesh, M.A. Mawass, P. Fischer, M. Kläui, G.S.D. Beach, *Observation of room-temperature magnetic skyrmions and their current-driven dynamics in ultrathin metallic ferromagnets*, Nature Materials **15**, 501 (2016).

[165] K. Zeissler, M. Mruczkiewicz, S. Finizio, J. Raabe, P.M. Shepley, A.V. Sadovnikov, S.A. Nikitov, K. Fallon, S. McFadzean, S. McVitie, T.A. Moore, G. Burnell, C.H. Marrows, *Pinning and hysteresis in the field dependent diameter evolution of skyrmions in Pt/Co/Ir superlattice stacks*, Scientific Reports **7**, 15125 (2017).

[166] C. Kooy, U. Enz, *Philips Research Reports*, Techreport (1960).

[167] F.B. Hagedorn, C.D. Graham, J.J. Rhyne, *Domain Wall Motion In Bubble Domain Materials*, 72–90 (1972).

[168] A. Smith, *Bubble-Domain Memory Devices*, Artech House Publishers, Massachusetts (1974).

[169] S. Muhlbauer, B. Binz, F. Jonietz, C. Pfleiderer, A. Rosch, A. Neubauer, R. Georgii, P. Boni, *Skyrmion Lattice in a Chiral Magnet*, Science **323**, 915 (2009).

[170] S. Heinze, K. Von Bergmann, M. Menzel, J. Brede, A. Kubetzka, R. Wiesendanger, G. Bihlmayer, S. Blügel, *Spontaneous atomic-scale magnetic skyrmion lattice in two dimensions*, Nature Physics **7**, 713 (2011).

[171] U.K. Rößler, A.N. Bogdanov, C. Pfleiderer, *Spontaneous skyrmion ground states in magnetic metals*, Nature **442**, 797 (2006).

[172] I. Dzyaloshinsky, *A thermodynamic theory of "weak" ferromagnetism of antiferromagnetics*, Journal of Physics and Chemistry of Solids **4**, 241 (1958).

[173] T. Moriya, *Anisotropic Superexchange Interaction and Weak Ferromagnetism*, Physical Review **120**, 91 (1960).

[174] A.N. Bogdanov, U.K. Rößler, *Chiral Symmetry Breaking in Magnetic Thin Films and Multilayers*, Physical Review Letters **87**, 037203 (2001).

[175] H. Yang, O. Boulle, V. Cros, A. Fert, M. Chshiev, *Controlling Dzyaloshinskii-Moriya Interaction via Chirality Dependent Atomic-Layer Stacking, Insulator Capping and Electric Field*, Scientific Reports **8**, 12356 (2018).

[176] H. Yang, A. Thiaville, S. Rohart, A. Fert, M. Chshiev, *Anatomy of Dzyaloshinskii-Moriya Interaction at Co/Pt Interfaces*, Physical Review Letters **115**, 267210 (2015).

[177] R. Cardias, A. Szilva, M.M. Bezerra-Neto, M.S. Ribeiro, A. Bergman, Y.O. Kvashnin, J. Fransson, A.B. Klautau, O. Eriksson, L. Nordström, *First-principles Dzyaloshinskii–Moriya interaction in a non-collinear framework*, Scientific Reports **10**, 20339 (2020).

[178] S. Banerjee, J. Rowland, O. Erten, M. Randeria, *Enhanced Stability of Skyrmions in Two-Dimensional Chiral Magnets with Rashba Spin-Orbit Coupling*, Physical Review X **4**, 031045 (2014).

[179] J. Rowland, S. Banerjee, M. Randeria, *Skyrmions in chiral magnets with Rashba and Dresselhaus spin-orbit coupling*, Physical Review B **93**, 020404(R) (2016).

[180] K.W. Moon, J. Yoon, C. Kim, C. Hwang, *Existence of in-Plane Magnetic Skyrmion and its Motion under Current Flow*, Physical Review Applied **12**, 064054 (2019).

[181] M. Hervé, B. Dupé, R. Lopes, M. Böttcher, M.D. Martins, T. Balashov, L. Gerhard, J. Sinova, W. Wulfhekel, *Stabilizing spin spirals and isolated skyrmions at low magnetic field exploiting vanishing magnetic anisotropy*, Nature Communications **9**, 1015 (2018).

[182] W. Legrand, D. Maccariello, F. Ajejas, S. Collin, A. Vecchiola, K. Bouzehouane, N. Reyren, V. Cros, A. Fert, *Room-temperature stabilization of antiferromagnetic skyrmions in synthetic antiferromagnets*, Nature Materials **19**, 34 (2020).

[183] I. Lemesh, F. Büttner, G.S.D. Beach, *Accurate model of the stripe domain phase of perpendicularly magnetized multilayers*, Physical Review B **95**, 174423 (2017).

[184] S.A. Montoya, S. Couture, J.J. Chess, J.C.T. Lee, N. Kent, D. Henze, S.K. Sinha, M.Y. Im, S.D. Kevan, P. Fischer, B.J. McMorran, V. Lomakin, S. Roy, E.E. Fullerton, *Tailoring magnetic energies to form dipole skyrmions and skyrmion lattices*, Physical Review B **95**, 024415 (2017).

[185] A. Bernand-Mantel, L. Camosi, A. Wartelle, N. Rougemaille, M. Darques, L. Ranno, *The skyrmion-bubble transition in a ferromagnetic thin film*, SciPost Physics **4**, 027 (2018).

[186] S.A. Montoya, S. Couture, J.J. Chess, J.C.T. Lee, N. Kent, M.Y. Im, S.D. Kevan, P. Fischer, B.J. McMorran, S. Roy, V. Lomakin, E.E. Fullerton, *Resonant properties of dipole skyrmions in amorphous Fe/Gd multilayers*, Physical Review B **95**, 224405 (2017).

[187] M. Li, D. Lau, M. De Graef, V. Sokalski, *Lorentz TEM investigation of chiral spin textures and Néel Skyrmions in asymmetric* $[Pt/(Co/Ni)_M/Ir)_N Multi-LayerThin films$, Physical Review Materials **3**, 064409 (2019).

[188] W. Koshibae, N. Nagaosa, *Dynamics of skyrmion in disordered chiral magnet of thin film form*, Scientific Reports **9**, 5111 (2019).

[189] A. Fert, N. Reyren, V. Cros, *Magnetic skyrmions: advances in physics and potential applications*, Nature Reviews Materials **2**, 17031 (2017).

[190] M. Vousden, M. Albert, M. Beg, M.A. Bisotti, R. Carey, D. Chernyshenko, D. Cortés-Ortuño, W. Wang, O. Hovorka, C.H. Marrows, H. Fangohr, *Skyrmions in thin films with easy-plane magnetocrystalline anisotropy*, Applied Physics Letters **108**, 132406 (2016).

[191] F. Büttner, I. Lemesh, G.S.D. Beach, *Theory of isolated magnetic skyrmions: From fundamentals to room temperature applications*, Scientific Reports **8**, 4464 (2018).

[192] N.K. Duong, R. Tomasello, M. Raju, A.P. Petrović, S. Chiappini, G. Finocchio, C. Panagopoulos, *Magnetization reversal signatures of hybrid and pure Néel skyrmions in thin film multilayers*, APL Materials **8**, 111112 (2020).

[193] J.A. Garlow, S.D. Pollard, M. Beleggia, T. Dutta, H. Yang, Y. Zhu, *Quantification of Mixed Bloch-Néel Topological Spin Textures Stabilized by the Dzyaloshinskii-Moriya Interaction in Co/Pd Multilayers*, Physical Review Letters **122**, 237201 (2019).

[194] W. Münzer, A. Neubauer, T. Adams, S. Mühlbauer, C. Franz, F. Jonietz, R. Georgii, P. Böni, B. Pedersen, M. Schmidt, A. Rosch, C. Pfleiderer, *Skyrmion lattice in the doped semiconductor FeCoSi*, Physical Review B **81**, 041203 (2010).

[195] S. Seki, X.Z. Yu, S. Ishiwata, Y. Tokura, *Observation of Skyrmions in a Multiferroic Material*, Science **336**, 198 (2012).

[196] G. Dresselhaus, *Spin-Orbit Coupling Effects in Zinc Blende Structures*, Physical Review **100**, 580 (1955).

[197] Y.A. Bychkov, E.I. Rashba, *Properties of a 2D electron gas with lifted spectral degeneracy* (1984).

[198] E.I. Rashba, V.I. Sheka, *Symmetry of Energy Bands in Crystals of Wurtzite Type II . Symmetry of Bands with Spin-Orbit Interaction Included Construction of double-valued irreducible representations*, Deutsche Physikalische Gesellschaft **2**, 162 (1959).

[199] N.S. Kiselev, A.N. Bogdanov, R. Schäfer, U.K. Rößler, *Chiral skyrmions in thin magnetic films: new objects for magnetic storage technologies?*, Journal of Physics D: Applied Physics **44**, 392001 (2011).

[200] W. Legrand, D. Maccariello, N. Reyren, K. Garcia, C. Moutafis, C. Moreau-Luchaire, S. Collin, K. Bouzehouane, V. Cros, A. Fert, *Room-Temperature Current-Induced Generation and Motion of sub-100 nm Skyrmions*, Nano Letters **17**, 2703 (2017).

[201] X.S. Wang, H.Y. Yuan, X.R. Wang, *A theory on skyrmion size*, Communications Physics **1**, 31 (2018).

[202] J.J. Sáenz, N. García, P. Grütter, E. Meyer, H. Heinzelmann, R. Wiesendanger, L. Rosenthaler, H.R. Hidber, H.J. Güntherodt, *Observation of magnetic forces by the atomic force microscope*, Journal of Applied Physics **62**, 4293 (1987).

[203] Y. Martin, H.K. Wickramasinghe, *Magnetic imaging by "force microscopy" with 1000 Å resolution*, Applied Physics Letters **50**, 1455 (1987).

[204] O. Kazakova, R. Puttock, C. Barton, H. Corte-León, M. Jaafar, V. Neu, A. Asenjo, *Frontiers of magnetic force microscopy*, Journal of Applied Physics **125**, 060901 (2019).

[205] U. Celano, *The Atomic Force Microscopy for Nanoelectronics*, in *NanoScience and Technology*, 408 (2019), ISBN 9783030156114.

[206] R.C. Jaklevic, J. Lambe, A.H. Silver, J.E. Mercereau, *Quantum Interference Effects in Josephson Tunneling*, Physical Review Letters **12**, 159 (1964).

[207] J. Clarke, A.I. Braginski (Eds.), *The SQUID Handbook*, Wiley (2004).

[208] N. Nagaosa, J. Sinova, S. Onoda, A.H. MacDonald, N.P. Ong, *Anomalous Hall effect*, Reviews of Modern Physics **82**, 1539 (2010).

[209] G. Bergmann, *The anomalous Hall effect*, Physics Today **32**, 25 (1979).

[210] J.R. Lindemuth, B.C. Dodrill, N.C. Oldham, L.S. Cryotronics, *Anomalous Hall Effect Magnetometry – A Method for Studying Magnetic Processes of Thin Magnetic Films*, Lakeshore cryotronics (2001).

[211] A. Neubauer, C. Pfleiderer, B. Binz, A. Rosch, R. Ritz, P.G. Niklowitz, P. Böni, *Topological Hall Effect in the A Phase of MnSi*, Physical Review Letters **102**, 186602 (2009).

[212] H. Wilhelm, M. Baenitz, M. Schmidt, U.K. Rößler, A.A. Leonov, A.N. Bogdanov, *Precursor Phenomena at the Magnetic Ordering of the Cubic Helimagnet FeGe*, Physical Review Letters **107**, 127203 (2011).

[213] I. Kézsmárki, S. Bordács, P. Milde, E. Neuber, L.M. Eng, J.S. White, H.M. Rønnow, C.D. Dewhurst, M. Mochizuki, K. Yanai, H. Nakamura, D. Ehlers, V. Tsurkan, A. Loidl, *Néel-type skyrmion lattice with confined orientation in the polar magnetic semiconductor GaV_4S_8*, Nature Materials **14**, 1116 (2015).

[214] Y. Tokunaga, X.Z. Yu, J.S. White, H.M. Rønnow, D. Morikawa, Y. Taguchi, Y. Tokura, *A new class of chiral materials hosting magnetic skyrmions beyond room temperature*, Nature Communications **6**, 7638 (2015).

[215] K. Karube, J.S. White, N. Reynolds, J.L. Gavilano, H. Oike, A. Kikkawa, F. Kagawa, Y. Tokunaga, H.M. Rønnow, Y. Tokura, Y. Taguchi, *Robust metastable skyrmions and their triangular–square lattice structural transition in a high-temperature chiral magnet*, Nature Materials **15**, 1237 (2016).

[216] A. Yagil, A. Almoalem, A. Soumyanarayanan, A.K.C. Tan, M. Raju, C. Panagopoulos, O.M. Auslaender, *Stray field signatures of Néel textured skyrmions in Ir/Fe/Co/Pt multilayer films*, Applied Physics Letters **112**, 192403 (2018).

[217] M. He, G. Li, Z. Zhu, Y. Zhang, L. Peng, R. Li, J. Li, H. Wei, T. Zhao, X.G. Zhang, S. Wang, S.Z. Lin, L. Gu, G. Yu, J.W. Cai, B.g. Shen, *Evolution of topological skyrmions across the spin reorientation transition in Pt/Co/Ta multilayers*, Physical Review B **97**, 174419 (2018).

[218] O. Boulle, J. Vogel, H. Yang, S. Pizzini, D. de Souza Chaves, A. Locatelli, T.O. Menteş, A. Sala, L.D. Buda-Prejbeanu, O. Klein, M. Belmeguenai, Y. Roussigné, A. Stashkevich, S.M. Chérif, L. Aballe, M. Foerster, M. Chshiev, S. Auffret, I.M. Miron, G. Gaudin, *Room-temperature chiral magnetic skyrmions in ultrathin magnetic nanostructures*, Nature Nanotechnology **11**, 449 (2016).

[219] M. Raju, A. Yagil, A. Soumyanarayanan, A.K.C. Tan, A. Almoalem, F. Ma, O.M. Auslaender, C. Panagopoulos, *The evolution of skyrmions in Ir/Fe/Co/Pt multilayers and their topological Hall signature*, Nature Communications **10**, 696 (2019).

[220] W. Legrand, J.Y. Chauleau, D. Maccariello, N. Reyren, S. Collin, K. Bouzehouane, N. Jaouen, V. Cros, A. Fert, *Hybrid chiral domain walls and skyrmions in magnetic multilayers*, Science Advances **4**, eaat0415 (2018).

[221] K. Chesnel, A.S. Westover, C. Richards, B. Newbold, M. Healey, L. Hindman, B. Dodson, K. Cardon, D. Montealegre, J. Metzner, T. Schneider, B. Böhm, F. Samad, L. Fallarino, O. Hellwig, *Morphological stripe-bubble transition in remanent magnetic domain patterns of Co/Pt multilayer films and its dependence on Co thickness*, Physical Review B **98**, 224404 (2018).

[222] C.J. Lin, G. Gorman, C. Lee, R. Farrow, E. Marinero, H. Do, H. Notarys, C. Chien, *Magnetic and structural properties of Co/Pt multilayers*, Journal of Magnetism and Magnetic Materials **93**, 194 (1991).

[223] M.T. Johnson, P.J.H. Bloemen, F.J.A. den Broeder, J.J. de Vries, *Magnetic anisotropy in metallic multilayers*, Reports on Progress in Physics **59**, 1409 (1996).

[224] J.M. Shaw, H.T. Nembach, T.J. Silva, *Measurement of orbital asymmetry and strain in $Co_{90}Fe_{10}$ / Ni multilayers and alloys: Origins of perpendicular anisotropy*, Physical Review B **87**, 054416 (2013).

[225] C.A.F. Vaz, J.A.C. Bland, G. Lauhoff, *Magnetism in ultrathin film structures*, Reports on Progress in Physics **71**, 056501 (2008).

[226] P. Srivastava, N. Haack, H. Wende, R. Chauvistré, K. Baberschke, *Modifications of the electronic structure of Ni/Cu(001) as a function of the film thickness*, Physical Review B **56**, R4398 (1997).

[227] S.S. Dhesi, H.A. Dürr, G. van der Laan, E. Dudzik, N.B. Brookes, *Electronic and magnetic structure of thin Ni films on Co/Cu(001)*, Physical Review B **60**, 12852 (1999).

[228] A. Siemens, Y. Zhang, J. Hagemeister, E.Y. Vedmedenko, R. Wiesendanger, *Minimal radius of magnetic skyrmions: statics and dynamics*, New Journal of Physics **18**, 045021 (2016).

[229] M.N. Wilson, A.B. Butenko, A.N. Bogdanov, T.L. Monchesky, *Chiral skyrmions in cubic helimagnet films: The role of uniaxial anisotropy*, Physical Review B **89**, 094411 (2014).

[230] J. Brandão, D.A. Dugato, R.L. Seeger, J.C. Denardin, T.J. Mori, J.C. Cezar, *Observation of magnetic skyrmions in unpatterned symmetric multilayers at room temperature and zero magnetic field*, Scientific Reports **9**, 1 (2019).

[231] K.G. Rana, A. Finco, F. Fabre, S. Chouaieb, A. Haykal, L.D. Buda-Prejbeanu, O. Fruchart, S. Le Denmat, P. David, M. Belmeguenai, T. Denneulin, R.E.

Dunin-Borkowski, G. Gaudin, V. Jacques, O. Boulle, *Room-Temperature Skyrmions at Zero Field in Exchange-Biased Ultrathin Films*, Physical Review Applied **13**, 044079 (2020).

[232] A. Samardak, A. Kolesnikov, M. Stebliy, L. Chebotkevich, A. Sadovnikov, S. Nikitov, A. Talapatra, J. Mohanty, A. Ognev, *Enhanced interfacial Dzyaloshinskii-Moriya interaction and isolated skyrmions in the inversion-symmetry-broken Ru/Co/W/Ru films*, Applied Physics Letters **112**, 192406 (2018).

[233] S.Z. Lin, A. Saxena, C.D. Batista, *Skyrmion fractionalization and merons in chiral magnets with easy-plane anisotropy*, Physical Review B **91**, 224407 (2015).

[234] S. Bordács, A. Butykai, B.G. Szigeti, J.S. White, R. Cubitt, A.O. Leonov, S. Widmann, D. Ehlers, H.A.K. von Nidda, V. Tsurkan, A. Loidl, I. Kézsmárki, *Equilibrium Skyrmion Lattice Ground State in a Polar Easy-plane Magnet*, Scientific Reports **7**, 7584 (2017).

[235] A.S. Ahmed, J. Rowland, B.D. Esser, S.R. Dunsiger, D.W. McComb, M. Randeria, R.K. Kawakami, *Chiral bobbers and skyrmions in epitaxial FeGe/Si(111) films*, Physical Review Materials **2**, 041401(R) (2018).

[236] L. Flacke, V. Ahrens, S. Mendisch, L. Körber, T. Böttcher, E. Meidinger, M. Yaqoob, M. Müller, L. Liensberger, A. Kákay, M. Becherer, P. Pirro, M. Althammer, S. Geprägs, H. Huebl, R. Gross, M. Weiler, *Robust formation of nanoscale magnetic skyrmions in easy-plane anisotropy thin film multilayers with low damping*, Physical Review B **104**, L100417 (2021).

[237] C. Denker, S. Nielsen, E. Lage, M. Römer-Stumm, H. Heyen, Y. Junk, J. Walowski, K. Waldorf, M. Münzenberg, J. McCord, *Observation of multi-skyrmion objects created by size and density control in Ta/CoFeB/MgO films* 1–21 (2020).

[238] X.Z. Yu, N. Kanazawa, Y. Onose, K. Kimoto, W.Z. Zhang, S. Ishiwata, Y. Matsui, Y. Tokura, *Near room-temperature formation of a skyrmion crystal in thin-films of the helimagnet FeGe*, Nature Materials **10**, 106 (2011).

[239] M. Farle, B. Mirwald-Schulz, A. Anisimov, W. Platow, K. Baberschke, *Higher-order magnetic anisotropies and the nature of the spin-reorientation transition in face-centered-tetragonal Ni(001)/Cu(001)*, Physical Review B - Condensed Matter and Materials Physics **55**, 3708 (1997).

[240] N.H. Kim, J. Jung, J. Cho, D.S. Han, Y. Yin, J.S. Kim, H.J. Swagten, C.Y. You, *Interfacial Dzyaloshinskii-Moriya interaction, surface anisotropy energy, and spin pumping at spin orbit coupled Ir/Co interface*, Applied Physics Letters **108** (2016).

[241] P.J. Metaxas, J.P. Jamet, A. Mougin, M. Cormier, J. Ferré, V. Baltz, B. Rodmacq, B. Dieny, R.L. Stamps, *Creep and Flow Regimes of Magnetic Domain-Wall Motion in Ultrathin Pt/Co/Pt Films with Perpendicular Anisotropy*, Physical Review Letters **99**, 217208 (2007).

[242] B. Satywali, F. Ma, S. He, M. Raju, V.P. Kravchuk, M. Garst, A. Soumyanarayanan, C. Panagopoulos, *Gyrotropic resonance of individual Néel skyrmions in Ir/Fe/Co/Pt multilayers* (2018).

[243] B. Satywali, V.P. Kravchuk, L. Pan, M. Raju, S. He, F. Ma, A.P. Petrović, M. Garst, C. Panagopoulos, *Microwave resonances of magnetic skyrmions in thin film multilayers*, Nature Communications **12**, 1909 (2021).

[244] O. Hellwig, A. Berger, J.B. Kortright, E.E. Fullerton, *Domain structure and magnetization reversal of antiferromagnetically coupled perpendicular anisotropy films*, Journal of Magnetism and Magnetic Materials **319**, 13 (2007).

[245] M. Hehn, S. Padovani, K. Ounadjela, J.P. Bucher, *Nanoscale magnetic domain structures in epitaxial cobalt films*, Physical Review B **54**, 3428 (1996).

[246] M.A. Marioni, N. Pilet, T.V. Ashworth, R.C. O'Handley, H.J. Hug, *Remanence due to Wall Magnetization and Counterintuitive Magnetometry Data in 200-nm Films of Ni*, Physical Review Letters **97**, 027201 (2006).

[247] M.W. Muller, *Domain Formation in a Ferromagnetic Plate*, Journal of Applied Physics **38**, 2413 (1967).

[248] J. Agustsson, U. Arnalds, A. Ingason, K. Gylfason, K. Johnsen, S. Olafsson, J. Gudmundsson, *Growth, coalescence, and electrical resistivity of thin Pt films grown by dc magnetron sputtering on SiO_2*, Applied Surface Science **254**, 7356 (2008).

[249] H.S. Körner, M.A.W. Schoen, T. Mayer, M.M. Decker, J. Stigloher, T. Weindler, T.N.G. Meier, M. Kronseder, C.H. Back, *Magnetic damping in poly-crystalline $Co_{25}Fe_{75}$: Ferromagnetic resonance vs. spin wave propagation experiments*, Applied Physics Letters **111**, 132406 (2017).

[250] R. Juge, K. Bairagi, K.G. Rana, J. Vogel, M. Sall, D. Mailly, V.T. Pham, Q. Zhang, N. Sisodia, M. Foerster, L. Aballe, M. Belmeguenai, Y. Roussigné, S. Auffret, L.D. Buda-Prejbeanu, G. Gaudin, D. Ravelosona, O. Boulle, *Helium Ions Put Magnetic Skyrmions on the Track*, Nano Letters **21**, 2989 (2021).

[251] J.P. Chen, D.W. Zhang, J.M. Liu, *Exotic skyrmion crystals in chiral magnets with compass anisotropy*, Scientific Reports **6**, 29126 (2016).

[252] Z. Wang, Y. Su, S.Z. Lin, C.D. Batista, *Meron, skyrmion, and vortex crystals in centrosymmetric tetragonal magnets*, Physical Review B **103**, 104408 (2021).

[253] O.I. Utesov, *Thermodynamically stable skyrmion lattice in a tetragonal frustrated antiferromagnet with dipolar interaction*, Physical Review B **103**, 064414 (2021).

[254] S. Banerjee, O. Erten, M. Randeria, *Ferromagnetic exchange, spin–orbit coupling and spiral magnetism at the $LaAlO_3/SrTiO_3$ interface*, Nature Physics **9**, 626 (2013).

[255] M.N. Potkina, I.S. Lobanov, H. Jónsson, V.M. Uzdin, *Skyrmions in antiferromagnets: Thermal stability and the effect of external field and impurities*, Journal of Applied Physics **127**, 213906 (2020).

[256] M.A. Ruderman, C. Kittel, *Indirect exchange coupling of nuclear magnetic moments by conduction electrons*, Physical Review **96**, 99 (1954).

[257] T. Kasuya, *A Theory of Metallic Ferro- and Antiferromagnetism on Zener's Model*, Progress of Theoretical Physics **16**, 45 (1956).

[258] K. Yosida, *Magnetic properties of Cu-Mn alloys*, Physical Review **106**, 893 (1957).

[259] Y. Luo, M. Moske, K. Samwer, *Interlayer coupling and magnetoresistance in Ir/Co multilayers*, Europhysics Letters (EPL) **42**, 565 (1998).

[260] S.S.P. Parkin, *Systematic variation of the strength and oscillation period of indirect magnetic exchange coupling through the 3d , 4d , and 5d transition metals*, Physical Review Letters **67**, 3598 (1991).

[261] M. Stiles, *Interlayer Exchange Coupling*, in *Ultrathin Magnetic Structures III*, Vol. 200, 99–142, Springer-Verlag, Berlin/Heidelberg (1999), ISBN 3540219536.

[262] K. Yakushiji, A. Sugihara, A. Fukushima, H. Kubota, S. Yuasa, *Very strong antiferromagnetic interlayer exchange coupling with iridium spacer layer for perpendicular magnetic tunnel junctions*, Applied Physics Letters **110**, 092406 (2017).

[263] M.S. Gabor, T. Petrisor, R.B. Mos, M. Nasui, C. Tiusan, T. Petrisor, *Interlayer exchange coupling in perpendicularly magnetized Pt/Co/Ir/Co/Pt structures*, Journal of Physics D: Applied Physics **50**, 465004 (2017).

[264] S. Karayev, P.D. Murray, D. Khadka, T.R. Thapaliya, K. Liu, S.X. Huang, *Interlayer exchange coupling in Pt/Co/Ru and Pt/Co/Ir superlattices*, Physical Review Materials **3**, 041401(R) (2019).

[265] H. Wang, L. Flacke, W. Wei, S. Liu, H. Jia, J. Chen, L. Sheng, J. Zhang, M. Zhao, C. Guo, C. Fang, X. Han, D. Yu, M. Althammer, M. Weiler, H. Yu, *Sub-50 nm wavelength spin waves excited by low-damping Co 25 Fe 75 nanowires*, Applied Physics Letters **119**, 152402 (2021).

[266] M. Küß, M. Heigl, L. Flacke, A. Hefele, A. Hörner, M. Weiler, M. Albrecht, A. Wixforth, *Symmetry of the Magnetoelastic Interaction of Rayleigh and Shear Horizontal Magnetoacoustic Waves in Nickel Thin Films on $LiTaO_3$*, Physical Review Applied **15**, 034046 (2021).

[267] M. Küß, M. Heigl, L. Flacke, A. Hörner, M. Weiler, A. Wixforth, M. Albrecht, *Nonreciprocal Magnetoacoustic Waves in Dipolar-Coupled Ferromagnetic Bilayers*, Physical Review Applied **15**, 034060 (2021).

[268] M. Müller, L. Liensberger, L. Flacke, H. Huebl, A. Kamra, W. Belzig, R. Gross, M. Weiler, M. Althammer, *Temperature-Dependent Spin Transport and Current-Induced Torques in Superconductor-Ferromagnet Heterostructures*, Physical Review Letters **126**, 087201 (2021).

[269] M. Küß, M. Heigl, L. Flacke, A. Hörner, M. Weiler, M. Albrecht, A. Wixforth, *Nonreciprocal Dzyaloshinskii–Moriya Magnetoacoustic Waves*, Physical Review Letters **125**, 217203 (2020).

[270] L. Liensberger, L. Flacke, D. Rogerson, M. Althammer, R. Gross, M. Weiler, *Spin-Wave Propagation in Metallic $Co_{25}Fe_{75}$ Films Determined by Microfocused Frequency-Resolved Magneto-Optic Kerr Effect*, IEEE Magnetics Letters **10**, 5503905 (2019).

Acknowledgements

Die Arbeit als Doktorand hat mit viel Spaß gemacht und ich habe die vergangenen Jahre am WMI genossen. Dazu haben zahlreiche Personen beigetragen ohne dessen Unterstützung und Hilfe diese Dissertation nicht zustande gekommen wäre. Ich möchte mich dafür besonders bei folgenden Personen bedanken:

Prof. Dr. Rudolf Gross als meinem Doktorvater für die Möglichkeit am Walther-Meißner-Institut zu promovieren. Danke für diese solide Platform, die Freiheiten, die Unterstützung bei meinen Manuskripten, die wertvollen Gespräche und die hilfreichen Kommentare zu der vorliegenden Doktorarbeit.

Prof. Dr. Mathias Weiler als meinem Betreuer für die immense Hilfe während meiner gesamten Zeit als Doktorand. Ich habe nicht nur immer eine offene Tür für allerelei Fragen und Anliegen gefunden sondern konnte auch immer von Mathias breitem Wissen und Erfahrung profitieren. Durch Mathias habe ich gelernt mich zu trauen Fragen zu stellen, wissenschaftlich zu präsentieren und zu diskutieren. Seine beständigen Ermutigungen für meine Arbeit haben mir geholfen mehr Selbstbewusstsein zu entwickeln und obwohl unser Austausch meist arbeitstechnischer Natur war durfte ich durch ihn somit auch charakterlich dazulernen.

Dr. Matthias Althammer als mein "zweit-Betreuer" der mir stets eine Anlaufstelle und Beratung vor allem für praktische Zwecke geboten hat. In der vielen Zeit die ich mit der Fabrikation verbracht habe hatte er für mich nicht nur wertvolle Tipps sondern hat mir auch immer wieder tatkräftig unter die Arme gegriffen.

PD Dr. Hans Huebl für die wertvollen, wissenschaftlichen Gespräche während und neben den Seminaren. Seine kritischen Fragen haben stets zu einem solideren Verständnis geführt und vor allem die Qualität meiner Manuskripte wesentlich verbessert.

Dr. Stephan Geprägs für die Unterstützung bei den Röntgen- und SQUID-Messungen. Für die Übungsorganisation hat er mir dir Arbeit als Tutor durch seine humorvolle und entspannte Art sehr angenehm gemacht und hatte immer ein offenes Ohr für Fragen.

Dr. Helmut Schultheiß, Dr. Katrin Schultheiß, Dr. Attila Kákay, Tobias Hula, Lukas Körber und *Mauricio Bejarano* für die fruchtbare Zusammenarbeit. Sie haben mir außerdem einen Besuch in Dresden ermöglicht bei denen ich sowohl an BLS Experimenten teilnehmen durfte als auch eine Einführung zu Mumaxsimulationen

erhalten habe. Danke auch an Helmut und Katrin für die anschließende private Herberge und das tolle Wochenende mit vielen eindrucksvollen Klettersteigen. Danke an Tobi und Mauricio für die gute Zusammenarbeit für die Organisation unseres PhD-Symposiums auf der DPG SKM-online Konferenz 2021.

Dr. Hans Nembach und *Dr. Justin Shaw* für die Zusammenarbeit und Diskussionen zu den Spinwellenexperimenten in CoFe.

Dr. Mathias Küß für die Möglichkeit und die Effizienz in den Kollaborationen in denen wir Magnon-Phonon Kopplungsphänomene in Mehrlagensystemen untersuchen konnten.

Prof. Dr. Haiming Yu und *Hanchen Wang* für die rege Zusammenarbeit und die Möglichkeit den Nutzen der Materialeigenschaften von CoFe auch für weitere Anwendungen in der Magnonik unter Beweis zu stellen. Danke für den immer freundlichen Austausch und durch den Beginn weiterer Projekte mit CoFe, die die Relevanz dieser Arbeit unterstreichen.

PD Dr.-Ing. Markus Becherer, Valentin Ahrens und *Simon Mendisch* für die angenehme und produktive Atmosphäre in unserer Kollaboration. Sie haben mir beigebracht wie man MFM Messungen durchführt und mit ihrer pragmatischen Art zu einem zügigen Erfolg verholfen die Skyrmionen in den CoFe-Mehrlagensystemen zu untersuchen.

Jun. Prof. Dr. Philipp Pirro und *Tobias Böttcher* für die zügige Unterstützung und Vermessung der DMI-Beiträge in den Skyrmionproben.

Anastasia Golovin als meine erste Studentin die ich für ihre Bachelorarbeit betreuen durfte. Deine freudige Art lässt mich gerne daran zurück denken das erste mal eine Studentin in der Abschlussarbeit zu begleiten.

Carolina Lüthi als meine erste Masterstudentin die ich ein ganzes Jahr betreuen durfte. Danke für deinen großen Einsatz und Eifer während des ganzen Jahres und deine Arbeit mit den YIG-FM und CSO-FM Untersuchungen. Danke für die damit verbundenen Hilfe die du mir warst und bist und dass du mir die Zusammenarbeit zu einer Freude gemacht hast.

Misbah Yaqoob als Masterstudentin die mir in der Optimierung der Skyrmionmultilagen ganz praktisch eine Hilfe war. Danke für den Eifer auch weiter in der Fabrikation vorzustoßen und erste Messungen zu kombinierten Systemen von Multilagen mit dickeren Ferromagneten voranzuschieben.

Elisabeth Meidinger als Werkstudentin und anschließend Masterstudentin die zu Transportmessungen an den Skyrmionmehrlagen vorgedrungen ist. Danke für deine Ausdauer in der Fabrikation vor allem in der Lithographie. Dein ausgeprägter Sinn für Struktur beeindruckt mich und ich werde mir davon ein paar Scheiben abschneiden. ;) Durch deine Ordnung hast du es mir stets leicht gemacht die Unmengen an Daten nachzuvollziehen und deine freundliche Art hat die Zusammenarbeit sehr angenehm gemacht.

Dr. Lukas Liensberger, Manuel Müller, Dr. Tobias Wimmer, Thomas Luschmann, Janine Gückelhorn, Dr. Daniel Schwienbacher und *Qi-Ming Chen* als meine Kollegen und

Bürogefährten. Danke für die schöne Atmosphäre und die große Hilfsbereitschaft die immer vorzufinden war. Besonders bei Lukas möchte ich mich bedanken der mir gerade am Anfang in vielen praktischen Arbeiten eine Hilfe war und mir zu einem schnellen Einblick in die Messtechniken verholfen hat. Danke auch besonders an Manuel für die engere Zusammenarbeit und den regen und produktiven Austausch über diverse Projekte.

Tom Brenninger, Sebastian Kammerer, Astrid Habel und *Andreas Russo* für die viele Hilfe vor allem in technischen, elekrischen und generell praktischen Angelegenheiten.

Dem IT-Team *Dieter Guratzsch, Matthias Opel* und *Michael Renger* für die Unterstüzung bei allerlei Schwierigkeiten mit PC und Netzwerken.

Der Werkstatt *Georg Nitschke, Christian Reichlmeier, Mario Nodes* und *Alexander Rößl* für die Beratung und Herstellung verschiedenster Bauteile und die unkomplizierte Hilfe.

Der Verwaltung *Andrea Person, Martina Meven, Carola Siegmayer* und besonders *Emel Dönertas* für die ständige, zügige und vor allem unbürokratische Hilfe in allerlei administrativen und Papier-angelegenheiten.

Dem gesamten WMI Team und dem Ensemble aus vielen neuen Kollegen und Masterstudenten vor allem die zwischenmenschliche Ebene so sehr bereichern.

Meiner Familie *Isabel, David, Eva* und *Laura* für den großen Rückhalt und die Stütze im Leben. Vielen Dank für eure anhaltende Ermutigung und Stabilität die ihr mir gegeben habt und weiterhin gebt.

Jesus Christus für die Hoffnung und den Sinn in meinem Leben.